Modelling of Flood Waves Based on Wave Propagation Algorithms with Bed Efflux and Influx Including a Coupled Pipe Network Solver

A thesis submitted to The University of Manchester for the degree of

Doctor of Philosophy

in the Faculty of Engineering and Physical Sciences (EPS)

2010

Hossein Mahdizadeh

School of Mechanical, Aerospace and Civil Engineering (MACE)

TABLE OF CONTENTS

LIST OF FIGURES

LIST OF TABLES

The University of Manchester
Faculty of Engineering and Physical Sciences

Abstract of thesis submitted by: Hossein Mahdizadeh

For the degree of: Doctor of Philosophy

and entitled: Modelling of Flood Waves Based on Wave Propagation Algorithms with Bed Efflux and Influx Including a Coupled Pipe Network Solver.

Flood propagation over urban areas can cause an interaction between the free-surface flow and large underground pipe networks used for storm drainage and sewage, causing outflows and inflows at the bed. The associated waves may collide with each other and the surface waves. In this thesis the shallow water equations are used to model this type of wave interaction over dry or wet beds with bathymetry gradients and friction terms. The proposed shallow water scheme is solved based on finite volume high-resolution Godunov-type methods. The solver is well-balanced and can accurately balance the source terms and flux-gradients for the steady-state solutions. The solver also utilises a new type of Riemann wave speed to provide depth-positive results over nearly dry beds and dry states. Additionally a new type of source term is introduced in the continuity equation to model pipe inflow and outflow conditions at bed connections.

For the standard one-dimensional shallow water equations the numerical results are validated with analytical solutions or other reference solutions provided in the literature. This includes the incipient Riemann problems for nearly dry and dry-states, steady flow over a hump in a rectangular channel and the wave propagation problem. Eventually, the generation of dry bed in the middle, over discontinuous topography is considered. Close agreement is achieved between the shallow water scheme and analytical or reference solutions for the above test cases. For the shallow water problems with influx/efflux source terms comparisons are made with STAR-CD, a commercial Navier-Stokes solver for general fluid flow prediction. The shallow water model is first used to simulate vertical flows through finite gaps in the bed. Next, the interaction of the vertical flows with a dam-break flow is considered for both dry and wet beds. An efflux number, En, is defined based on the vertical efflux velocity and the gap length. A parameter study is undertaken to investigate the effect of the one-dimensional approximation of the present model, for a range of non-dimensional efflux numbers. It is found that the shallow flow model gives sensible predictions at all times provided $En<0.5$, and for long durations for $En>0.5$. Dam break flow over an underground connecting pipe is also considered for the one-dimensional efflux problems.

To solve two-dimensional problems the shallow water scheme uses the dimensional-splitting method which solves each one-dimensional Riemann problem in the x- and y-directions separately. The cross-derivative terms for second-order accuracy are incorporated by solving another Riemann problem in the orthogonal direction. For two-dimensional problems first the dam-break problems are considered over wet and dry beds. Then, flood propagation over complex terrain is demonstrated. Next, efflux discharge is modelled in isolation over a dry bed and then with dam-break interaction, comparing with

STAR-CD results. Again very good agreement is shown between the two-dimensional shallow water model and STAR-CD for the efflux numbers of *En*<0.5.

For modelling the inundation problem over an underground pipe network the solver is coupled with the general underground pipe network solver to calculate the efflux discharge as the flood waves pass through the pipe network. For analysing the pipe network with unknown effluxes an additional set of equations is incorporated into the solution of a general pipe network solver. The shallow water solver coupled to an underground pipe network is then used to simulate dam-break interaction with pipe networks with 9 and 25 nodes to demonstrate the versatility of the method.

DECLARATION

No portion of the work referred to in the thesis has been submitted in support of an application for another degree or qualification of this or any other university or other institute of learning.

ACKNOWLEDGEMENTS

Firstly, I would like to express my thanks to my supervisor Professor Peter Stansby for his guidance and his novel research ideas. I also thank him for his support and his invaluable suggestions. Without him, I would not have had any chance to study at the University of Manchester and I owe him a debt of gratitude. I am also indebted to my co-supervisor, Dr. Ben Rogers, for his explanation and advice. I would like to sincerely thank him for his patience, encouragement and his valuable time. His experience and knowledge of shallow water equations guided me through my PhD work.

Special thanks are due to the School of Mechanical, Aerospace and Civil Engineering for the award of the MACE scholarship. I would also like to thank Professor Derek Causon and Professor Dominique Laurence for examining this thesis and their invaluable suggestions. I will forever be grateful to my family, and in particular, my father Dr. Mohammad Hadi Mahdizadeh for their encouragement and support during these years. I owe thanks to my sister Sara who patiently has drawn my initial condition figures. Eventually, my sincere gratitude goes to Dr. Mohammad Reza Jaefarzadeh for his mentorship and changing my life direction.

Chapter 1 : INTRODUCTION AND LITERATURE REVIEW

In cities, flood waves may propagate over street surfaces below which lie complicated pipe networks used for storm drainage and sewage. The flood and pipe outflows can interact at connections between the underground pipes and the street surface. To date the effects of urban flooding and inundation over cities interacting with underground sewage networks and drainage pipes have not been numerically simulated. The main purpose of this project is to employ the shallow water equations for modelling the inundation problems over underground pipe networks with either efflux/influx source terms and/or complex bed topographies. First the need of devising a robust numerical solution for the inundation problems with underground outflows is explored. Then an overview for modelling urban flooding based on the shallow water equations is provided. The rest of this Chapter is devoted to the various and existing solutions for the shallow water equations based on the Godunov methods investigated by other researchers. Finally the thesis outline and the objectives are presented.

1.1 Urban Flooding: the Need for Numerical Models including Underground Pipe Systems

Recent floods occurred in autumn 2000 across Europe and several flood events in the UK in summer 2007 caused serious damage within the urban areas mainly due to the surcharge of drainage or sewage systems and the interaction of flood waves with the efflux discharge at the street surface. The flood waves can then pass through the underground sewage manholes and may impose pressure over them which cause outflows from downstream sewage ports.

The concept of drainage system (underground pipe networks) and the free-surface flow was first considered at the eighties in the North America [18]. The early studies just considered the runoff hydrographs calculated separately for the free-surface propagation and underground systems and no numerical model has been provided to simulate the effect of surface flow propagation and sewage systems simultaneously. Additionally the effect of

interaction between over-ground flooding and efflux propagation was also neglected within the hydrological hydrograph.

These examples demonstrate the need for an accurate and robust numerical method to simulate urban flooding over an underground sewage network. The prediction method should thus be able to handle the surface shallow flow over general bathymetries coupled with the pipe network flow through connections at ground (or bed) level which cause a multiple flood waves interactions. Additionally in particular for two-dimensional problems a robust underground solver should be devised to exactly compute the sewage efflux discharge during the flood propagation. Flow local to bed influx or efflux depends on the associated velocities and pipe size and may in principle be modelled quite generally by Navier-Stokes equation solvers with free-surface capability. However for large domains in three dimensions, and even in the two dimensions of a vertical-plane, computational demands are quite prohibitive. The shallow water equations (SWEs), on the other hand, are a well-established set of conservation laws that approximate the hydrodynamics of flows in shallow water domains where the depth is small compared to the overall plan dimensions. The SWEs are depth-averaged with the assumption of hydrostatic pressure and are much more computationally efficient for simulation of inundation over large areas. The purpose of this thesis work is to develop an accurate and robust numerical scheme to model this type of wave interactions based on the SWEs for both one-dimensional and two-dimensional problems. Moreover, as mentioned above an underground pipe network solver will be introduced to evaluate the efflux discharge through the sewage manholes.

The numerical schemes provided within this thesis consist of a set of explicit solutions for the SWEs with different types of source term such as bathymetry gradients, frictions terms and more importantly the efflux/influx terms used to model the sewage pipe outflows into the streets. Furthermore, the presented methods introduce a new development and modifications to cope with difficulties in dealing with efflux/influx propagations in particular when the dry-state appears in the solution. Depending on the velocity efflux/influx propagation can be dominated by non-hydrostatic pressures and generally should be solved by the full Navier-Stokes equations. However, it will be shown that for many efflux/influx discharge problems the non-hydrostatic pressures and the viscous terms do not necessarily affect the important aspects of solution and can be neglected. This enables the SWEs to incorporate the efflux outflows terms for many applications fully

described in Chapter 3. For the problems with underground sinks or sources the comparisons for the over-ground results are made with numerical predictions from STAR-CD, a commercial Navier-Stokes solver which models the free-surface motions, and a parameter study is undertaken to investigate the effect of numerical approximation of the present model, for a range of non-dimensional efflux numbers.

1.2 An Overview for the Urban Flooding Models Based on the Shallow Water Equations

In general, urban flooding is caused by some unexpected phenomena such as dam failure, torrential rainfall or tsunami waves moving toward the urban areas. Numerical methods have been used for many years to model the inundation problems over urban areas. Computational and mathematical approaches can be employed for several reasons: First, they can be considered as a reliable approach that allows modellers or engineers to predict the flooding extent into the cities and mitigate the hazardous effects on civilians, infrastructure facilities and constructions. Second, the experimental and geophysical data obtained for the previous inundations around the world are regional and strongly depend on the geographical and local conditions for the inundated area and therefore cannot be applied for the other districts. Finally, the numerical simulation can be used for the large computational domains and can help to design the flood capacity for the conveyance channels or underground pipe networks devised for collecting free-surface flows within the cities.

Many experimental and numerical studies have been reported in the literature for the flooding problems over urban areas. See for instance the works by Shabayek *et al.* [73] and Nania *et al.* [64] and Soares-Frazão and Zech [75, 76] who modelled the dam-break problem through buildings during the inundation. More complete experimental works have been achieved by comparing numerical methods mostly with the SWEs. Stansby *et al.* [78] used the experimental investigations for the dam-break problem in the rectangular channel validated by the one-dimensional SWEs and Ritter's solution. A similar work has been performed by Soares-Frazão and Zech in [74, 76] who have compared the experimental measurements for the dam-break propagation into the rectangular channel with a 90-degree bend with two-dimensional SWEs solved based on Roe-type speed. They modelled the dam-break problem over an idealised city with both experimental and

numerical comparisons with the HLLC Riemann solver (see [76] for more details). Other works have been reported by Schubert *et al.* [72] and Gallegos *et al.* [23] who used first-order Godunov method with unstructured grids to simulate the flood extent within residential areas in Glasgow and southern California.

Recently, some attention has been paid to modelling the flood problems over the cities with sewer systems. Djordjevic´ *et al*. [18] developed a model with a one-dimensional representation of urban surface flows with underground pipe or chamber infilling, but without outflows. They have employed a solver which solves simultaneously the continuity equations for the underground network and the Saint-Venant equations for flow in the overland channels. For their own simulation a Preissmann four-point implicit scheme [2] has been applied. The numerical results within this work have been compared with the hydrological hydrographs but no physical interaction has been provided by authors.

1.3 Numerical Descretisation for the SWEs

1.3.1 Finite Difference Methods

The SWEs are generally solved based on different numerical and mathematical solutions. The difference between the solutions arises from the physical assumptions for the SWEs and the difficulties for solving different flow patterns. Several numerical methods have been used to discretise the SWEs where the finite difference methods (FDM) has been applied extensively due to the simplicity of the formulation. The FDM can be derived from Taylor-series expansion to approximate the first-order and second-order derivatives and can be used with both explicit and semi-implicit shallow water schemes.

Many semi-implicit shallow water solvers based on finite difference methods have been proposed in the literature. See for instance Stansby [77], Casulli [12], Casulli and Cheng [13]. Most of these approaches solve the pressure gradient and velocity divergence implicitly by using five-diagonal matrix with the conjugate gradient or other relaxation schemes. The updated version of the free-surface level can then be obtained explicitly by using one or more fractional time step methods. Other finite difference based methods have been specifically devised for modelling the real tsunami wave propagation. See for instance the researches have been done by Titov *et al.* [81, 82] and Liu *et al.* [53-55] who

used the FDM scheme for the Boussinesq equations. Other shallow water solver based on implicit finite difference schemes has been reviewed in [2].

The explicit FDM for the conservation laws such as Euler and SWEs was firstly introduced by Lax and Wendroff [41] and MacCormack [57]. The explicit finite difference methods sometimes provide accurate results for some shallow water problems. The problem with these schemes is that they give oscillatory results for strong shocks or rarefaction waves and special treatments are needed to avoid spurious results. This might be due to the sophisticated descretisation for the momentum or continuity equations used for some of these solutions. Several numerical treatments have been suggested for the explicit finite difference formulation to avoid spurious results. See for instance Fennema and Chaudhry (e.g. [22]) and the work done by Aguirre-Pe *et al.* [1].

1.3.2 Finite Element Methods

Another numerical approach used to discretise the partial differential equations is called the finite element method (FEM) and was firstly introduced by Clough [14] for the structural analysis. The first attempt for using the finite element for the SWEs has been made by Kawahara *et al.* [38] who has used a two step explicit Lax-Wendroff method for time descretisation along with the Galerkin approach for the spatial descretisation to model long waves. This method was significantly improved in [39, 37] and special care was taken for moving boundary conditions. Other research works have been performed by Zienkiewicz *et al.* [92, 94, 93, 91] who defined a very accurate finite element scheme, namely the Characteristic-Based-Split (CBS) approach. In the CBS scheme the velocity field for the momentum equations can be evaluated in three sequential steps. First the free-surface level is retained from momentum to compute the intermediate velocity vector. Second the obtained velocity field is used in the continuity equations which give the pressure fields and therefore the free-surface level can be computed. Eventually the velocity field is corrected based on the obtained pressure vector. Note that for the CBS scheme in each time increment several algebraic systems of equations need to be solved simultaneously. A more complete and accurate CBS scheme has been defined in [63].

The finite element schemes described above are robust and can be effectively applied for any structured or unstructured hierarchies; however they are computationally expensive

because they contain different systems of equations which requires efficient iterative or relaxation methods and for many applications explicit finite volume methods can provide very accurate results for the SWEs.

1.3.3 Finite Volume Methods

The finite volume method (FVM) was first introduced by McDonald [58]. An important property for the finite volume methods is that the conservation principles are imposed to fixed domain known as a control volume. These methods are based on the integral form of physical laws and therefore can treat difficulties that arise from discontinuous problems like hyperbolic conservation laws. For the finite volume method, the computational domain is divided into the numerical cells rather than grid points used for the finite difference methods and the vector of unknowns within the numerical cell at each time step is modified only by the flux differencing through the cell edges. Explicit finite volume methods which are shock capturing [87] are called Godunov-type methods and are well-known to produce non-oscillatory results for the discontinuous problems and are fully reviewed in this Chapter.

Solution of a Godunov-type scheme requires solving the Riemann problem which is defined as a discontinuity in space. Riemann solvers are extensively applied for solving the Euler equations as well as the inviscid SWEs and many attempts have been made to develop accurate solutions for these problems over the past two decades. However, due to the existence of discontinuities such as shock waves and the contact discontinuities within the Riemann problems, defining a robust and unique solution is a difficult task for the Riemann solvers. Moreover, many mathematical Riemann solutions implemented for solving the Euler-type equations including the SWEs are notorious for giving non-unique solutions and more importantly oscillatory results [10]. Other difficulties for the inviscid SWEs arise from the wet/dry propagation where the free-surface level approaches the bed-topography and the fluid depth becomes nearly zero or when the bore interactions occur over dry or nearly dry states. Many numerical solutions of the non-linear shallow water equations based on Riemann solvers have been developed over the years, generally based on the finite volume approach. The standard SWEs can be generally expressed as the integral form of conservation laws and therefore are preferably solved by the finite volume methods.

1.4   An Overview for the Godunov-Type Methods for the SWEs

The original Godunov method was firstly introduced in [28] for gas dynamics problems and was devised to capture discontinuities for the Riemann problems to produce non-oscillatory results. Here we will only discuss the Godunov-type finite volume methods for the inviscid SWEs (see [47, 84] for a full discussion of Godunov-type methods).

1.4.1 Exact Riemann Solvers

Over the past twenty years, many efforts have been made to develop both exact and approximate Riemann solutions for the SWEs based on the Godunov-type methods [85]. The main idea for Riemann solvers is to calculate the wave speeds for the shock waves and other discontinuities within the Riemann problem. These types of wave speeds are later used for evaluating the fluxes and eventually the updated version for the conserved variables for the next time step. Exact Riemann solvers require several steps to exactly compute the discontinuity wave speeds. First the difference between shock and rarefaction waves should be identified. Second the middle-state depth and velocity should be calculated between two waves. This can be performed by using the Rankine-Hugoniot jump condition [47, 84, 85]. If only shock waves appear in the solution then the Rankine-Hugoniot leads to non-linear equations solved by non-linear iterative schemes such as Newton method. In the case of rarefaction waves, only a simple linear system needs to be solved. The exact Riemann speed was firstly used in [62] by Marshall and Ménd̄éz for the SWEs. Bernetti *et al.* [9] have introduced a novel exact Riemann solution for solving one-dimensional SWEs with bathymetry variations. Other research works based on the exact Riemann solvers have been reported by Alcrudo and Benkhaldoun [4] and Wu and Cheung [88]. Evaluating the exact Riemann solution is computationally expensive and in practical finite volume methods approximate Riemann solvers are used rather than the exact Riemann solutions and often provide better wave speed approximations for many shallow water problems. However, some numerical challenges still exist in dealing with source terms including complex bed topography and efflux/influx source terms and special care is required to avoid non-physical results. This can be often done by utilising the combination of the exact and approximate Riemann solvers and will be fully discussed in Chapter 3.

1.4.2 Approximate Riemann Solvers

One of the most popular approximate Riemann solvers was proposed by Roe in [67] who defined a linearised Riemann solution to approximate the Jacobian matrix for the Rankine-Hugoniot condition. For the SWEs this can provide explicit formulae for calculating the water depth and depth-averaged velocities for the SWEs. The problem with the Roe speeds is that they only compute the discontinuities without rarefaction waves and can therefore lead to the violation for the entropy conditions needed to discern the difference between shock and rarefaction waves [50]. This problem can be rectified by Harten-Hyeman entropy fix condition defined in [32]. Another disadvantage for the Roe speeds is that they often give negative depths for the SWEs or negative pressure or density for the Euler equations which causes the numerical scheme to crash [47]. For the SWEs this happens when the fluid depth tends to zero or where the strong rarefaction waves occur in the solution. Another simple approximate Riemann solver was proposed by Harten *et al.* [33] called the HLL Riemann solver. The HLL Riemann solver is based on estimating the largest and smallest wave speeds that appear in the Riemann solution later used for computing the cell interface unknowns. For the earlier version of the HLL scheme only the characteristic speeds were involved in the solution which produces sharper results for the shock waves. The HLL method further developed by Enfield [20] proposed another choice of wave speed which takes the advantage of both Roe and characteristic wave speeds. This method is called HLLE and can be effectively used for many one-dimensional SWEs including wet/dry front propagation. However, for the two-dimensional SWEs the HLLE Riemann solver gives results with less resolution than the one-dimensional problems. This is due to the fact that the original HLLE method only employs two waves into the solution and the effect of contact discontinuity which appears for the two-dimensional SWEs is neglected. Toro [84] defined a more complete HLLE Riemann solver which adds a contact discontinuity computation into the approximation. This method is called the HLLC solver and can provide better results for two-dimensional SWEs.

1.4.3 High-Order Godunov-Type Schemes

The original Godunov methods were only first-order accurate. Various types of second-accurate terms have been proposed in the literature such as the Lax-Wendroff scheme defined in [41] which produces the second-order terms within the Taylor-series expansion and can be used with the finite volume methods. The problem with these terms is that they

break down near the discontinuities and are not able to give the exact solutions and often produce spurious oscillations. This is due to the elimination of the third terms in the Taylor-series expansions. This problem is partially rectified by the high-resolution methods. In fact in the high-resolution methods the second-order accurate terms are used in the smooth portion of the problem whilst the discontinuous portion of the solution remains non-oscillatory. Generally this can be accomplished by using the TVD (total variation diminishing) schemes which adds the second-order correction terms to the first-order method, along with the use of limiter functions that modifies the local smoothness of the method [47, 85].

Another class of mathematical methods which gives non-oscillatory results for the hyperbolic conservation laws are called semi-discrete methods [47]. In these methods the hyperbolic problem should be solved in two states. First the method should be discretised only in space to reach a system of ordinary differential equations (ODEs) in time. The second step then involves time descretisation for the obtained ODEs. In fact in these methods the current partial differential equations (PDEs) are reduced to ODEs and therefore any standard numerical method for solving the ODEs can be applied. This enables us to obtain the methods with order of accuracy greater than two. Many high-order semi-discrete methods have been developed in the literature, including MUSCL (monotonic upstream scheme for conservation laws), ENO (essentially non-oscillatory) and weighted ENO. More details about these methods can be found in [31, 34, 65]. The problem with these methods is that such methods rely on fluxes and might not apply for general hyperbolic systems and additionally they are computationally more expensive compared to high-resolution wave propagation algorithms defined later in this Chapter [47].

The high-resolution numerical methods described above are widely used within the Godunov finite volume methods for the SWEs. However, despite of significant efforts for solving the SWEs based on the approximate Riemann solver, some serious concerns still remain. As mentioned earlier the main difficulties are with respect to dealing the dry-state problems and steady-state cases in particular for the inhomogeneous SWEs. Any shallow water solver always needs to ensure depth non–negativity for the entire duration of the simulation. This is an important property in particular for inundation problems or for the problems which comprise of bore interactions over the dry area and require the Riemann

solvers that deal with the initial dry-state. Additionally the proposed Riemann solver should be able to preserve the mass conservation for the steady-state problems or the stationary flow when the discharge needs to be constant.

1.5 The Well–Balanced Shallow Water Solvers

The well-balanced methods can be generally achieved by mathematically or numerically balancing the flux gradients and the source terms using approximate or exact Riemann speeds described above. Rogers *et al.* [70] defined a novel Riemann solver based on the Roe wave speeds which mathematically balanced the source terms in the momentum equation. Vázquez-Cendón [86] used a type of upwind scheme to treat the source terms and also to obtain the equilibrium between the source terms and fluxes in the momentum equations. This approach has later been improved by other researchers who defined high-order TVD schemes. See the works of other researchers e.g. Hubbard and Garcia-Navarro [36] and García-Navarro and Vázquez-Cendón [25]. Delis *et al.* [17] introduced a well-balanced high-resolution scheme for modelling tsunami and long waves over both wet and dry bed profiles based on a modified Roe-type speed which enables the method to cope with wet/dry fronts propagating. Zhou *et al.* [90, 89] presented the surface gradient method (SGM) employing the HLL Riemann solver and also the MUSCL scheme to obtain high-resolution results. Other well-balanced approaches have previously been suggested by Liang *et al.* [51] who used the HLLC Riemann solver based on the Q-tree grid generation and Liang and Marche [52] defined a novel scheme that solves a set of pre-balanced governing equations with the HLL schemes. Another work was proposed by Audusse *et al.* [5] who used a well-balanced solver based on hydrostatic reconstruction. Here and in this thesis a modified version of wave propagation algorithm is used and will be reviewed briefly in the following Section. The advantages of a modified wave propagation algorithm are in relation to propagation over a dry bed. Additionally, the scheme enables the efflux/influx source terms to be incorporated simply into the continuity equation. Therefore, this represents an accurate approach with some possible advantages over the aforementioned well-balanced methods in terms of the continuity equation and is fully described in Chapter 3.

1.6 The Wave Propagation Algorithm

The wave propagation algorithm firstly defined by LeVeque [43, 45] implements the Godunov-type finite volume methods for the Riemann problems to calculate the updated version of unknowns for the next step. The only difference between the LeVeque's wave propagation algorithm and the original Godunov method [28] is that in the LeVeque's method the waves arising in the Riemann solutions are re-averaged into the neighbouring cells for the finite volume method whilst the original Godunov method uses the flux data at the cell interface for the updated version. The second-order accurate terms for the wave propagation can be added to the first-order Godunov method and only includes the correction flux terms. These additional flux terms are obtained based on the second-order accurate terms in the Lax-Wendroff schemes together with the limiter functions to avoid oscillatory results and will be fully discussed in Chapter 2. Note that for LeVeque's wave propagation algorithm the limiter terms are directly imposed into the corresponding correction terms rather than flux terms that appear in the first-order Godunov method [47] .

The first well-balanced wave propagation scheme for the inhomogeneous SWEs was presented in [46]. In this work a new discontinuity term was defined at the middle of each computational cell at the beginning of each time step. This enables the scheme to cancel the effect of source terms by the waves arising from solving the Riemann problem at this new discontinuity. Although the presented method gives excellent results for the quasi-steady conditions it is less suitable for the transcritical flow where the hydraulic jump appears in the flow and provides unsatisfactory results [46, 47, 70]. Moreover, no special care has been taken for treating the dry-state situations. LeVeque and Pelanti [48] introduced a novel formula for the wave propagation algorithm which interprets both discrepancies between vector of conserved variables and the fluxes in the adjacent cells as the waves or flux waves propagating from each cell interface. This method was later employed by Bale *et al*. [6, 47] who slightly modified the scheme to incorporate the source terms into the flux-differencing of the neighbouring cells for the wave propagation algorithm. This method is called the flux-wave approach (f-wave) [47, 50] and can predict any shallow water flow regime. More importantly the f-wave approach can cope with the difficulties explained for the wave propagation algorithms in [46] and in particular for the steady-state problems to produce well-balanced results.

For the earlier version of the f-wave approach defined in [6, 47] the wave speeds were computed using Roe's method only for the wet-state problems and therefore could not handle the dry or nearly dry-state propagations. LeVeque and George [50] defined a new type of wave speed based on the Einfeldt speed for the f-wave approach to deal with the method's inadequacies for the nearly dry-state problems. Moreover, a special wave speed was introduced for the propagation over dry states obtained using the Rankine-Hugoniot condition for only rarefaction waves. However, the proposed method cannot completely prevent depth non-negativity for achieving high-resolution results where the second-order terms should be added to the first-order scheme [27]. Additionally, for two-dimensional and for the dry-state problems the defined wave speeds cannot even be used to create the cross-derivative terms needed to obtain second-order accurate terms within the Godunov method [27].

George [26, 27] introduced a robust Riemann solver based on the wave propagation algorithm defining a fluid depth, discharge, momentum fluxes and bathymetry deviations as the four waves arising from each cell interface for the wave propagation algorithm. The presented scheme can cope with the difficulties for the flux-wave (f-wave) approach explained in [27, 50] because it utilises the properties from approximate Riemann solvers defined above. For example, in the case that the strong rarefaction waves appear in the solution these waves are divided into the discontinuity and give very approximate wave speeds [27]. Moreover, the method automatically maintains the entropy fix conditions for the rarefaction waves. In the case of shock waves the scheme uses Roe-type speeds and for treating the dry-state propagation the HLLE solver is employed to produce depth non-negativity for the wet/dry propagation. The proposed scheme can also provide very well-balanced results because the bed topography terms are treated as another discontinuity within the Riemann solution.

Herein, in this thesis a new type of wave speed will be introduced for the flux-wave approach defined above. The present method will take the advantage of both approximate and exact Riemann speeds to improve the behaviour in dry-state in particular when a single or multiple wave interactions occur over the dry-state. The efflux/influx terms are then included into the source term for the first time for the wave propagation algorithms. In fact in the present work new source terms which predict the effect of sinks or sources for the flood extent are added into flux differencing of the adjacent cell to compute the

correspondent wave speed for the Riemann solution. Additionally as mentioned earlier in this Chapter a robust pipe network solver is coupled with the free-surface solver. Hence, this demonstrates that the modified SWEs offer an accurate scheme for modelling the larger plan-scale effects of such a case without accurately representing the efflux process. The new scheme is well-balanced and can deal with the difficulties for the f-wave method. The proposed scheme uses the Harten-Hyman condition to identify the rarefaction waves from other discontinuities. For achieving the high-resolution methods the limiters defined in [47] can be used for both wet and dry conditions. This scheme has been fully described in [60] and will be explained again in Chapter 3 for the one-dimensional SWEs. The mathematical equations for the modified flux-wave method for two-dimensional SWEs are explained in Chapter 5.

1.7 Thesis Overview

Chapter 2 describes the mathematical equations and general formulations for the hyperbolic conservation laws. The Godunov-type finite volume methods based on the wave propagation algorithms are explained. Then, the flux-wave formulas and some Riemann techniques for wave propagation algorithms are introduced. Chapter 3 is devoted to the one-dimensional SWEs. A new type of wave speed which uses the combination of the approximate and exact Riemann solvers for the flux-wave approach is then defined. Chapter 4 contains the numerical results for the one-dimensional SWEs and is organised into two main parts. The first part comprises the one-dimensional problems mostly with the source terms in the momentum equations and are compared with the available analytical solutions presented in literature. Part II explains the one-dimensional problem with the efflux/influx terms and is validated with the STAR-CD solver which predicts the fluid motions. A parameter study is also undertaken for the efflux/influx results. In Chapter 5 a two-dimensional extension for the wave propagation algorithm is described. First in this Chapter, the two-dimensional wave propagation algorithm is derived from the Taylor-series expansions for the finite volume methods. Then a dimensional-splitting method which splits multidimensional conservation laws into sequential one-dimensional Riemann problem is fully introduced. Finally the two-dimensional f-wave approach is explained and the new choice of wave speeds defined in Chapter 3 is extended for two-dimensional problems. Chapter 6 provides the shallow water results for two-dimensional problems. This Chapter is also organised in two main parts. The first part includes the homogenous

SWEs or problems with the source terms only in the momentum equations and models the well-known shallow water benchmarks used by other researchers. In the second part, we compare the two-dimensional shallow water results with efflux terms with three-dimensional STAR-CD results. Chapter 7 describes the flood propagation over underground sewage pipe networks. In this Chapter first we will express the mathematical equations for the underground sewage pipe systems. Then more realistic two-dimensional benchmarks coupled with underground pipe propagations are solved with the wave propagation algorithm and therefore comprise the source terms in both continuity and momentum equations. Finally, Chapter 8 presents conclusions and more recommendation for future work.

Chapter 2 : HYPERBOLIC CONSERVATION LAWS AND THE WAVE PROPAGATION ALGORITHM

This Chapter addresses the mathematical equations for the Riemann problem and hyperbolic conservation laws. First the general formulation for the shallow water equations (SWEs) is described. Next, the discontinuous solution of the Riemann problem for the conservation laws is explained. Then, the wave propagation algorithms and finite volume Godunov-type methods are introduced for both linear and non-linear hyperbolic systems. The rest of this Chapter describes different Riemann solvers based on the wave propagation algorithms for the general conservation laws. The wave propagation algorithm and the modified flux-wave (f-wave) method for the one-dimensional SWEs are fully explained in Chapter 3.

2.1 The Shallow Water Equations

The shallow water equations (SWEs) are depth-averaged hyperbolic conservation laws for depth and momentum and can be expressed as

$$\frac{\partial h}{\partial t} + \frac{\partial}{\partial x}(hu) + \frac{\partial}{\partial y}(hv) = \phi, \tag{2.1a}$$

$$\frac{\partial(hu)}{\partial t} + \frac{\partial}{\partial x}(hu^2 + \frac{1}{2}gh^2) + \frac{\partial}{\partial y}(huv) = -gh\frac{\partial b}{\partial x} + S_{fx}, \tag{2.1b}$$

$$\frac{\partial(hv)}{\partial t} + \frac{\partial}{\partial y}(hv^2 + \frac{1}{2}gh^2) + \frac{\partial}{\partial x}(huv) = -gh\frac{\partial b}{\partial y} + S_{fy}, \tag{2.1c}$$

where g, is gravitational acceleration, h is the fluid depth and, u and v are the depth-averaged velocities in x- and y-directions, respectively and $\partial b/\partial x$ and $\partial b/\partial y$ are bathymetry gradients. S_{fx} and S_{fy} are the friction slope terms and are defined in Chapter 5 for two-dimensional SWEs and ϕ is the efflux/influx term which representing vertical flow within the continuity equation. The efflux/influx term is fully explained in Chapter 3. The SWEs above constitute a system of non-linear hyperbolic conservation laws. In general the vector U belongs to the conservation laws if the following equation is fulfilled,

$$\frac{\partial U}{\partial t} + \sum_{k=1}^{m} \frac{\partial f_k(U)}{\partial x_k} = \boldsymbol{\phi}(U, x), \tag{2.2}$$

where U is the vector of conserved variables $U = (U_1, U_2, U_3, \cdots, U_m)^T$, f is the correspondent flux terms for the *x*-direction and $\boldsymbol{\phi}$ denotes the source term vector. The system of (2.2) are conservation laws for *m* conserved variables and states that the temporal change in vector U is only caused by the flux-gradients and source terms changes within the computational domain. If we integrate the system of Equation (2.2) over a computational domain Ω, (2.2) then becomes

$$\frac{d}{dt}\int_{\Omega} U \, dx + \sum_{k=1}^{m} \int_{\Omega} f_k w_k \, dS = \int_{\Omega} \boldsymbol{\phi} \, dx, \tag{2.3}$$

where $w = (w_1, w_2, w_3, \cdots, w_m)^T$ is the outward normal vector into the boundary $\partial\Omega$. The Equation (2.3) is called the integral form of the conservation laws. If the PDEs in Equation (2.2) take the form of a hyperbolic system then the Equation (2.3) become the hyperbolic conservation laws. For the hyperbolic systems the Jacobian matrix for the flux terms should contain the real eigenvalues and linearly independent eigenvectors. The hyperbolic conservation laws can be expressed as linear, quasilinear and non-linear systems and include some specific properties briefly discussed in the next Section.

2.2 Linear and Quasilinear Conservation Laws

2.2.1 Definition of One-Dimensional Linear System

The linear system of the form

$$U_t + A U_x = 0, \tag{2.4}$$

is called a homogenous hyperbolic system if matrix A is diagonalisable (i.e. there is a complete set of eigenvectors) with real eigenvalues. Then we have

$$A r_k = \lambda_k r_k, \qquad \text{for } k = 1, 2, \cdots, m \tag{2.5}$$

34

where r_k is a corresponding eigenvector for eigenvalue λ_k. If the eigenvectors are distinct these vectors of eigenvalues are linearly independent. Hence the matrix of eigenvectors, R, is non-singular and has an inverse R^{-1} such that

$$R^{-1}AR = \Lambda \quad \text{and} \quad A = R\Lambda R^{-1}, \tag{2.6}$$

where Λ is a diagonal matrix of eigenvalues, say

$$\Lambda = \begin{bmatrix} \lambda_1 & & & \\ & \lambda_2 & & \\ & & \ddots & \\ & & & \lambda_m \end{bmatrix} \equiv diag\,(\lambda_1, \lambda_2, \ldots, \lambda_m) \tag{2.7}$$

If we replace A in Equation (2.5) by (2.6) by multiplying with R^{-1} then the linear system (2.4) can be rewritten as

$$\sigma_t + \Lambda\sigma_x = 0, \tag{2.8}$$

where $\sigma = R^{-1}U$. The above relation implies m scalar advection equations (Riemann waves) travelling at the characteristic speed, λ, and forms characteristics curves $X(t) = x_0 + \lambda_k t$ along which data propagate in the decoupled advection equations. In fact, this type of data propagation is the basis of the wave propagation algorithm extended to non-linear equations later explained in this Chapter. The characteristic lines for the Equation (2.8) are straight lines expected for the linear systems where the information should transfer through the parallel characteristics curves (lines).

2.2.2 Quasilinear Hyperbolic Systems

The one-dimensional quasilinear and non-linear hyperbolic conservation laws can generally take the form

$$U_t + F(U)_x = 0, \tag{2.9}$$

where again U is the vector of unknowns for the conserved variables and $F(U)$ implies the flux-gradient in the x-direction. Equation (2.9) shows the most common homogenous

form for the general hyperbolic systems including the SWEs. The quasilinear form for the Equation (2.9) can be written as

$$\boldsymbol{U}_t + \boldsymbol{F}'(\boldsymbol{U})\boldsymbol{U}_x = 0, \tag{2.10}$$

where $\boldsymbol{F}'(\boldsymbol{U})$ denotes the Jacobian matrix for the flux-gradient term. It should be stressed that for the linear hyperbolic systems all information travels at a local speed given by the eigenvalues of the Jacobian matrix [47] and the eigenpair $\left[\lambda_k, \boldsymbol{r}_k\right]$ implies the eigenvalue and the corresponding eigenvector for the kth characteristic family.

2.2.3 Riemann Problems

In the solution to the hyperbolic systems there might be occasions where a single jump discontinuity propagates along the characteristics curve (line). For instance consider a one–dimensional system (2.9) with piecewise constant initial conditions

$$\boldsymbol{U}(x,0) = \begin{cases} \boldsymbol{U}_l & x < 0, \\ \boldsymbol{U}_r & x > 0. \end{cases} \tag{2.11}$$

The initial value for the problem in Equation (2.11) is known as a Riemann problem.

2.2.4   Linear Riemann Waves

As mentioned in Section 2.2.1 for the linear hyperbolic systems, the Equation (2.4) can be interpreted as m scalar equations of the form (2.8) propagating at the speed of λ_k. This implies that for the initial data (2.11), the discontinuity $\boldsymbol{U}_r - \boldsymbol{U}_l$ also propagates across the related characteristic line. For the Riemann problem with $m \times m$ linear system the right and left states of the initial data (Riemann problem) can be decoupled as

$$\boldsymbol{U}_l = \sum_{k=1}^{m} \sigma_{kl} \boldsymbol{r}_k \quad \text{and} \quad \boldsymbol{U}_r = \sum_{k=1}^{m} \sigma_{kr} \boldsymbol{r}_k. \tag{2.12}$$

Then we have

$$U_r - U_l = \sum_{k=1}^{m} \alpha_k r_k, \qquad (2.13)$$

where $(\sigma_{kr} - \sigma_{kl}) r_k = \alpha_k r_k$. Note that this jump in U is an eigenvector of matrix A in Equation (2.4). This condition is called *Rankine-Hugoniot* condition [47] for the linear system that will be derived from the integral form of the conservation laws. This condition is needed for determining wave speeds for non-linear systems. In Equation (2.13) the term $\alpha_k r_k$ is the kth characteristic line and states the jump within the vector of U based on the set of Riemann waves (W_k), that is

$$U_r - U_l = \sum_{k=1}^{m} W_k. \qquad (2.14)$$

2.3 Non-linear Hyperbolic Systems

For the non-linear hyperbolic systems the Riemann problem also comprises the transitions within the solution. These types of transitions are not necessarily discontinuities and connect two states U_l and U_r defined for the Riemann problem through the characteristic family. The transition in the non-linear systems appears due to the difference between characteristic speeds from different characteristic families. Three types of transitions are introduced in the literature for the hyperbolic systems called rarefaction wave, shock waves and contact discontinuity. The rarefaction waves are a type of smooth differentiable waves and arise where the characteristic waves propagate from each other. For the rarefaction waves the solution for the Riemann problem should satisfy $U(x,t) = \tilde{U}(\xi(x,t))$ [47] throughout the wave, where

$$\tilde{U}'(\xi) = \alpha(\xi) r_k(\xi), \qquad (2.15)$$

where $\alpha(\xi)$ is a scalar value and depends on the function ξ. The curve $\tilde{U}(\xi)$ is called an *integral curve* of the vector field r_k if at each point in $\tilde{U}(\xi)$ the tangent vector to the curve, $\tilde{U}'(\xi)$, is an eigenvector of $F'(\tilde{U}(\xi))$ corresponding to the eigenvalue $\lambda_k(\tilde{U}(\xi))$ [47].

Definition 2.1 *The kth characteristic field is called genuinely non-linear if*

$$\nabla \boldsymbol{\lambda}_k (\boldsymbol{U}) \boldsymbol{r}_k (\boldsymbol{U}) \neq 0, \qquad \forall U \in \Omega \qquad (2.16)$$

Definition 2.2 *The kth characteristic is called linearly degenerate if*

$$\nabla \boldsymbol{\lambda}_k (\boldsymbol{U}) \boldsymbol{r}_k (\boldsymbol{U}) \equiv 0. \qquad \forall U \in \Omega \qquad (2.17)$$

In the linearly degenerate field the eigenvalues of the Jacobian matrix remain unchanged through any wave satisfying Equation (2.15). The discontinuities in the non-linear genuinely field are called shock waves. The property of genuinely non-linear field ensures that the characteristics never become parallel in contrary to what is expected for the linear systems. This means that characteristic lines are always compressing or expanding as U varies with time. For scalar conservation laws like advection equation U is constant along the characteristic lines which are straight lines for the smooth solution. Figure 2.1 exhibits different type of transitions for the Riemann problem in the $x - t$ plane. As can be seen in this Figure for the rarefaction waves the characteristic lines are emitting from point $x=0$ at the origin. Figure 2.1b illustrates the contact discontinuity where the characteristic lines propagate with the equal wave speed. The shock wave occurs in the Riemann problem when the characteristic lines collide with together as evident in Figure 2.1c.
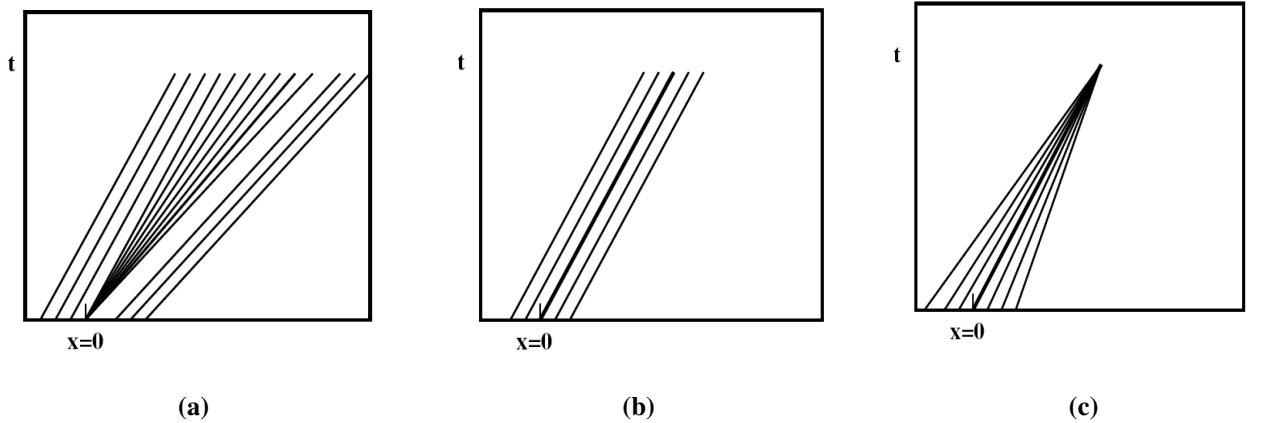
Figure 2.1. Three type of transition for the non-linear hyperbolic systems. (a): Rarefaction waves. (b): Contact discontinuity. (c): Shock waves.

2.3.1 Rankine-Hugoniot Condition

In then case that shock wave appears in the solution, it propagates with a particular speed $s(t)$. This speed can be derived by using the integral form of the conservation laws described earlier in Equation (2.3) which can be rewritten as the following condition

$$s(\boldsymbol{U}_r - \boldsymbol{U}_l) = \boldsymbol{F}(\boldsymbol{U}_r) - \boldsymbol{F}(\boldsymbol{U}_l), \tag{2.18}$$

where s is the speed of shock. The Equation (2.18) is called the Rankine-Hugoniot jump condition and plays an important role for calculating the speed of the discontinuity. For the system of m equations this condition should be applied for vectors.

The characteristic lines which satisfy (2.18) can be either a shock or contact discontinuity. Using the Rankine-Hugonit conditions for the physical rarefaction waves gives a weak solution which might not satisfy entropy condition in particular when the transonic rarefaction waves appear in the solution. In such cases the entropy fix condition should be properly employed to give physical results for the rarefaction waves and fully described in [41, 47].

2.3.2 The One-Dimensional Shallow Water Equations

For the homogenous one-dimensional SWEs the vector of unknowns and the relevant flux terms for the Equation (2.9) can be defined as

$$\boldsymbol{U} = \begin{bmatrix} h \\ hu \end{bmatrix} \quad \text{and} \quad \boldsymbol{F}(\boldsymbol{U}) = \begin{bmatrix} hu \\ hu^2 + \dfrac{1}{2}gh^2 \end{bmatrix}, \tag{2.19}$$

where h and hu are the fluid depth and discharge respectively. The Jacobian matrix for the above flux term then can be obtained by differentiating with respect to $\boldsymbol{U}$ that is

$$\boldsymbol{F}'(\boldsymbol{U}) = \begin{bmatrix} 0 & 1 \\ -u^2 + gh^2 & 2u \end{bmatrix}. \tag{2.20}$$

The eigenvalues (wave speeds) for the above Jacobian matrix can be evaluated as

$$\lambda(U)_1 = u - \sqrt{gh} \quad \text{and} \quad \lambda_2(U) = u + \sqrt{gh}, \tag{2.21}$$

and the corresponding eigenvectors can be obtained

$$r_1(U) = \begin{bmatrix} 1 \\ \lambda_1 \end{bmatrix} \quad \text{and} \quad r_2(U) = \begin{bmatrix} 1 \\ \lambda_2 \end{bmatrix}. \tag{2.22}$$

The one-dimensional SWEs are genuinely non-linear and the Riemann problem should consist of two waves, each of which can be either a rarefaction or shock wave. The contact discontinuity is not existent for the one-dimensional SWEs and only appears for the two-dimensional shallow water problems. There might be a single constant middle state between states U_l and U_r denoted by U^*. This region is often called middle state [47]. The uniqueness of the weak solution can be guaranteed by using this area employed for calculating the non-linear roots for the exact Riemann solver and will be discussed in Chapter 3 for the SWEs.

2.3.3   Riemann Invariants

The integral curve introduced in (2.15) defines a genuinely non-linear hyperbolic system and it relates to the particular function called *Riemann Invariants* since the value of this function is an invariant along an integral curve [26]. For one-dimensional SWEs the Riemann Invariants for the first and second characteristics family can be obtained as [47]

$$\delta_1(U) = u + 2\sqrt{gh}, \tag{2.23a}$$

$$\delta_2(U) = u - 2\sqrt{gh}. \tag{2.23b}$$

2.4 Finite Volume Methods for the Conservation Laws

In this Section the general formulation of the finite volume approach is described. A finite volume method is based on subdividing a computational domain into the grid cells called control volumes. Then, the approximation for each cell average can be obtained by integrating of conserved variables U over each of these volumes. For instance for the ith grid cell, $\tilde{U}$, confined in interval $C_i = (x_{i-1/2}, x_{i+1/2})$ at time t_n this can be done by

$$\tilde{U}_i^n \approx \frac{1}{\Delta x} \int_{x_{i-1/2}}^{x_{i+1/2}} U(x,t_n)dx \equiv \frac{1}{\Delta x} \int_{C_i} U(x,t_n)dx, \qquad (2.24)$$

where $\Delta x = x_{i+1/2} - x_{i-1/2}$, denotes the length of interval C_i. For one-dimensional problems the integral form of conservation laws can be integrated in time which yields the explicit flux-differencing equation

$$\tilde{U}_i^{n+1} = \tilde{U}_i^n - \frac{\Delta t}{\Delta x}(F_{i+1/2}^n - F_{1-1/2}^n), \qquad (2.25)$$

where $F_{i\pm 1/2}$ are approximations to the average fluxes along $x_{i\pm 1/2}$

$$F_{i-1/2} \approx \frac{1}{\Delta t} \int_{t_n}^{t_n+1} f(U(x_{i-1/2},t))dt. \qquad (2.26)$$

For hyperbolic conservation laws information propagates with a particular speed through the characteristic lines. Therefore, for approximating the fluxes in each cell interface $x_{i\pm 1/2}$, $F_{i-1/2}$ should be defined based on the values $\tilde{U}_{i-1}^n$ and $\tilde{U}_i^n$.

2.5 Godunov-Type Finite Volume Methods

A class of explicit schemes used extensively in the context of hyperbolic systems are called Godunov-type methods as was reviewed in Chapter 1. In these methods the Riemann problems are solved in each time step for calculating the numerical fluxes for the desired time. For solving the system of conservation laws based on Godunov-type method, first, the states at left and right of the cell interface should be chosen equal to the average cell values, that is

$$U_l = \tilde{U}_{i-1}^n \qquad \text{and} \qquad U_r = \tilde{U}_i^n. \qquad (2.27)$$

This leads to a definition of a new value at the cell interface where the Riemann problem is centred at this point. This value is implied by $\tilde{U}_{i-1/2} = U(\tilde{U}_{i-1},\tilde{U}_i)$ and can be obtained by solving the Riemann problem at this point. The next step is to define a relevant flux at the cell interface, that is, $F_{i-1/2} = F(\tilde{U}_{i-1}^n,\tilde{U}_i^n)$ and finally this flux should be used in formula

41

(2.25). The standard Godunov method is first-order accurate but appropriate second-order terms can be added to the first-order scheme based on the Taylor series expansion. However, most of these terms break down near the discontinuities and efficient slope limiters should be applied to the second-order terms to avoid oscillatory results. This is discussed later in this Chapter.

2.6 The Wave Propagation Algorithm

The wave propagation algorithm is a simple way to re-average the Riemann problem into adjacent grid cells for the finite volume methods and was introduced by LeVeque in [43, 45]. Additionally, the wave propagation algorithm can be used within the Godunov-type methods to determine fluxes based on the waves. To understand the basis of the method, a linear system of conservation laws is considered as illustrated in Figure 2.2. It is also assumed that the wave speeds take the order of $\lambda_1 < 0 < \lambda_2 < \lambda_3$. As mentioned earlier in (Equations (2.12) and (2.13)) the difference between right- and left-going states can be expressed as a set of Riemann waves (m Riemann waves), that is

$$U_i - U_{i-1} = \sum_{k=1}^{m} \alpha_{k,i-1/2} r_k = \sum_{k=1}^{m} W_{k,i-1/2}. \tag{2.28}$$

In fact the Equation (2.28) explains that in the wave propagation algorithm the discrepancies between the vectors of unknowns of the neighbouring cells can be interpreted as the sum of waves that arise from each cell interface.
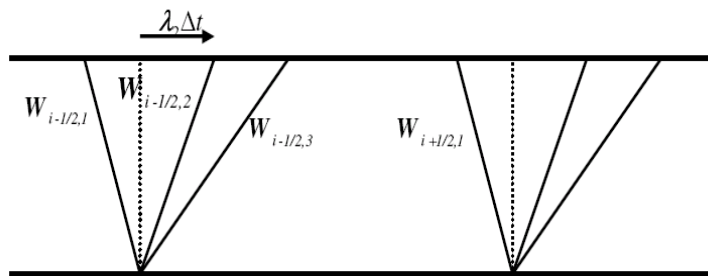
Figure 2.2. An illustration of a linear system of three equations (borrowed from [47]).

To understand the effect of each wave over the cell average, a second Riemann wave implied by $W_{2,i-1/2}$ is considered. As can be seen in (2.28) this Riemann wave includes a

42

jump in U given by $W_{2,i-1/2} = \alpha_{2,i-1/2} r_2$ and after time Δt it moves a distance $\lambda_2 \Delta t$ and occupies a fraction of the grid cell equal to $\lambda_2 \Delta t / \Delta x$. This means that the cell average of U for the next time step is varied by the amount of $\dfrac{-\lambda_2 \Delta t}{\Delta x} W_{2,i-1/2}$. In a similar way, each Riemann wave moves into the grid cell causing the same effect on the cell average. Hence, the updated version for the vector of unknowns in the next time step can be obtained via

$$\begin{aligned}
\tilde{U}_i^{n+1} &= \tilde{U}_i^n - \frac{\lambda_2 \Delta t}{\Delta x} W_{2,i-1/2} - \frac{\lambda_3 \Delta t}{\Delta x} W_{3,i-1/2} - \frac{\lambda_1 \Delta t}{\Delta x} W_{1,i+1/2} \\
&= \tilde{U}_i^n - \frac{\Delta t}{\Delta x} (\lambda_2 W_{2,i-1/2} + \lambda_3 W_{3,i-1/2} + \lambda_1 W_{1,i+1/2}).
\end{aligned} \qquad (2.29)$$

If we consider $\lambda^+ = \max(\lambda,0)$ and $\lambda^- = \min(\lambda,0)$ then, Equation (2.29) can be rewritten as

$$\tilde{U}_i^{n+1} = \tilde{U}_i^n - \frac{\Delta t}{\Delta x} \left[\sum_{k=1}^{m} (\lambda_k)^+ W_{k,i-1/2} + \sum_{k=1}^{m} (\lambda_k)^- W_{k,i+1/2} \right]. \qquad (2.30)$$

This formula is a generalisation of (2.25) that can be used for non-linear systems where discontinuities and rarefaction waves arise in the solution. Some useful notations are introduced in the following equations named left- and right-going fluctuations defined as

$$A^- \Delta U_{i+1/2} = \sum_{k=1}^{m} (\lambda_k)^- W_{k,i-1/2}, \qquad (2.31a)$$

$$A^+ \Delta U_{i-1/2} = \sum_{k=1}^{m} (\lambda_k)^+ W_{k,i-1/2}. \qquad (2.31b)$$

So the updated formula for (2.25) can be rewritten as

$$\tilde{U}_i^{n+1} = \tilde{U}_i^n - \frac{\Delta t}{\Delta x} (A^+ \Delta U_{i-1/2} + A^- \Delta U_{i+1/2}). \qquad (2.32)$$

Equation (2.32) is the Godunov version for the wave propagation algorithm. The wave propagation algorithm described above is more generally applicable than the flux-differencing (2.25) since it can be applied to non-conservative hyperbolic systems. It can be found from Equations (2.25) and (2.32) that the flux term in each cell interface can be

described based on either the right- or left-fluctuations. For example for the flux formula for the cell interface $i-1/2$ we can have [47, 50]

$$F_{i-1/2}^{n} = F(\tilde{U}_{i-1}) + A^{-}\Delta U_{i-1/2}, \tag{2.33a}$$

$$F_{i-1/2}^{n} = F(\tilde{U}_{i}) - A^{+}\Delta U_{i-1/2}. \tag{2.33b}$$

and therefore we can obtain

$$F(\tilde{U}_{i}) - F(\tilde{U}_{i-1}) = A^{+}\Delta U_{i-1/2} + A^{-}\Delta U_{i-1/2}. \tag{2.34}$$

Equation (2.34) represents a flux splitting required to maintain conservation for the wave propagation algorithm. For the hyperbolic conservation laws LeVeque and Pelanti [48] introduced the decomposition of the form

$$\begin{bmatrix} \tilde{U}_{i} - \tilde{U}_{i-1} \\ F(\tilde{U}_{i}) - F(\tilde{U}_{i-1}) \end{bmatrix} = \sum_{k=1}^{2m} \alpha_{k,i-1/2} \begin{bmatrix} r_{k,i-1/2} \\ \eta_{k,i-1/2} \end{bmatrix}, \tag{2.35}$$

where $\eta_{k,i-1/2} = s_{k,i-1/2} r_{k,i-1/2}$. The formula (2.35) states that any jump within fluxes or a vector of unknowns can be propagated as a set of waves or flux-waves from the cell interface $i-1/2$ and defines a more general class of Riemann solvers based on the wave propagation algorithm. The scalar coefficients a_{k} then can be evaluated by solving $(2m \times 2m)$ equations explained later for the SWEs in the next Chapter. Note that for the non-linear systems each wave propagates with a particular wave speed $s_{k,i-1/2}$ which presents the speed of kth wave for the $i-1/2$ interface. Therefore, the characteristic speed for the linear systems, λ_{k} can be replaced by $s_{k,i-1/2}$ for the non-linear systems. By using Equation (2.35) the fluctuations defined in (2.31) can be expressed as

$$A^{-}\Delta U_{i-1/2} = \sum_{k:s_{k,i-1/2}<0} \xi_{k,i-1/2}, \tag{2.36a}$$

$$A^{+}\Delta U_{i-1/2} = \sum_{k:s_{k,i-1/2}>0} \xi_{k,i-1/2}, \tag{2.36b}$$

44

where $\xi_{k,i-1/2} = \alpha_{k,i-1/2}\eta_{k,i-1/2}$ is called the flux–wave or f-wave. So the second component of the Equation (2.35) can be stated in a different equation, say

$$F(\tilde{U}_i) - F(\tilde{U}_{i-1}) = \sum_{k=1}^{m} \xi_{k,i-1/2},$$ (2.37)

where m again shows the number of Riemann waves. The Equation (2.37) is called the flux-wave approach because it carries the flux-waves within each cell interface rather than Riemann waves. The flux-wave approach is a robust formula for solving inhomogeneous conservation laws where the source terms appear in the solution and it produces very accurate results compared to other well-balanced Riemann solvers. The f-wave method for the SWEs is fully described in Chapter 3.

2.7 Approximate Riemann Solvers

A process of solving Riemann problems analytically is a cumbersome task and in some situations is quite expensive. However, in the context of the SWEs sometimes it is convenient to use the exact Riemann speed instead of approximate solvers. This is discussed in the next Chapter. A wide variety of approximate Riemann solvers have been introduced in literature as reviewed in Chapter 1. Approximate Riemann solvers are computationally cheaper that the exact solutions. Moreover, these solutions can be employed efficiently with second-order terms or high-resolution Godunov-type finite volume methods to obtain a better accuracy in the discontinuous points. In the approximate Riemann solvers the non-linear problem $U_t + F(U)_x = 0$ is replaced by some linearised problems defined locally at each cell interface, that is

$$\tilde{U}_t + \tilde{A}_{i-1/2}\tilde{U}_x = 0,$$ (2.38)

where the matrix $\tilde{A}_{i-1/2}$ is chosen as an approximation to the Jacobian matrix $F'(\tilde{U})_x$ in a neighbourhood of the cell average data $\tilde{U}_{i-1}$ and $\tilde{U}_i$. This means that the approximate Riemann solvers consist of m Riemann waves proportional to the eigenvectors travelling with speed $s_{k,i-1/2} = \lambda_{k,i-1/2}$ given by eigenvalues. In this Section, we describe two well known approximate Riemann solutions that extensively are used with the shallow water and Euler equations.

2.7.1 Roe Solver

Roe proposed [68] his popular method for obtaining parameter vector for the Euler equations. This method can be applied for deriving a parameter average in each cell for the SWEs. The Roe-average scheme generally is based on evaluating the Jacobian matrix $\tilde{A}_{i-1/2}$, with the special average of the left and right states of the Riemann problem. The Roe matrix is calculated by computing true flux Jacobian matrix with a valid state $\tilde{U}_{i-1/2}$ and is considered that all characteristic lines are connected through the shock wave or contact discontinuity. This means that the Rankine-Hugoniot condition defined in (2.18) is satisfied. For the SWEs and for fluid depth the Roe-average can be easily obtained by the arithmetic average for h_i and h_{i-1}.

$$\tilde{h} = \frac{1}{2}(h_{i-1} + h_i).\tag{2.39}$$

and the Roe-average for velocity can be calculated as [47]

$$\tilde{u} = \frac{\sqrt{h_{i-1}}\,u_{i-1} + \sqrt{h_i}\,u_i}{\sqrt{h_{i-1}} + \sqrt{h_i}}.\tag{2.40}$$

Then the eigenvalues of the Jacobian matrix or Roe's speed become

$$s_{1Roe} = \tilde{u}_{i-1/2} - \sqrt{g\tilde{h}_{i-1/2}} \qquad \text{and} \qquad s_{2Roe} = \tilde{u}_{i-1/2} + \sqrt{g\tilde{h}_{i-1/2}},\tag{2.41}$$

and the Roe matrix eigenvectors are

$$r_{1,i-1/2} = \begin{bmatrix} 1 \\ s_{1Roe} \end{bmatrix} \qquad \text{and} \qquad r_{2,i-1/2} = \begin{bmatrix} 1 \\ s_{2Roe} \end{bmatrix}.\tag{2.42}$$

Note that when that shock waves appear in the solution the Roe-average gives the exact Riemann solution [50]. For the rarefaction waves and in particular for transonic rarefaction, the Roe-average gives inaccurate results; however, in this case the entropy fix conditions can be used appropriately to treat this problem. The entropy fix condition for the approximate Riemann solver will be explained in Section 2.8.

2.7.2 The HLL and HLLE Solvers

In some cases, the linearised Riemann solvers such as the Roe-average fail to converge and provide negative depth for the SWEs as well as negative pressure or density for the Euler equations and shock tube problems [50]. This means that in some situations no linearisation can be achieved to maintain depth or pressure positivity and other approaches should be employed. These methods are often called positive conservative for the Euler equations [47]. The simplest positive conservative procedure is HLL introduce by Harten , Lax and van Leer [33] as mentioned in Chapter 1. According to this method $\tilde{U}_{i-1/2}$ comprises only two waves propagating at speeds $s_{1,i-1/2}$ and $s_{2,i-1/2}$. So waves in each interface can be determined by

$$W_{1,i-1/2} = \tilde{U}_{i-1/2} - \tilde{U}_{i-1} \quad \text{and} \quad W_{2,i-1/2} = \tilde{U}_i - \tilde{U}_{i-1/2} . \tag{2.43}$$

Then the flux-splitting scheme defined in Equation (2.34) can be employed to provide an explicit formula for calculating the vector of unknowns at the cell interface, say

$$s_{1,i-1/2} (\tilde{U}_{i-1/2} - \tilde{U}_{i-1}) + s_{2,i-1/2} (\tilde{U}_i - \tilde{U}_{i-1/2}) = F(\tilde{U}_i) - F(\tilde{U}_{i-1}), \tag{2.44}$$

and so we can have

$$\tilde{U}_{i-1/2} = \frac{F(\tilde{U}_i) - F(\tilde{U}_{i-1}) - s_{2,i-1/2}\tilde{U}_i + s_{1,i-1/2}\tilde{U}_{i-1}}{s_{1,i-1/2} + s_{2,i-1/2}}. \tag{2.45}$$

The HLL method was further developed by Einfeldt [20] who suggested the choice of s_1 and s_2 for gas dynamics problems as

$$s_{1,i-1/2} = \min(\lambda_{k,i-1}, \tilde{\lambda}_{k,i-1/2}), \tag{2.46a}$$

$$s_{2,i-1/2} = \max(\lambda_{k,i}, \tilde{\lambda}_{k,i-1/2}). \tag{2.46b}$$

This method is named HLLE. In the above equations $\lambda_{k,i}$ is the kth eigenvalues for the Jacobian matrix and $\tilde{\lambda}_{k,i-1/2}$ implies the kth eigenvalues for the Roe matrix. The relation

(2.46) is called an Einfeldt speed and has properties suitable for the SWEs discussed in the next Chapter. It will also be shown that the HLL can be derived directly from (2.34) instead of (2.35). A disadvantage of this solver as mentioned in Chapter 1 is that only two waves are considered in each direction. Toro [84] introduced the HLLC method and modified HLLE by defining a linear function to capture the contact discontinuity. For the one-dimensional SWEs, both HLLE and the HLLC are identical with each other. In Chapter 3 a new type of speed is defined which has several advantages for the SWEs.

2.8 Entropy Fix Conditions

Godunov-type methods converge to the correct physical solution provided that the Riemann solution is obtained based on entropy satisfying weak solutions. As described above, the Roe-average was obtained based on discontinuities that only comprise shocks with no rarefaction wave. Since approximate Riemann solvers are discontinuous, even when the true solution consists of a rarefaction wave, they can provide a weak solution which does not necessarily give a physical solution [26, 47]. The entropy fix conditions are needed for the transonic rarefaction wave in which $F'(U_l) < 0 < F'(U_r)$. In this case the true solution contains a wave spreading out in both sides and an appropriate entropy fix condition should be applied. In this Section a Harten and Hyman entropy fix conditions is defined. This approach can be used appropriately with the Godunov-type finite volume methods. Other types of entropy fix conditions have been introduced in literature. For more details see [19, 80].

2.8.1 Harten-Hyman Entropy Fix Conditions

An efficient and robust entropy fix condition for the gas dynamics problems first was introduced by Harten and Hymen [32] and modified in [10, 44]. In this method it is assumed that a transonic rarefaction appears in the kth wave of the problem, say, $\lambda_{k,l} < 0 < \lambda_{k,r}$ where $\lambda_{k,l}$ and $\lambda_{k,r}$ represents the jth eigenvalues of the Jacobian matrix for the left and right states of jth wave respectively, that is

$$U_{j,l} = \tilde{U}_{i-1} + \sum_{j=1}^{k-1} W_j \qquad \text{and} \qquad U_{k,r} = U_{k,l} + W_k . \qquad (2.47)$$

At the cell interface the single wave W_k propagating at speed of eigenvalue λ_k should be replaced by waves $W_{k,l} = \beta W_k$ and $W_{k,r} = (1-\beta)W_k$ travelling at speeds equal to left- and right-going states. To preserve conservation, the following condition needs to be satisfied, say

$$\lambda_{k,l} W_{k,l} + \lambda_{k,r} W_{k,r} = \lambda_k W_k. \tag{2.48}$$

Therefore the coefficient β can be obtained as

$$\beta = \frac{\lambda_{k,r} - \lambda_k}{\lambda_{k,r} - \lambda_{k,l}}. \tag{2.49}$$

In practical finite volume methods the values $(\lambda_k)^{\pm}$ are employed in the left- and right-going fluctuations ($A^{\pm}\Delta U_{i-1/2}$) instead of W_k within the Godunov-type method of the form (2.32). Note that the entropy fix condition can be used with any entropy violating conditions. However, for LeVeque's wave propagation algorithm the Riemann waves arising from each cell interface are averaged to the neighbouring cell. So the smooth rarefaction waves that spread from the right or left states may have no effect on the numerical solution and even in the case of smooth rarefaction wave the wave propagation algorithm can provide reasonable results provided that the structure of the rarefaction wave remains completely within a grid cell [47, 50]. As mentioned above, the exceptional case is a transonic rarefaction waves in which the wave speeds pass through zero. This type of rarefaction has a wave structure that exceeds the grid cell domain which affects the numerical solutions drastically and gives non-physical results [50]. In such cases the Harten-Hymen entropy fix conditions defined above can be used efficiently with the wave propagation algorithm to avoid undermining the solution.

2.9 CFL Conditions

The CFL condition plays an important role in numerical stability and ensures that a numerical method can converge to the true solution if its numerical domain of dependence comprise the true domain of dependence for a PDEs, as Δt and Δx tend to zero [47]. The CFL condition was introduced by Courant, Friedrichs, and Lewy in [15]. For the one-dimensional wave propagation algorithm the following CFL condition should be fulfilled

$$\frac{\max(s_{k,i-1/2})\Delta t}{\Delta x} \leq 1,$$ (2.50)

where the left hand side of Equation (2.50) is called Courant number. Note that the CFL condition is only a necessary condition for stability and it is not sufficient to guarantee stability [47].

2.10 High-Resolution Methods

The wave propagation algorithm described in (2.32) is only first-order accurate and produces diffusive results. The solution for the original Godunov method can be improved by adding second-order accurate terms created within the Lax-Wendroff methods. However, this scheme gives oscillatory results around the discontinuities and requires limiters. Here, we introduce a specific high-resolution non-linear algorithm developed by LeVeque [43, 46]. The wave propagation algorithm can be generally expressed in a second-order accurate form as

$$\tilde{\boldsymbol{U}}_i^{n+1} = \tilde{\boldsymbol{U}}_i^n - \frac{\Delta t}{\Delta x}(\boldsymbol{A}^+\Delta\boldsymbol{U}_{i-1/2} + \boldsymbol{A}^-\Delta\boldsymbol{U}_{i+1/2}) + \frac{\Delta t}{\Delta x}(\tilde{\boldsymbol{F}}_{i+1/2} - \tilde{\boldsymbol{F}}_{i-1/2}),$$ (2.51)

where the fluctuations are given by (2.31) or (2.36) and the correction fluxes then become

$$\tilde{\boldsymbol{F}}_{i-1/2} = \frac{1}{2}\left(|\boldsymbol{A}| - \frac{\Delta t}{\Delta x}\boldsymbol{A}^2\right)\Delta\boldsymbol{U}_{i-1/2} = \frac{1}{2}\left(\boldsymbol{I} - \frac{\Delta t}{\Delta x}|\boldsymbol{A}|\right)|\boldsymbol{A}|\Delta\boldsymbol{U}_{i-1/2},$$ (2.52)

where $|\boldsymbol{A}| = \boldsymbol{A}^+ - \boldsymbol{A}^-$ for the linear systems , $\boldsymbol{I}$ is an identity matrix and

$$\boldsymbol{A}^+ = \boldsymbol{R} \ \mathrm{diag}((\lambda_{k,i-1/2}^+) \ )\boldsymbol{R}^{-1},$$ (2.53)

where $\boldsymbol{R}$ is a matrix of eigenvectors. As mentioned in Chapter 1 the Lax-Wendroff method is a second-order accurate method on the smooth portions and gives dispersive results on the discontinuities which might undermine the accuracy of the problem. To cope with this problem, Equation (2.52) can be stated in a slightly different form and the limiters can be applied for the fluxes to reduce spurious solutions near discontinuities. So the correction terms in (2.52) can be defined as

$$\tilde{F}_{i-1/2} = \frac{1}{2} \sum_{k=1}^{m} \left(I - \frac{\Delta t}{\Delta x} |\lambda_k| \right) |\lambda_k| \tilde{W}_{k,i-1/2}, \tag{2.54}$$

where $\tilde{W}_{k,i-1/2} = \varphi(\theta) W_{k,i-1/2}$ is limited version of the Riemann wave and φ, is a limiting function. The limited function measures the smoothness of the solution by comparing the jump arising in the neighbouring interface that is, $W_{k,I-1/2}$ where

$$I = \begin{cases} i-1 & if \quad s_{k,i-1/2} > 0, \\ i+1 & if \quad s_{k,i-1/2} < 0. \end{cases} \tag{2.55}$$

This can be implemented by projecting the vector $W_{k,I-1/2}$ on the vector $W_{k,i-1/2}$ to obtain a vector $\theta_{i-1/2} W_{k,i-1/2}$ that is aligned with $W_{k,i-1/2}$. LeVeque [47] defined the scalar coefficient of this projection as

$$\theta_{i-1/2}^{n} = \frac{W_{k,I-1/2}.W_{k,i-1/2}}{W_{k,i-1/2}.W_{k,i-1/2}}. \tag{2.56}$$

By defining this coefficient the limited function φ can be chosen for the high-resolution methods and standard slope limiters can be applied in this way. The most general limiters that can be efficiently employed with the wave propagation algorithms are introduced as follows [47]

$$\text{Minmod: } \varphi(\theta) = \text{minmod}(1,\theta), \tag{2.57a}$$

$$\text{Superbee: } \varphi(\theta) = \max(0, \min(1,2\theta), \min(2,\theta)), \tag{2.57b}$$

$$\text{Monotonised centre (MC): } \varphi(\theta) = \max(0, \min(1,2\theta), \min(2,\theta)), \tag{2.57c}$$

$$\text{van Leer: } \varphi(\theta) = \frac{\theta + |\theta|}{1 + |\theta|}. \tag{2.57d}$$

where the Minmod function of two arguments is defined by [47]

51

$$\text{minmod}(a,b) = \begin{cases} a & if & |a| < |b| & and & ab > 0, \\ b & if & |b| < |a| & and & ab > 0, \\ 0 & if & ab \le 0. \end{cases} \qquad (2.58)$$

Note that if a and b have the same sign then the proposed scheme selects one which is smaller in magnitude otherwise it chooses zero. The MC method defined above, gives very good results near the discontinuities for the wave propagation algorithm and produces a method that changes between Fromm's method ($\varphi = 2$), Lax- Wendroff method ($\varphi = 1$) and the first order Godunov method ($\varphi = 0$). See [47] for more details and discussions. The van Leer limiter mentioned here was proposed in [42] and gives nearly identical result to MC limiter.

The wave propagation algorithm of the form (2.51) with the correction fluxes (2.54) can be extended to non-linear problems. The only change needed is again to replace the characteristic speed λ_k by the local speeds $s_{k,i-1/2}$ that is

$$\tilde{F}_{i-1/2} = \frac{1}{2} \sum_{k=1}^{m} \left(I - \frac{\Delta t}{\Delta x} |s_{k,i-1/2}| \right) |s_{k,i-1/2}| \tilde{W}_{k,i-1/2}, \qquad (2.59)$$

It should be emphasised that the high-resolution method described here with the choice of limiters of the form (2.57) are *total variation diminishing* (TVD). The total variation diminishing is the way to show that how much the slope at the discontinuities should be limited and can be defined as

$$TV(\tilde{U}) = \sum_{i=-\infty}^{+\infty} |\tilde{U}_i - \tilde{U}_{i-1}|. \qquad (2.60)$$

However, with wave propagation algorithm the limiters are imposed onto fluxes rather than slopes but it can be shown that these methods are TVD. For proof and details see [30, 80].

2.11 Balancing Flux-Gradient and Source Terms

So far in this Chapter we have presented the numerical solution for homogenous conservation laws. For many conservation laws including the inviscid SWEs the external

terms such as bed topography and friction terms are placed into the source terms which create an additional vector at the right side of conservation laws. In general, finding the exact solution for the inhomogeneous Riemann is a difficult task due to the effect of source term into the characteristic speeds. The general system for the one-dimensional inhomogeneous conservation laws can be expressed as

$$U_t + F(U)_x = S(U, x),$$ (2.61)

where $S(U, x)$ implies the source terms and represents the physical terms of external forces for the hyperbolic system. Equation (2.61) is sometimes called the "balanced laws" instead of conservation laws [26]. Here we will explain two numerical treatments for the balanced law systems namely fractional step method and flux-wave scheme described above for the homogenous systems.

2.11.1 Fractional Step Methods

The simplest class of mathematical solutions used extensively with the Riemann solvers for solving the inhomogeneous conservation laws are called fractional step methods. In this method the original hyperbolic equations is split into the homogenous conservation law and an ordinary differential equation (ODE) which only deals with the source term. So the Equation (2.61) can be rewritten as

$$U_t + F(U)_x = 0,$$ (2.62a)
$$U_t = S(U, x).$$ (2.62b)

Therefore, for solving the homogenous equation any wave propagation algorithm described above can be used directly with the Riemann solution. The source term equation then can be solved with any ODE solver such as Runge–Kutta. For many applications such as those posed in gas dynamics, this approach is quite successful and can provide very simple and accurate solution. However, for some inhomogeneous SWEs the fractional step method gives a non-physical solution. This is particularly true for the problems where the $F(U)_x$ is relatively small compared to $S(U, x)$ such that the solution is nearly close to steady-state [46, 47]. The fractional step method can fail for the steady-state case so that solving the homogenous conservation laws may lead to large changes in the solution that might not be considered by the ODE solver defined for the source terms. Additionally

some numerical errors can be created in the solutions because of different types of numerical methods are used in these two steps [47].

2.11.2 Flux-Wave (F-Wave) Method

One of the challenges for conservation laws are cases where source terms and flux-gradient terms need to neutralise the effect of each other. As mentioned above, for these cases the fractional step method produces non-physical solutions because they are not fully able to cancel the effect of $F(U)_x$ and $S(U, x)$. A class of numerical methods that can nicely balance the source terms and flux-gradient terms are called well-balanced methods and were reviewed in Chapter 1. For the wave propagation algorithm it is possible to consider the effect of source terms into the left- and right-going fluctuations $A^{\pm}\Delta U_{i-1/2}$. For the wave propagation, this method was first introduced by Bale *et al.* in [6] and places the source term into the flux differencing for the flux-wave formula of the form (2.37). Equation (2.37) can then be rewritten as

$$F(\tilde{U}_i) - F(\tilde{U}_{i-1}) - \phi_{i-1/2}\Delta x = \sum_{k=1}^{m} \xi_{k,i-1/2}, \qquad (2.63)$$

where $\phi_{i-1/2}\Delta x$ is an approximation for the source terms. The proposed method is conservative and can balance the source terms and flux-gradients for the steady-state problems. In the next Chapter a modified flux-wave method is introduced for the SWEs which are also able to consider the effect of efflux/influx terms within the wave propagation algorithm. Moreover a new choice of wave speed is defined for the wet/dry propagation.

2.12 Conclusions

In this Chapter we have presented the Riemann problems and the wave propagation algorithm for the hyperbolic conservation laws. Different types of discontinuities for the hyperbolic systems have been also introduced. Then, the first-order Godunov wave propagation algorithm based on the right- and left-going fluctuations has been defined. Moreover, approximate Riemann solvers such as Roe's and HLL or HLLE methods have been expressed for the wave propagation algorithm. In the remainder of this Chapter high-resolution form for the wave propagation algorithm were stated and the need of limiter

functions has been explained. Eventually the fractional step methods and the flux-wave formula have been stressed for solving balance law systems. In the next Chapter a one-dimensional SWEs is fully explained based on the wave propagation algorithm.

Chapter 3 : THE NUMERICAL SOLUTION FOR THE ONE-DIMENSIONAL SHALLOW WATER EQUATIONS

In this Chapter we will describe the numerical solutions for one-dimensional SWEs based on the wave propagation algorithm and the flux-wave (f-wave) formula. First source terms that represent efflux/influx in the bed due to combined sewage over flow pipe are defined in the continuity equation for the SWEs. Then the f-wave approach and HLLE Riemann solver are described. Next, the choice of exact Riemann speeds is described for the SWEs. Finally we will explain a modified Riemann solver for the SWEs and based on the f-wave approach which takes advantage of the approximate and exact Riemann speeds.

3.1 The SWEs with the Efflux/Influx and the Godunov-Type Method

The homogenous SWEs have been introduced in the previous Chapter. In general the shallow water equations (SWEs) express depth-integrated conservation of mass and momentum. The inhomogeneous form for the SWEs can take the form

$$U_t + F(U)_x = S,$$ (3.1a)

$$U = \begin{bmatrix} h \\ hu \end{bmatrix}, \qquad F(U) = \begin{bmatrix} hu \\ hu^2 + \dfrac{1}{2}gh^2 \end{bmatrix}, \qquad S = \begin{bmatrix} \phi_1 \\ \phi_2 \end{bmatrix},$$ (3.1b)

where U is the vector of unknowns, $F(U)$ denotes the flux vector, and S is the vector of source terms, ϕ_1 and ϕ_2 represent the source terms in the continuity and momentum equations, g is acceleration due to the gravity, u is the horizontal depth-averaged velocity, h and ρ are total water depth and water density respectively.

In order to include efflux and influx at the bed, the governing equations need to be rederived with their presence included in the bottom boundary condition. By integrating both the continuity and momentum equations over the depth, this adds additional source

terms to the conventional SWEs. With the presence of efflux/influx represented by a vertical velocity ω, the source terms in Equation (3.1) are given by

$$\phi_1 = \omega, \tag{3.2a}$$

$$\phi_2 = -gh\frac{\partial z_b}{\partial x} - \frac{\tau_{fx}}{\rho} - \omega u_{bed}, \tag{3.2b}$$

where z_b is bed elevation, u_{bed} denotes local (i.e. non-depth-averaged) horizontal velocity at the bed and τ_{fx} is the bed shear stress in the horizontal direction defined by $\tau_{fx} = \frac{1}{2}C_f \rho u|u|$ where C_f is the bed friction coefficient and u is the depth-averaged velocity as before. Note that the local horizontal velocity at the bed, u_{bed}, is zero both on the solid surface and at the jet exit, hence the extra momentum source term, $-\omega u_{bed}$, is zero. For the study of efflux discharge, it is important to ensure that during inundation the numerical scheme should maintain strict depth non-negativity and model accurately the effects of interacting bores.

For solving the SWEs we will use LeVeque's wave propagation algorithm [45, 46] defined in the previous Chapter. The left- or right-going fluctuations $A^{\pm}\Delta\tilde{U}_{i-1/2}$, therefore can be computed by either Equations (2.31) or (2.36). However, for solving the SWEs in this thesis the modified flux-wave method is employed. So the fluctuations should be calculated based on the flux waves rather than waves. In Equation (2.36) the flux-wave can be simply related to waves by $\boldsymbol{\xi}_{k,i-1/2} = s_{k,i-1/2}\boldsymbol{W}_{k,i-1/2}$. The waves of the conserved variables $\boldsymbol{W}_{k,i-1/2}$ then can be evaluated by multiplying an eigenvector coefficient $\alpha_{k,i-1/2}$ by the eigenvectors, such that $\boldsymbol{W}_{k,i-1/2} = \alpha_{k,i-1/2}\boldsymbol{r}_{k,i-1/2}$, where $\boldsymbol{r}_{k,i-1/2}$ is again the eigenvector. Therefore the flux-wave takes the form $\boldsymbol{\xi}_{k,i-1/2} = \beta_{k,i-1/2}\boldsymbol{r}_{k,i-1/2}$ and $\beta_{k,i-1/2} = \alpha_{k,i-1/2}s_{k,i-1/2}$. In Chapter 2 the correction flux terms have been expressed based on a limited version of waves. For the f-wave approach the correction fluxes should be evaluated based on the flux waves. So the second-order correction terms in Equation (2.59) can be rewritten for the flux waves as

$$\tilde{F}_{i-1/2} = \frac{1}{2} \sum_{k=1}^{M_w} \left(I - \frac{\Delta t}{\Delta x} \left| s_{k,i-1/2} \right| \right) \tilde{\xi}_{k,i-1/2},$$ (3.3)

where $\tilde{\xi}_{k,i-1/2}$ is the flux-limited version of the flux waves obtained by using appropriate TVD (total variation diminishing) limiters defined in the previous Chapter, M_w denotes the number of waves which is equal to two for one-dimensional SWEs and I again describes the identity matrix. Approximate Riemann solvers such as the HLLE method and the f-wave methods described in the previous Chapter are used to solve SWEs based on the wave propagation algorithm. In the next Section we will define these methods for the SWEs.

3.2   Solving for the Interface Fluxes in a Modified Wave Propagation

For the wave propagation algorithm, a new decomposition of the conserved variable, Riemann waves, $W_{k,i-1/2}$, and flux-waves, $\xi_{k,i-1/2}$ has been introduced in [48] and stated in (2.35). This formula can be defined based on the waves and flux waves as

$$\begin{bmatrix} U_i - U_{i-1} \\ F(U_i) - F(U_{i-1}) \end{bmatrix} = \sum_{k=1}^{2M_w} \begin{bmatrix} W_{k,i-1/2} \\ \xi_{k,i-1/2} \end{bmatrix},$$ (3.4)

This scheme has some useful properties since the solution uses both wave and flux differencing which can lead to a unique way to extract approximate Riemann speeds for approaches such as the HLLE and f-wave method as explained in Chapter 2. In the next Section we first describe the HLLE method which acts as an appropriate introduction to the f-wave approach for the SWEs.

3.2.1 The HLLE Method for the SWEs

The HLLE method was fully explained in Chapter 2 for the general conservation laws based on the flux splitting scheme defined in Equation (2.34). The HLLE method can be derived directly from the decomposition formula introduced in Equation (3.4) for the SWEs

$$\tilde{U}_i - \tilde{U}_{i-1} = W_{1,i-1/2} + W_{2,i-1/2},$$ (3.5a)

$$F(\tilde{U}_i) - F(\tilde{U}_{i-1}) = s_{1,i-1/2}W_{1,i-1/2} + s_{2,i-1/2}W_{1,i-1/2}. \tag{3.5b}$$

This gives a system of two equations that can be solved for the vector of waves of conserved variables W. Hence, $W_{1,i-1/2}$ and $W_{2,i-1/2}$ can be obtained via

$$W_{1,i-1/2} = \frac{s_{2,i-1/2}dU - dF}{s_{2,i-1/2} - s_{1,i-1/2}} \quad \text{and} \quad W_{2,i-1/2} = \frac{-s_{1,i-1/2}dU + dF}{s_{2,i-1/2} - s_{1,i-1/2}}, \tag{3.6}$$

where $dU = \tilde{U}_i - \tilde{U}_{i-1}$ and $dF = F(\tilde{U}_i) - F(\tilde{U}_{i-1})$. The waves obtained here can be directly used to evaluate the fluctuations for the Godunov method. As mentioned before, the wave speeds for the HLLE method are calculated by comparing the characteristic speed and the Roe speeds

$$s_{En1} = \min(u_{i-1} - \sqrt{gh_{i-1}}, s_{1Roe}) \quad \text{and} \quad s_{En2} = \max(u_i + \sqrt{gh_i}, s_{2Roe}). \tag{3.7}$$

where $s_{1,Roe}$ and s_{2Roe} are called Roe speeds which are given for the cell interface defined in Equation (2.41). The speeds defined in (3.7) are called Einfeldt speeds [50]. The HLLE method defined above is a depth-positive method and can be used appropriately for the homogenous SWEs. The weakness for the HLLE solver is that it is not a balanced approach and in particular for the steady-state shallow water equations it produces non well-balanced results and further modification is needed in order to accurately preserve a steady-state for the SWEs. For more details see [20, 21].

3.2.2 The F-Wave Approach for the SWEs

The f-wave method fully defined in Equation (2.37) allows us to solve for the wave propagation fluxes and can be obtained through Equation (3.4) and describes a jump in fluxes as the set of flux-waves propagate from the cell interface. For the f-wave approach, the flux wave $\xi_{k,i-1/2}$ is decomposed into eigenvectors as described in Section 3.1. Therefore for the one-dimensional SWEs, Equation (2.37) becomes

$$F(\tilde{U}_i) - F(\tilde{U}_{i-1}) = \beta_{1,i-1/2}r_{i-1/2} + \beta_{2,i-1/2}r_{2,i-1/2} \tag{3.8}$$

where again $r_{1,i-1/2}$ and $r_{2,i-1/2}$ are the eigenvectors of the form (2.22) for the left and right waves of the cell interface $i-1/2$. (The only difference between this and the modified HLLE solvers is that for the f-wave approach only the flux waves of the form (3.4) are considered for evaluating waves and the flux waves are decomposed into a linear combination of the eigenvectors). Instead of calculating the waves, the corresponding coefficients for the eigenvectors, $\beta_{1,i-1/2}$ and $\beta_{2,i-1.2}$, are computed for evaluating waves and flux waves themselves. The only difficulty for the method proposed in [26, 27] is that for the dry and nearly dry states, the Roe speeds give non-physical solutions for the SWEs. This problem can be partially rectified by using the choice of Einfeldt speed defined in the previous Section. However, the Einfeldt speed cannot provide the exact solution in some shallow water problems in particular where strong rarefaction waves collide with dry states. We can overcome this shortcoming by using another choice of speed for the f-wave approach. This new wave speed contains a combination of the exact and approximate Riemann speed and is fully explained in Section 3.4. In the next Section we briefly introduce the exact Riemann speeds for the SWEs which are further used with the approximate wave speeds to define an appropriate speed for the f-wave approach.

3.3 The Exact Riemann Speed for the SWEs

In the previous Chapter the Riemann invariants and the Hugoniot locus have been briefly introduced. In summary, the Riemann invariants are the exact solution to Riemann problem when only rarefaction waves appear in the solution, however the Hugoniot loci is the locus of the shock waves. For the SWEs the Riemann invariants have been defined in Equation (2.23). So if the solution to the Riemann problem just consists of two rarefaction waves the intermediate state U^{*} must lie on both of integral curves [27, 47]. For the SWEs and generally in the case that the rarefaction propagates to the different sides of the middle state, the Riemann invariants can be used appropriately to evaluate intermediate unknowns as

$$u^{*} = u_{l} + 2(\sqrt{gh_{l}} - \sqrt{gh^{*}}), \tag{3.9a}$$

$$u^{*} = u_{r} - 2(\sqrt{gh_{r}} - \sqrt{gh^{*}}), \tag{3.9b}$$

where l and r denote left and right states, respectively. This is a system of two non-linear equations that can be solved explicitly for the middle state fluid-depth as

$$h^* = \frac{1}{16g}\left[u_l - u_r + 2(\sqrt{gh_l} + \sqrt{gh_r})\right]^2.$$

(3.10)

This is valid provided that the expression being squared is non-negative. These two equations can be used to calculate the intermediate state U^* unknowns connected to U_l and U_r through the rarefaction waves. For the SWEs with two Riemann wave families the rarefaction wave occurs in the solution where we have $\lambda_1(U_l) < \lambda_1(U^*)$ and $\lambda_2(U^*) < \lambda_2(U_r)$ for left and right Riemann wave families respectively. In the case of shocks the Rankine-Hugoniot jump condition of the form Equation (2.18) should be employed to compute the speed of discontinuities. For the one-dimensional SWEs this condition becomes

$$s\left[\!\left[\begin{matrix} h \\ hu \end{matrix}\right]\!\right] = \left[\!\left[\begin{matrix} hu \\ hu^2 + \frac{1}{2}gh^2 \end{matrix}\right]\!\right],$$

(3.11)

where $[\![.]\!]$ indicates the difference across the jump discontinuity and s implies the speed of discontinuity. Figure 3.1 illustrates the Riemann problems when two shocks appear in the solution. As can be seen here two shock families are connected to each other through the middle state U^*. For the SWEs the middle state U^* can connect the right states U_l through the 1st-shock satisfy the following equation, that is

$$u^* + h^*\sqrt{\frac{g}{2}\left(\frac{1}{h^*} + \frac{1}{h_l}\right)} = u_l + h_l\sqrt{\frac{g}{2}\left(\frac{1}{h^*} + \frac{1}{h_l}\right)}.$$

(3.12)

and the right state U_r is connected to middle states through the 2nd-shock

$$u^* - h^* \sqrt{\frac{g}{2}\left(\frac{1}{h^*} + \frac{1}{h_r}\right)} = u_r - h_r \sqrt{\frac{g}{2}\left(\frac{1}{h^*} + \frac{1}{h_r}\right)}. \qquad (3.13)$$

Equations (3.12) and (3.13) should be solved simultaneously to find the middle state unknowns when only two shocks appear in the problem. This can be done by eliminating u^* from the left-hand side by using simple non-linear solvers such as Newton method. For solving this simple equation any initial guess can be used for h^* and the relaxation scheme would be reached to the desired tolerance after a few iterations.
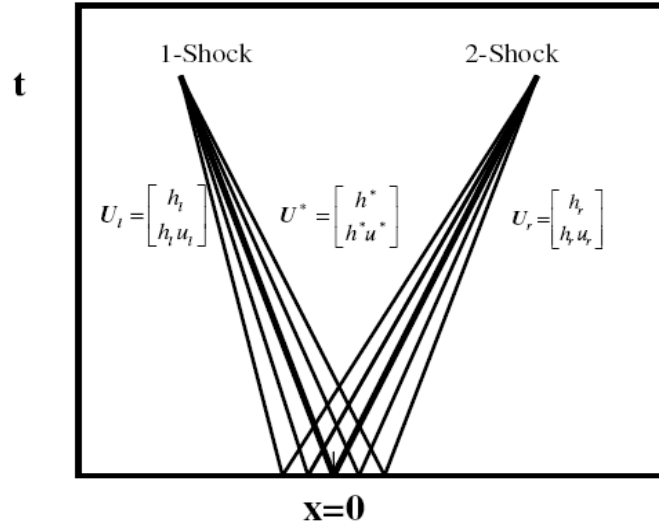
Figure 3.1 . Two shock waves structure for the Riemann problem.

In the case that the solution consists of one shock in the first Riemann wave family and rarefaction wave in the second family the combination of Equations (3.12) and (3.13) should be used with Equation (3.9). For example if the intermediate state U^* is connected to U_l by 1-rarefaction wave and connected to U_r by 2nd-shock, the following equations should be employed

$$u^* = u_l + 2(\sqrt{gh_l} - \sqrt{gh^*}), \qquad (3.14a)$$

$$u^* = u_r + (h^* - h_r)\sqrt{\frac{g}{2}\left(\frac{1}{h^*} + \frac{1}{h_r}\right)}. \qquad (3.14b)$$

Here, an appropriate entropy condition must be applied to the problem to avoid non-physical solutions. In general to find out the difference between shocks and rarefaction waves the Lax entropy condition should be used for strictly genuinely non-linear systems such as the SWEs. For the SWEs the following conditions can be employed to discern the difference between waves. For proof and more details see [26, 27]. For solving a system of Equation (3.1) the following properties need to be applied within the solution to give a correct entropy-satisfying condition:

i.   A 1-shock connects the middle state U_l to U^* if and only if $h^* > h_l$.

ii.   A 2-shock connects the middle state U_r to U^* if and only if $h^* > h_r$.

iii.   Otherwise rarefaction defined by smooth integral curve of the first or second characteristic field U^* to U_l and U_r respectively.

By introducing the above conditions the general solution for the SWEs can be evaluated for any combination of shocks and rarefaction waves. In summary therefore, for the exact solution of the Riemann problem for the SWEs, the velocity in the intermediate or star region is given by [47]

$$
u_l^* = \begin{cases} u_l + 2(\sqrt{gh_l} - \sqrt{gh^*}) & \text{if} \quad h^* < h_l, \\ u_l - (h^* - h_l)\sqrt{\dfrac{g}{2}\left(\dfrac{1}{h^*} + \dfrac{1}{h_l}\right)} & \text{if} \quad h^* > h_l, \end{cases}
\tag{3.15}
$$

for the left state, and for the right state, we have

$$
u_r^* = \begin{cases} u_r - 2(\sqrt{gh_r} - \sqrt{gh^*}) & \text{if} \quad h^* < h_r, \\ u_r + (h^* - h_r)\sqrt{\dfrac{g}{2}\left(\dfrac{1}{h^*} + \dfrac{1}{h_r}\right)} & \text{if} \quad h^* > h_r, \end{cases}
\tag{3.16}
$$

where $u_l^* = u_r^* = u^*$ and the intermediate state is computed by solving the above equations. Note that, the middle unknowns cannot be used solely to determine the Riemann wave speed when we have rarefaction waves in either the first or second Riemann wave family. For example, if we assume that the left Riemann wave is a rarefaction (Riemann wave

family 1) and the right Riemann wave is a shock (Riemann wave family 2) as was depicted in Figure 3.2 then we define the middle rarefaction speed as the average of the left-most and right-most rarefaction speeds

$$s_{Ex1} = \frac{s_{1,l}^- + s_{1,r}^+}{2},$$ (3.17)

where the characteristics speeds are evaluated from $s_{1,l}^- = u_L - \sqrt{gh_L}$ and $s_{1,r}^+ = u^* - \sqrt{gh^*}$. We define the exact shock speed, s_{Ex2}, using the Rankine-Hugoniot condition

$$s_{Ex2} = s_{2,l}^- = s_{2,r}^+ = \frac{h_r u_r - h^* u^*}{h_r - h^*} \ .$$ (3.18)

More generally, the exact Riemann speeds can be evaluated based on the following formulae

$$s_{Ex1} = \frac{s_{1,l}^- + s_{1,r}^+}{2} \qquad \text{and} \qquad s_{Ex2} = \frac{s_{2,l}^- + s_{2,r}^+}{2},$$ (3.19)

where s_{Ex1} and s_{Ex2} are the left- and right-going wave speeds propagating from the cell interface $i-1/2$.

3.4 The Choice of the Wave Speed for the F-wave Approach

As mentioned in Section 3.2, the Roe speed cannot be used for many shallow water problems in particular where there is a large difference between the velocities of the neighbouring cells in the nearly dry states. For the f-wave approach, the Roe speed gives a non-physical solution which would be a major shortcoming where the efflux discharge occurs in a dry-state. Using the Einfeldt speed with the f-wave approach can provide depth non-negativity but unfortunately cannot be applied with shallow water problems when strong transonic rarefaction waves arise in the solution, e.g. two rarefaction waves travelling away from each other. This may be due to the fact that with approximate Riemann solvers the mass of each cell becomes negative on one side of the cell interface, (see [49]). Another problem with the Einfeldt speed is that when two rarefaction waves

collide the solution produces an inaccurate result. The exact Riemann speed can be used to handle the nearly dry states and overcome the issues of the Roe speeds.
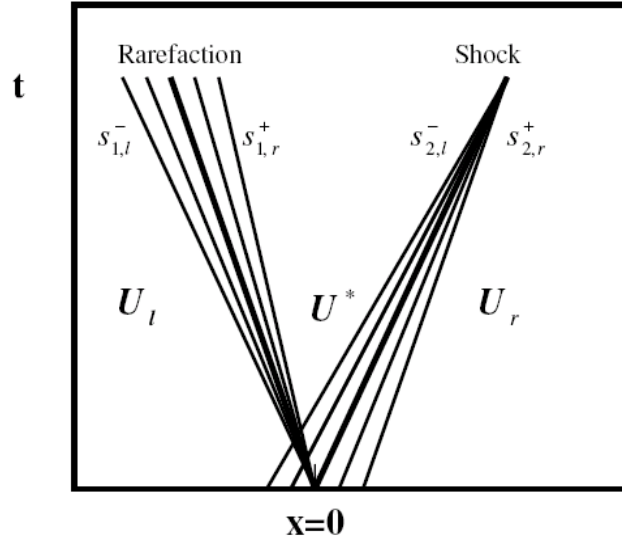
Figure 3.2. The Riemann structure for the rarefaction wave (first wave family) and shock wave(second wave)

Evaluating the exact Riemann speeds is computationally expensive compared to the approximate Riemann speeds. However, for the nearly dry-state situation, a different speed must be used to avoid depth non-negativity. This leads to the new choice of speed for the wave propagation algorithm taking the advantages of both approximate and exact Riemann speeds

$$s_1 = \min(s_{Ex1}, s_{Roe1}) \qquad \text{and} \qquad s_2 = \max(s_{Ex2}, s_{Roe2}). \tag{3.20}$$

The formulae defined in Equation (3.20) can be implemented for the initial wet state problem with the wave propagation algorithm when $h_i > 0$ and $h_{i-1} > 0$. For the initial dry-state problem the wave speed of the form (3.20) cannot be used since only rarefaction waves can physically exist over the dry states. Therefore, in the case where we have initial dry depth such as $h_i = 0$ or $h_{i-1} = 0$, using Riemann invariants [85] gives the speed for the corresponding rarefaction waves over dry states as

$$s_1 = u_i - 2\sqrt{gh_i} \quad if \quad h_{i-1} = 0 \text{ and } s_2 = u_{i-1} + 2\sqrt{gh_{i-1}} \quad if \quad h_i = 0. \tag{3.21}$$

For one-dimensional SWEs, evaluating the second and first wave speeds for the initial dry bed, $h_{i-1} = 0$, $h_i = 0$ is crucial and the speed given by Equation (3.20) cannot be used everywhere, for example when a transonic rarefaction wave appears in the solution, i.e. $s_1 < 0 < s_2$. In this case the characteristic speed can be used for the second and first wave speed for Equation (3.21). We can introduce our new wave speed for the f-wave approach which is named advanced Riemann wave speed (ARWS) and is shown below. In summary

$$
\begin{aligned}
&if \quad h_{i-1} = 0, \quad
\begin{aligned}
&s_{ARWS1} = u_i - 2\sqrt{gh_i} \\
&s_{ARWS2} =
\begin{cases}
u_i + \sqrt{gh_i} & if \quad h_i < \varepsilon \quad otherwise, \\
\max(s_{Ex2}, s_{Roe2})
\end{cases}
\end{aligned} \\[2em]
&if \quad h_i = 0, \quad
\begin{aligned}
&s_{ARWS1} =
\begin{cases}
u_{i-1} - \sqrt{gh_{i-1}} & if \quad h_{i-1} < \varepsilon \quad otherwise, \\
\min(s_{Ex1}, s_{Roe1})
\end{cases} \\
&s_{ARWS2} = u_i + 2\sqrt{gh_i}
\end{aligned} \\[2em]
&if \quad h_i > \varepsilon \quad and \quad h_{i-1} > \varepsilon \quad
\begin{aligned}
&s_{ARWS1} = \min(s_{Ex1}, s_{Roe1}) \\
&s_{ARWS2} = \max(s_{Ex2}, s_{Roe2})
\end{aligned}
\end{aligned}
$$

where s_{ARWS1} and s_{ARWS2} denote the right- and left-going Riemann wave speeds for the one-dimensional SWEs. Note, the exact Riemann speed, s_{Ex}, is only calculated at the nearly dry states defined by ε. The choice of ε depends on the particular problem. For most shallow water problems, ε can be chosen between 0.005-0.007m. This gives an accurate wet/dry front speed as demonstrated later in particular when interacting bores appear in the same dry area of the computational domain.

3.5 Treating the Source Terms with the F-Wave Approach

In earlier versions of the wave propagation algorithm [6, 47], the source terms were presented only in the momentum conservation equations and hence were incorporated into the flux differencing of the wave solution. Here, we extended this approach to handle the source terms in the continuity equation. For the inhomogeneous SWEs the source terms including efflux source terms can be defined for the cell interface $i - 1/2$ as

$$S_{i-1/2} = \begin{bmatrix} \omega_{i-1/2} \\ -\dfrac{\tau_{fx}}{\rho} - g\, h_{i-1/2}\, \dfrac{\Delta z_b}{\Delta x} \end{bmatrix},$$ (3.22)

where $h_{i-1/2} = 1/2(h_i + h_{i-1})$ and $\omega_{i-1/2}$ is the efflux/influx velocity at the cell interface. The term $-g\, h_{i-1/2}\, \dfrac{\Delta z_b}{\Delta x}$ implies bathymetry deviation as was shown in Equation (3.1a). Δz_b in Equation (3.22) can be approximated as $(z_{bi} - z_{bi-1})$ and Δx denotes cell length. For the f-wave approach the source terms can be incorporated into the flux differencing for neighbouring cells to compute the wave structures explained in Section 2.11.2 in Chapter 2. Hence, the source terms are included in the flux differencing of the adjacent cells. For calculating the flux-waves at each cell interface we need to obtain the relevant coefficients based on the efflux/influx terms and the source terms in the momentum equation. By replacing the fluxes and the source term in Equation (2.63) we can compute the flux-waves, coefficients as follows

$$\begin{bmatrix} h_i u_i - h_{i-1} u_{i-1} - \Delta x\, \omega_{i-1/2} \\ (h_i u_i^2 + 1/2\, g h_i^2) - (h_{i-1} u_{i-1}^2 + 1/2\, g h_{i-1}^2) + \Delta x\, \dfrac{\tau_{fx}}{\rho} + \dfrac{1}{2} g(h_{i+1} + h_i)(z_{bi} - z_{bi-1}) \end{bmatrix}$$
$$= \beta_{1,i-1/2} \begin{bmatrix} 1 \\ s_{1,i-1/2} \end{bmatrix} + \beta_{2,i-1/2} \begin{bmatrix} 1 \\ s_{2,i-1/2} \end{bmatrix}.$$ (3.23)

then coefficients $\beta_{1,i-1/2}$ and $\beta_{2,i-1/2}$ can be obtained as

$$\beta_{1,i-1/2} = \frac{s_{ARWS\,2,i-1/2}\Gamma_1 - \Gamma_2}{s_{ARWS\,2,i-1/2} - s_{ARWS\,1,i-1/2}} \quad \text{and} \quad \beta_{2,i-1/2} = \frac{-s_{ARWS\,1,i-1/2}\Gamma_1 + \Gamma_2}{s_{ARWS\,2,i-1/2} - s_{ARWS\,1,i-1/2}}.$$ (3.24)

where

$$\Gamma_1 = h_i u_i - h_{i-1} u_{i-1} - \Delta x\, \omega_{i-1/2},$$ (3.25a)

$$\Gamma_2 = (h_i u_i^2 + 1/2\, g h_i^2) - (h_{i-1} u_{i-1}^2 + 1/2\, g h_{i-1}^2) + \Delta x\, \frac{\tau_{fx}}{\rho} + \frac{1}{2} g\, (h_{i+1} + h_i)(z_{bi} - z_{bi-1}).$$ (3.26b)

The quantity $\Delta x\; \omega_{i\text{-}1/2}$ is called the efflux or influx discharge, depending on the sign of $\omega_{i-1/2}$. After obtaining the coefficients $\beta_{1,i-1/2}$ and $\beta_{2,i-1/2}$ the right- and left-going fluctuations can be computed.

It should be noted that the SWEs are obtained based on the assumption of hydrostatic pressure and negligible vertical acceleration. The viability of this approximation for efflux flows will depend on the local efflux number and will be investigated numerically in Chapter 4 through comparison with a full Navier-Stokes equation solver (with dynamic pressure computation).

In summary therefore, the numerical scheme introduced in this Chapter is based on the modified form of the wave propagation algorithm where the fluxes which incorporate the efflux/influx source terms are solved using the f-wave (or flux differencing) approach, and new choices of wave speed have been proposed to deal with the propagation of the wet-dry interface. This makes the numerical scheme significantly different from previous works in this area [6, 46] for a wide range of applications.

Other well-balanced approaches have previously been suggested e.g. Audusse *et al*. [5] Liang and Marche [52] and the works done by other researchers were reviewed in Chapter 1. The advantages of the present scheme have already been discussed, particularly in relation to propagation over a dry bed and the scheme enables the efflux/influx source terms to be incorporated simply. Therefore, this represents an accurate approach with some possible advantages over [5] and [52] in terms of the continuity equation.

3.6 Boundary Conditions

An advantage of the wave propagation algorithm is that boundary conditions can be specified simply for many problems. The wave propagation algorithm with correction terms has a five-point stencil due to limiters and we need to define two ghost cells at boundaries [46]. Non-reflecting boundary conditions can be achieved by using a zero-order extrapolation boundary condition and by setting U_0 and U_{-1} equal to U_1 [46]. This ensures that no waves are generated in solving the Riemann problem and in particular that there are no ingoing waves. A solid wall boundary is modelled by reflecting interior data across the boundary, with h copied directly and the momentum hu is balanced.

$$h_0 = h_1, \quad h_{-1} = h_2, \quad (hu)_0 = -(hu)_1, \quad (hu)_{-1} = -(hu)_2. \tag{3.26}$$

3.7 Conclusions

In this Chapter we have described a numerical scheme for solving the inhomogeneous SWEs with source terms in both the continuity and momentum equations. The efflux/influx was included as a source term in the continuity equation. We have also introduced a new type of wave speeds for the f-wave approach which utilises the combination of both approximate and exact Riemann solver. This new Riemann speed improves the behaviour for the propagation over nearly dry or dry states. The two-dimensional extension for the wave propagation algorithm and the f-wave approach will be explained in Chapter 5. In the next Chapter we will present the shallow water results in one-dimension.

Chapter 4 : NUMERICAL RESULTS FOR THE ONE DIMENSIONAL SWES WITH NON UNIFORM BED TOPOGRAPHIES AND LOCAL EFFLUX/INFLUX BED DISCHARGES

In this Chapter we express numerical results for the one-dimensional shallow water scheme with source terms present either in the continuity or momentum equations. This Chapter is presented into two different parts. In the first part the standard shallow water benchmarks defined in literature are considered and solved based on the proposed shallow water scheme. This includes the homogeneous problems or shallow water problems with source terms in the momentum equations that are either bathymetry gradients or friction. The second part comprises the efflux results obtained based on the source term in the continuity equations where results are compared with the general purpose Navier-Stokes solver STAR-CD.

4.1 Part I: The Standard Shallow Water Problems

To validate the numerical results, we test the numerical scheme against standard homogeneous shallow water problems or the shallow water with perturbation or over non-uniform bed topographies. Herein, we first present the existence of strong rarefaction waves then the shallow water scheme is examined for the steady-state problems with topography deviations. At the end of this part the LeVeque's perturbation test cases [46] are computed based on the proposed scheme.

4.1.1 Two Rarefaction and Nearly Dry Bed

This test case investigates the reliability of the proposed scheme in dealing with two strong rarefaction in the solution and was taken from [85]. The initial water depth is chosen to 1m and the right and left going velocities are selected equal to $u_l = -u_r = 5$ m/s. The computational domain is set equal to x=50m and the computation is then performed until time t=2.5s. Some approximate Riemann solvers based on Roe-average scheme produces a negative depth for this particular test case. Figure 4.1 illustrates the results for both depth and discharge based on the ARWS wave speeds defined in the previous Chapter.
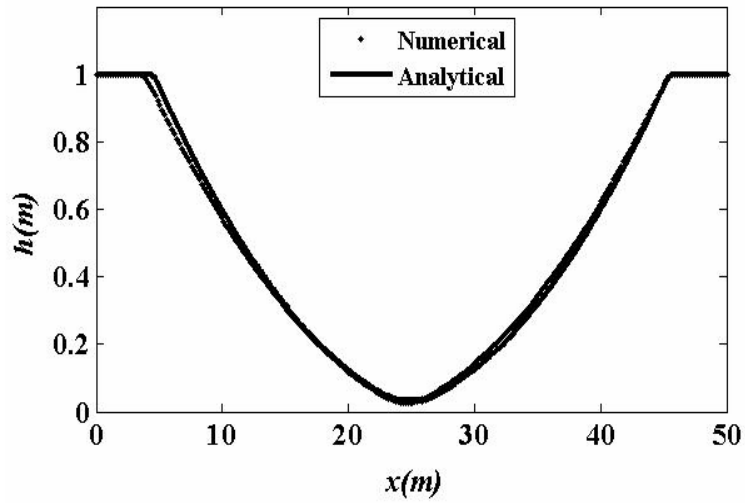
(a)
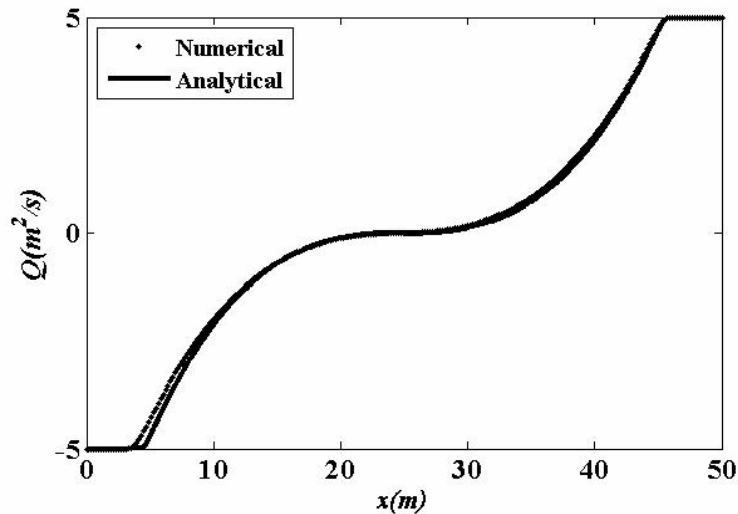
(b)

Figure 4.1. Two rarefaction and nearly dry bed based on the ARWS wave speed at *t*=2.5s. **a: Fluid depth, b: Discharge (Q).**

The computational grid cells and the CFL number were chosen equal to 512 and 0.9. As can be seen here the modified f-wave method produce nearly identical results with the analytical solution. The obtained error between the shallow water solves and analytical solution is observed at the left-going rarefaction wave. A very similar results to the modified f-wave approach have been obtained in [16].

4.1.2 Incipient Cavitation Riemann Problem

This test case has been introduced to produce dry region in the middle of two strong rarefaction waves and is devised to examine the numerical capability to treating the dry-state in the solution. The only difference between the current test case and the nearly dry
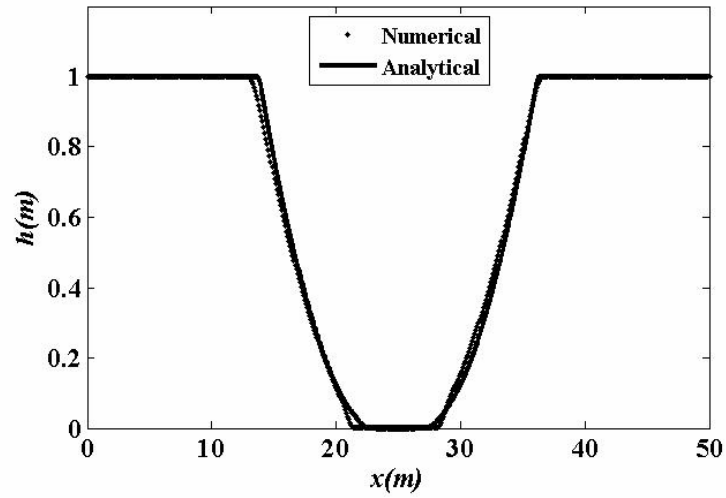
(a)
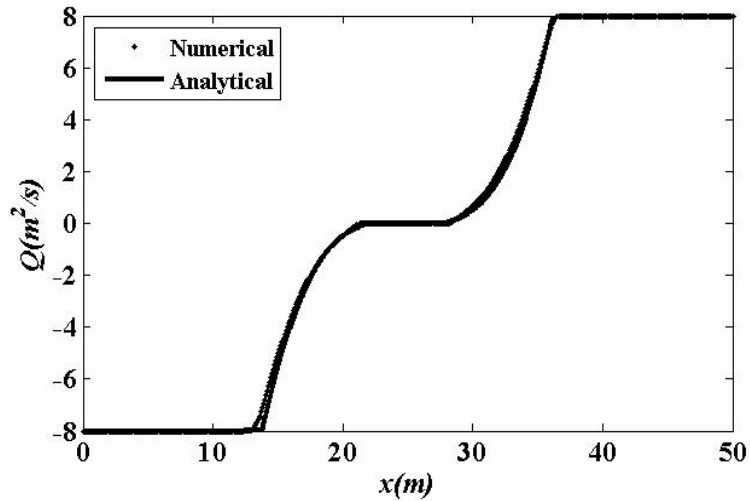
(b)

Figure 4.2. The incipient cavitation problem calculated for $t=2.5$s. a: Fluid depth, b: Discharge (Q).

bed is that the initial velocity is selected equal $u_r = -u_l = 8$ m/s to create incipient cavitation. A majority of numerical solutions have some difficulties for solving this particular test case as reported in [85]. Figure 4.2 displays the numerical results obtained based on the modified f-wave method for both depth and discharge and emphasises that the method can efficiently deal with incipient cavitation problems. Again the numerical error between the shallow water solver and the analytical solution is observed at wet/dry interface for the let rarefaction wave. The numerical results obtained here are in a close agreement with the other researches work reviewed in [85] .The computational grid cells and the CFL number were chosen equal to 512 and 0.9 respectively.

4.1.3 Steady Flow over Hump in a Rectangular Channel

The purpose of this problem is to study the conservation and suitability of the numerical scheme to model the steady-state conditions over a defined hump in the rectangular channel. Four different cases will be studied here. The difference between these test cases is the boundary conditions which impose different flow regime for the steady-state problem. The global relative error for the steady-state is defined by [89] as

$$R = \sqrt{\sum_i \left(\frac{h_i^n - h_i^{n-1}}{h_i^n} \right)^2}, \qquad (4.1)$$

where h^n and h^{n-1} are the water elevations at time levels n and $n-1$ respectively. The scheme is said to be in the steady-state when $R < 1 \times 10^{-6}$. The channel bed topography with a hump for the following test cases is given as

$$z_b(x) = \begin{cases} 0.2 - 0.05(x-10)^2, & \text{if } 8 < x < 12 \\ 0 & \text{Otherwise}. \end{cases} \qquad (4.2)$$

According to the boundary and the initial condition, the flow may be subcritical, supercritical or transcritical. The analytical solutions for these test cases was borrowed from [29]. For all of these cases the CFL number is 0.95 with 200 grid cells and extrapolation boundary conditions is used.

4.1.3.1 Flow at rest

This test case shows the quiescent flow over the hump. The initial elevation is set equal to $h(x) + z_b(x) = 2\text{m}$ and the discharge equal to zero is imposed into the left boundary to create the quiescent flow condition. Figure 4.3 demonstrates the numerical results for both discharge and fluid depth for the steady-state condition. As evident in this Figure, the proposed Riemann solver with the choice of ARWS wave speed can provide very well-balanced results. Figure 4.4 exhibits the numerical results for the similar problem obtained based on the improved HLLE solver presented in [16] which produces some oscillations for the theoretical discharge compared to the f-wave method, hence demonstrating that the new method is superior.
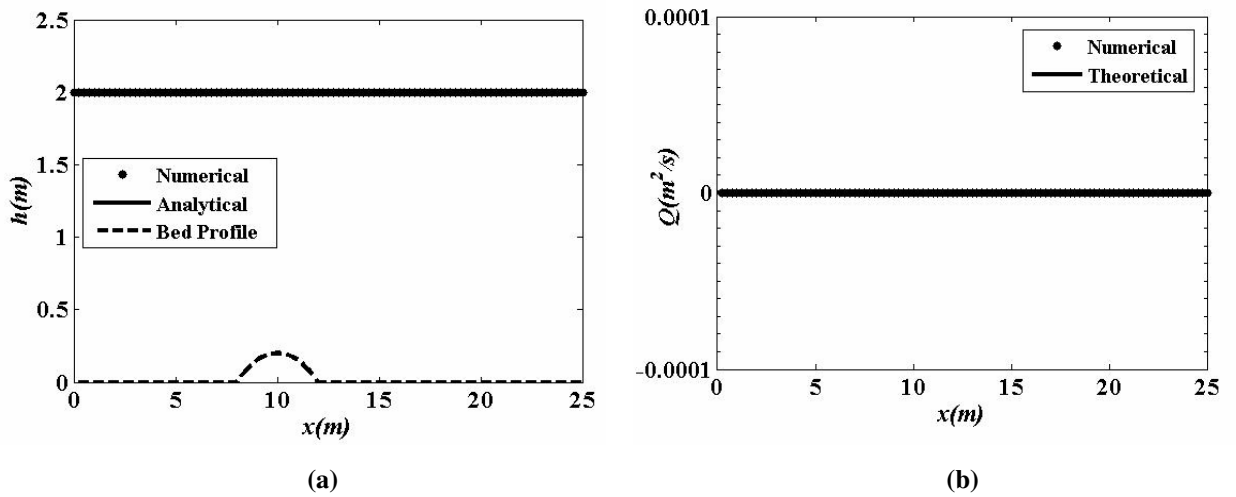
Figure 4.3. Flow at rest over hump based on the f-wave approach. a: Fluid depth, b: Discharge (Q).
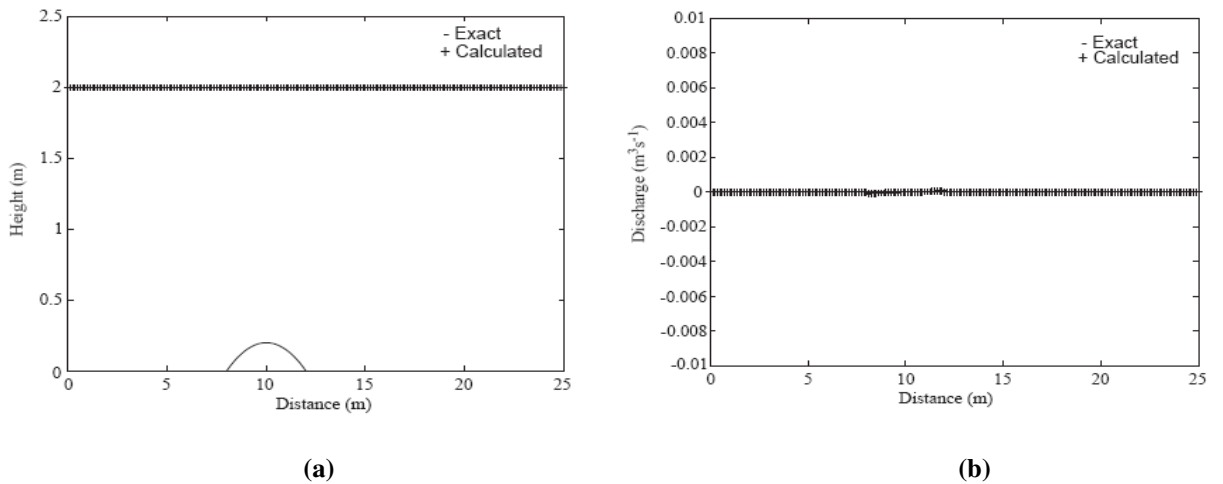
Figure 4.4. Flow at rest over hump with the improved HLLE method borrowed from [16].
(a): Fluid depth, (b): Discharge (Q).

4.1.3.2 Subcritical flow

The upstream boundary conditions impose a discharge $Q = 4.42 \text{m}^2/\text{s}$ and the downstream height is fixed at $h = 2\text{m}$. Again the initial conditions were selected to $h(x) + z_b(x) = 2\text{m}$. Figure 4.5 shows numerical results for the water elevation and discharge and indicates that the modified f-wave method provides very close results to the analytical solution. Figure 4.6 illustrates the solution for this problem with the surface gradient method (SGM) introduced in [89]. Again the SGM method produces some oscillations for the discharge and proves that it cannot exactly balance the source terms and the flux-gradient for the steady-state problems. The convergence history to achieve steady-state conditions is

74
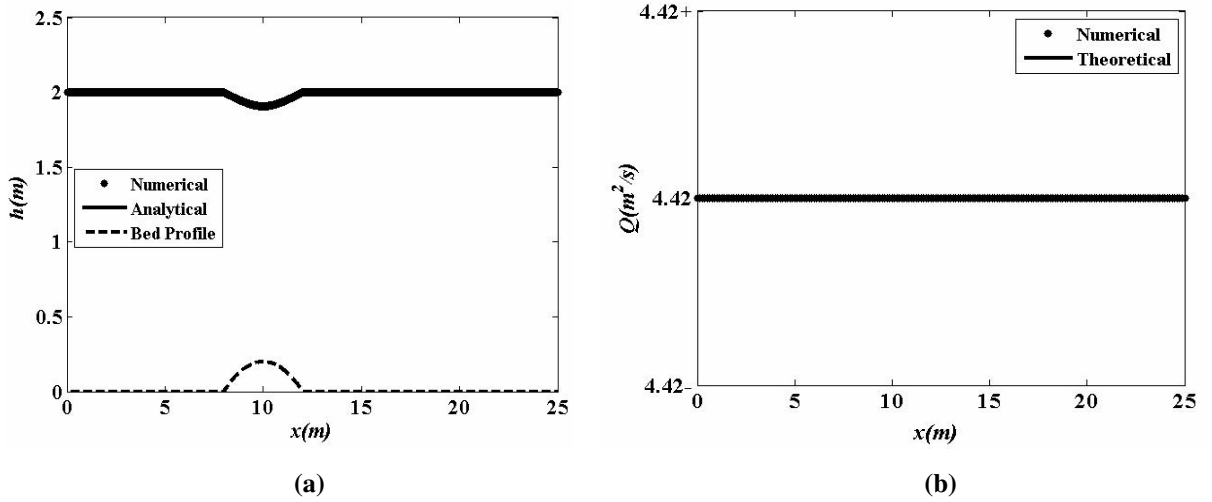
Figure 4.5. Depth (a) and discharge (b) for subcritical flow over the hump calculated by the f-wave approach where 4.42+=4.42+10^{-5} m and 4.42-=4.42-10^{-5}m.
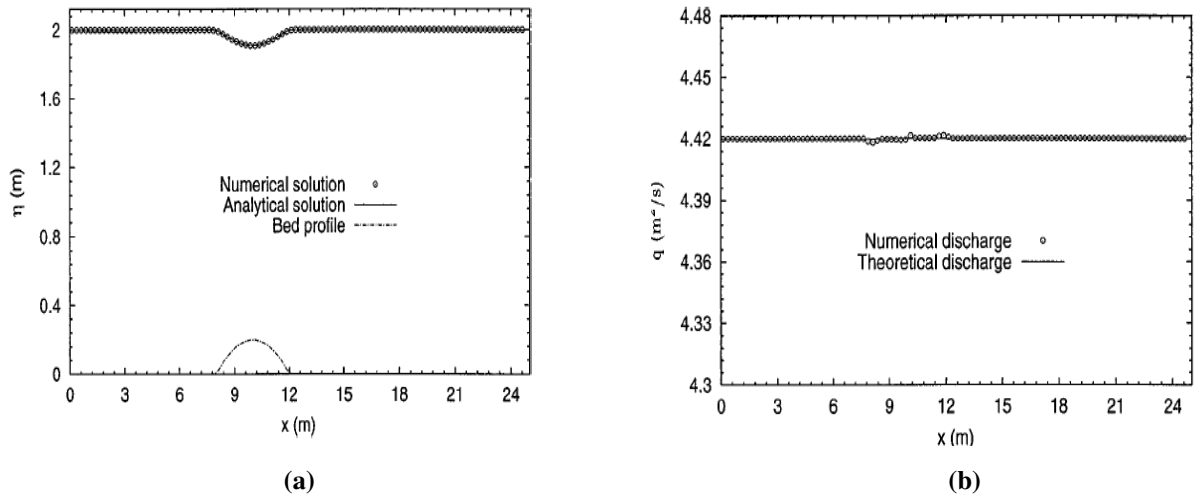
Figure 4.6. The subcritical test case borrowed from [89]. (a): Fluid depth, (b): Discharge(Q).

depicted in Figure 4.7. However, the number of iterations needed to obtain the steady-state is relatively more than number of iteration presented in [89].

4.1.3.3 Transcritical flow without shock

For this test case the upstream boundary conditions imposes a discharge equal to 1.53 m^2/s on the initial condition $h(x) + z_b(x) = 0.66$m with $Q = 0\,m^2$/s. The downstream condition is fixed at $h = 0.66$m only in the case of subcritical flow and no boundary condition is needed for the supercritical flow. Figure 4.8 displays the results for both depth and discharge based on the modified f-wave approach. As shown in this Figure the results are in very close agreement with the theoretical solution. Figure 4.9 demonstrates the similar test case solved based on the SGM scheme and borrowed from [89]. As can be seen

again the f-wave approach gives better results in terms of discharge. The convergence history was plotted in Figure 4.10 which shows that the steady-state solution was reached after 3147 iterations.
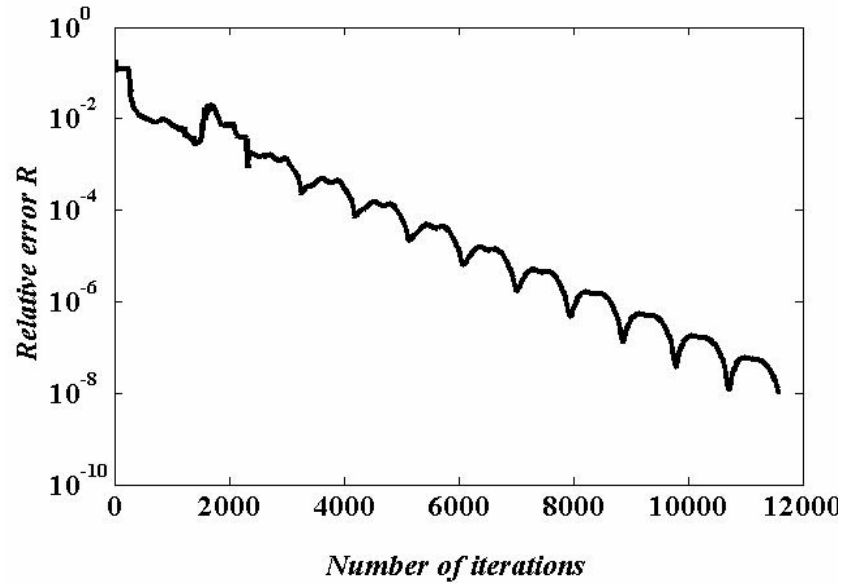
Figure 4.7. Convergence history for the subcritical flow.

| (a) | (b) |
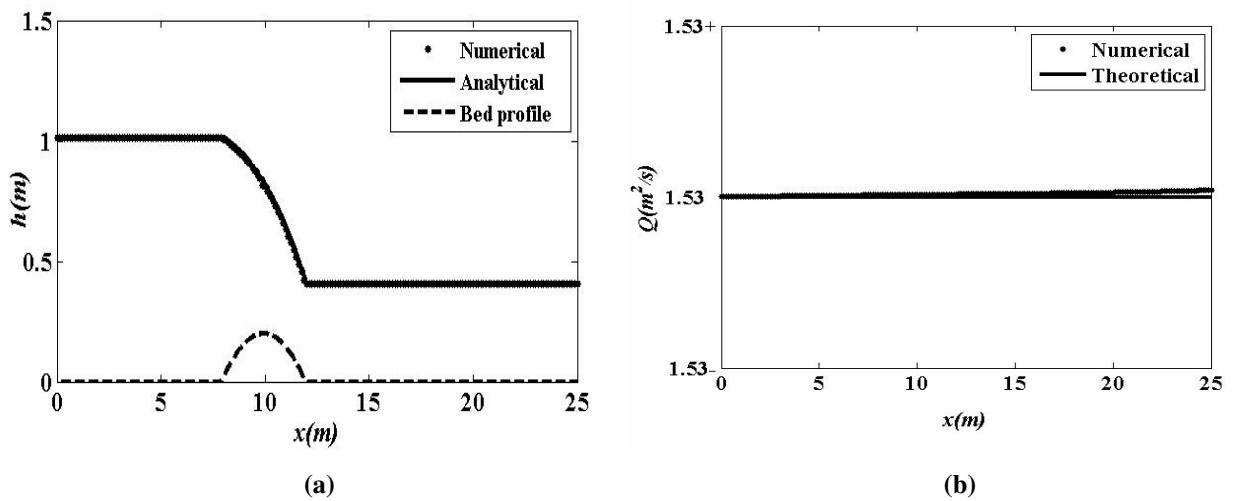
Figure 4.8. Depth (a) and discharge (b) for transcritical flow without shock over the hump calculated by the f-wave approach where 1.53+=1.53+10^{-5} m and 1.53-=1.53-10^{-5}m.
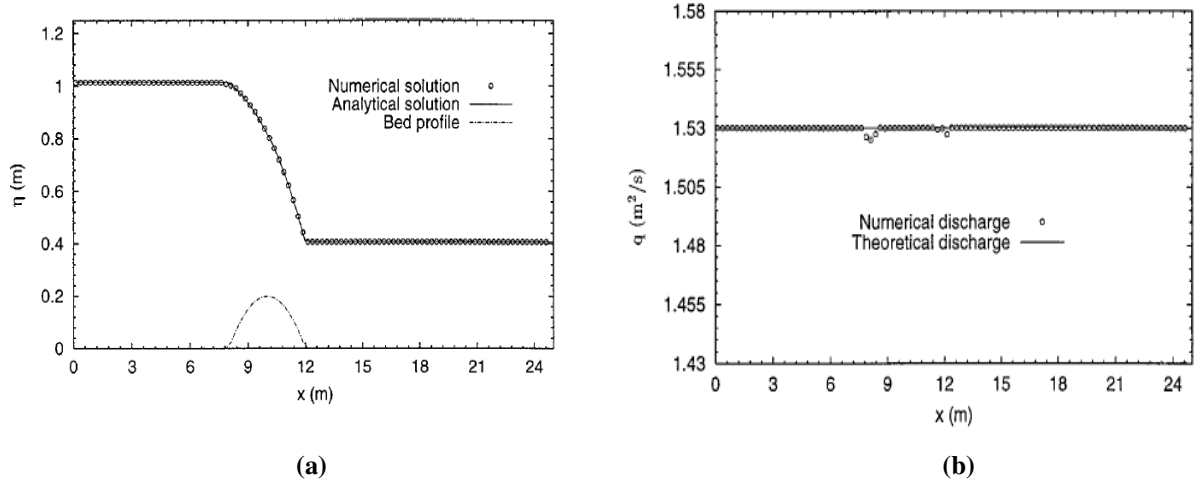
Figure 4.9. The transcritical test case without shock borrowed from [89]. (a): Fluid depth, (b): Discharge(Q).
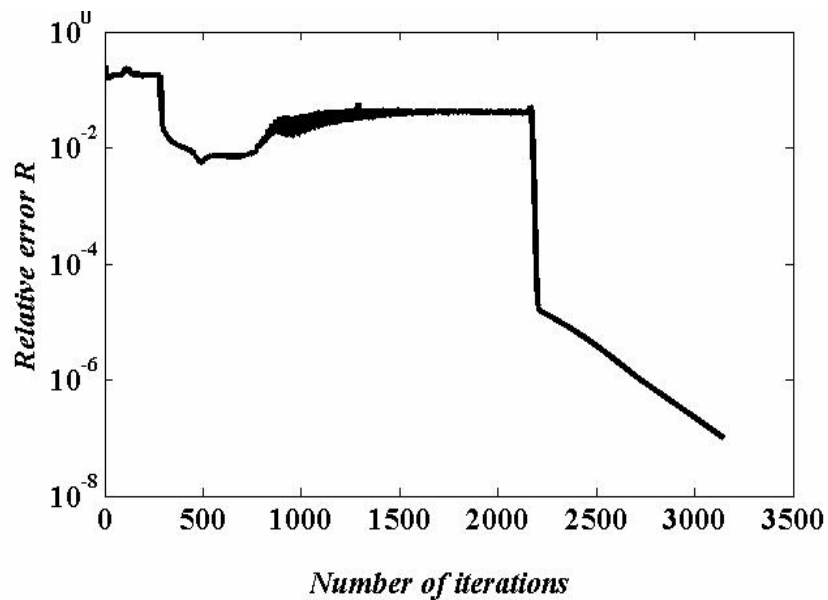
Figure 4.10. Convergence history for the transcritical flow without shock.

4.1.3.4 Transcritical flow with shock

In this test case a discharge per unit width of $Q = 0.18\text{m}^2/\text{s}$ was imposed at the upstream boundary and the downstream height was fixed at h=0.33m to make a stationary shock (hydraulic jump) on the downstream. The initial conditions for the water elevation and the discharge are $h(x) + z_b(x) = 0.33$m and $Q = 0\,\text{m}^2/\text{s}$ respectively. Figure 4.11 exhibits the numerical results for depth, discharge and the Froude number evaluated based on $Fr = V/\sqrt{gh}$ where V is the depth-averaged velocity. The only significant difference between the theoretical discharge and numerical flow is observed at the location of the shock. This is also reposted in [16, 51, 70, 90] for the transcritical flow over a hump.

77
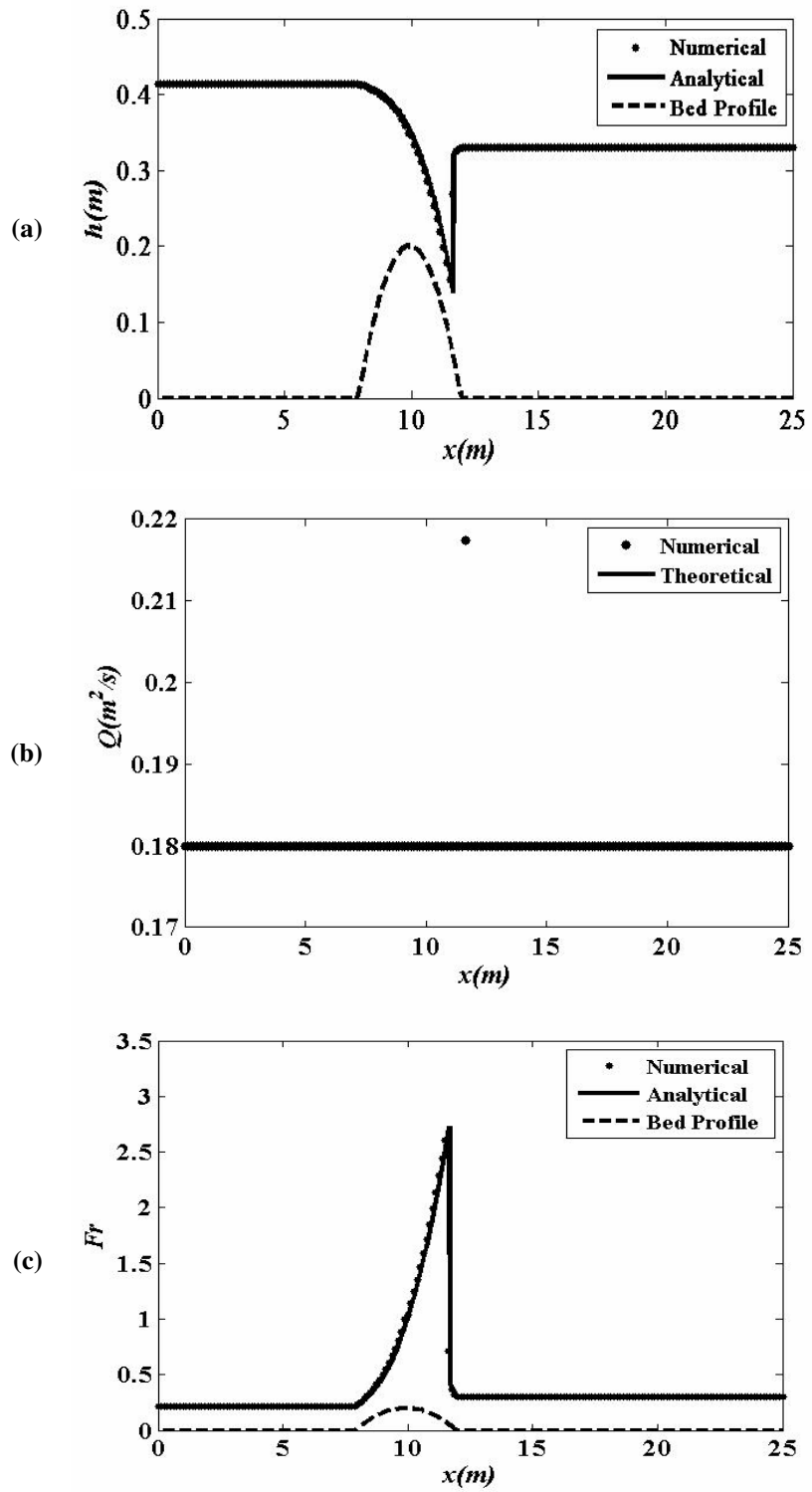
Figure 4.11. Depth (a), discharge (b) and the Froude number (c) for transcritical flow with shock with the modified f-wave approach.
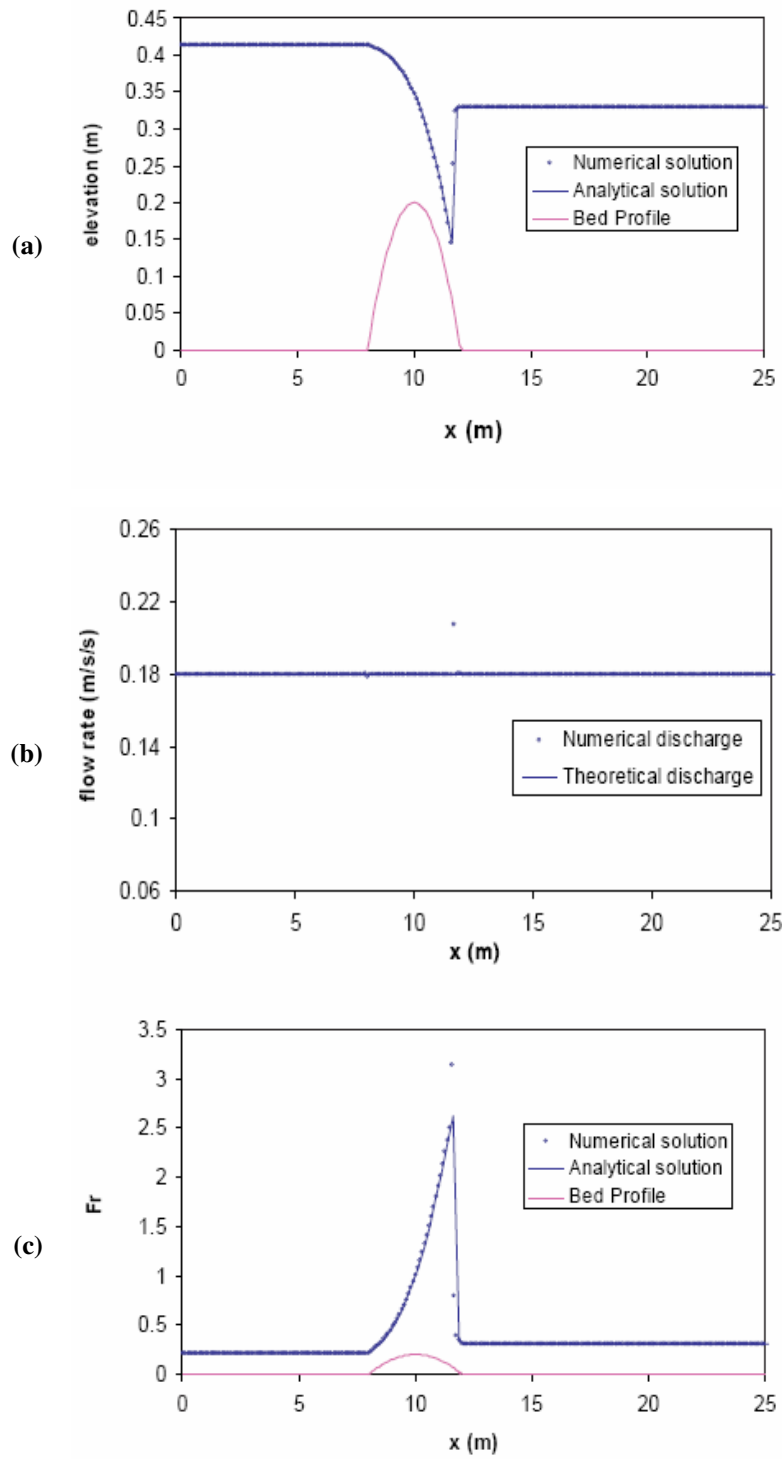
Figure 4.12. Depth (a), discharge (b) and the Froude number (c) for transcritical flow with shock done by Rogers *et al.* [70].

The underlying reason may be due to the fact that Godunov-type method does not conserve energy for shallow water flow [70]. With the exception of the flow rate at the jump the results shows nearly identical results with the analytical solution. Figure 4.12 presents the similar problem solved based on the method introduced by Rogers *et al.* described in [70]. A comparison of results verifies that the modified f-wave approach gives better results regarding discharge and Froude number. Figure 4.13 demonstrates a close up plot for discharge. Convergence history for the steady-state condition is depicted in Figure 4.14. The number of iterations to achieve steady-state for the modified approach is more than the methods presented in [70, 89]. The difference between the number of iterations may be due to the number of computational cells and the CFL number used within each method.
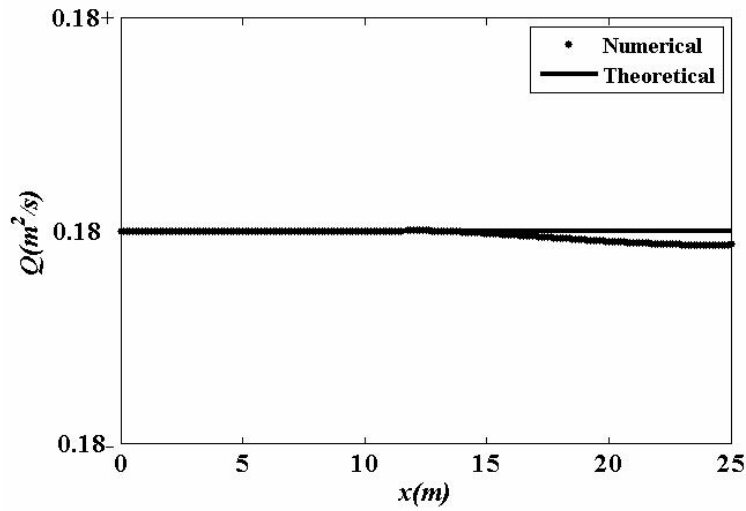
Figure 4.13. A close up demonstration for the discharge for the transcritical flow with shock computed based on the f-wave method where 0.18+=0.18+10^{-5} m and 0.18-=0.18-10^{-5}m.

4.1.4 Generation of Dry-Bed in the Middle (Vacuum) over Discontinuous Topography

The purpose of this case is to show the numerical performance of the modified f-wave approach for inhomogeneous shallow water problems with strong rarefaction wave over dry states. This problem was borrowed from [10] and was firstly defined in [24]. The computational domain is set again between $x \in [0, 25]$ and the final computational time is considered equal to $t = 0.25\text{s}$. The topography is defined as

$$z_b(x) = \begin{cases} 1 & \text{if } 25/3 < x < 12.5, \\ 0 & \text{Otherwise}. \end{cases} \tag{4.3}$$

80
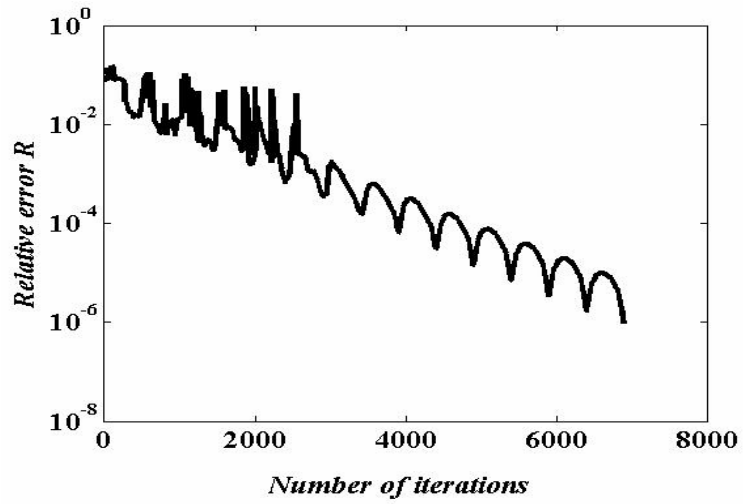
Figure 4.14. Convergence history for the transcritical flow with shock.

(a)

(b)
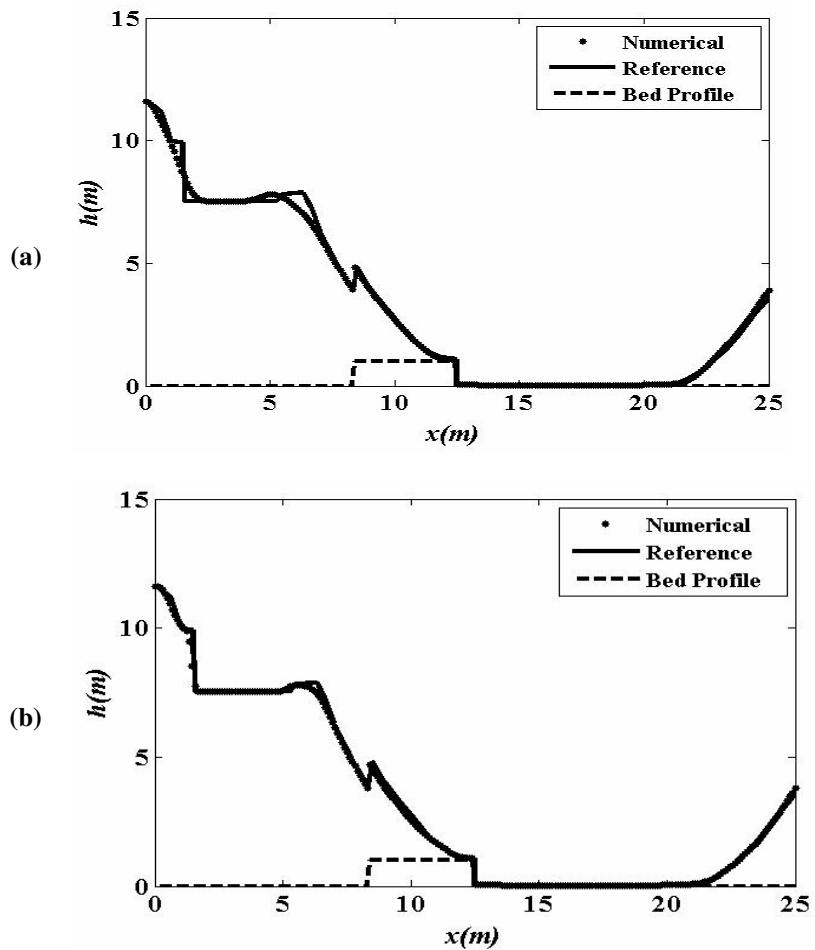
Figure 4.15. First and second accuracy using the f-wave method based on the choice of García-Navarro P wave speeds for double rarefaction problem over discontinuous topography. (a) The first-order. (b) The second-order.

The initial conditions are $h(x,0) = 10$m and

$$hu(x,0) = \begin{cases} -350 \text{ m}^2/\text{s} & \text{if} \quad x < 50/3, \\ 350 \text{ m}^2/\text{s} & \text{if} \quad x > 50/3. \end{cases} \qquad (4.4)$$

The numerical results at time $t = 0.25$s for both first-order and second-order accurate scheme based on the modified f-wave approach were illustrated in Figure 4.15 and indicates that the choice of ARWS wave speed can deal with strong rarefaction waves over the dry-state. Figure 4.16 provides different type of solutions for this particular case based on the MUSCL scheme with different limiters (Hydrostatic K and Hydrostatic S) again directly borrowed from [10]. The properties of many depth-positive methods are that they proceeded from the actual dry front. This is evident in Figure 4.16 in particular for the second-order accurate method. This is a drawback for the many numerical methods and might be due to the fact that in such schemes "the density is systematically underestimated on front" as described in [10] (see [10] for further discussion). This problem has been rectified by using the ARWS speed. To examine the effect of other limiters within the wave propagation algorithm in the case of second-order accuracy the van-Leer limiter was employed instead of MC. Very similar results to the modified f-wave approach were presented in [26].

4.1.5 Wave Propagation Problem

This test problem was first suggested by LeVeque [46] and is chosen to demonstrate the capability of the numerical methods for computation of the small perturbation occurring in the shallow water flow. The channel geometry for this case has 1m length and the equation of the hump in the bed topography was defined by

$$z_b(x) = \begin{cases} 0.25(\cos(\pi(x - 0.5)/0.1 + 1) & \text{if} \quad |x - 0.5| \leq 0.1, \\ \\ 0 & \text{Otherwise}. \end{cases} \qquad (4.5)$$
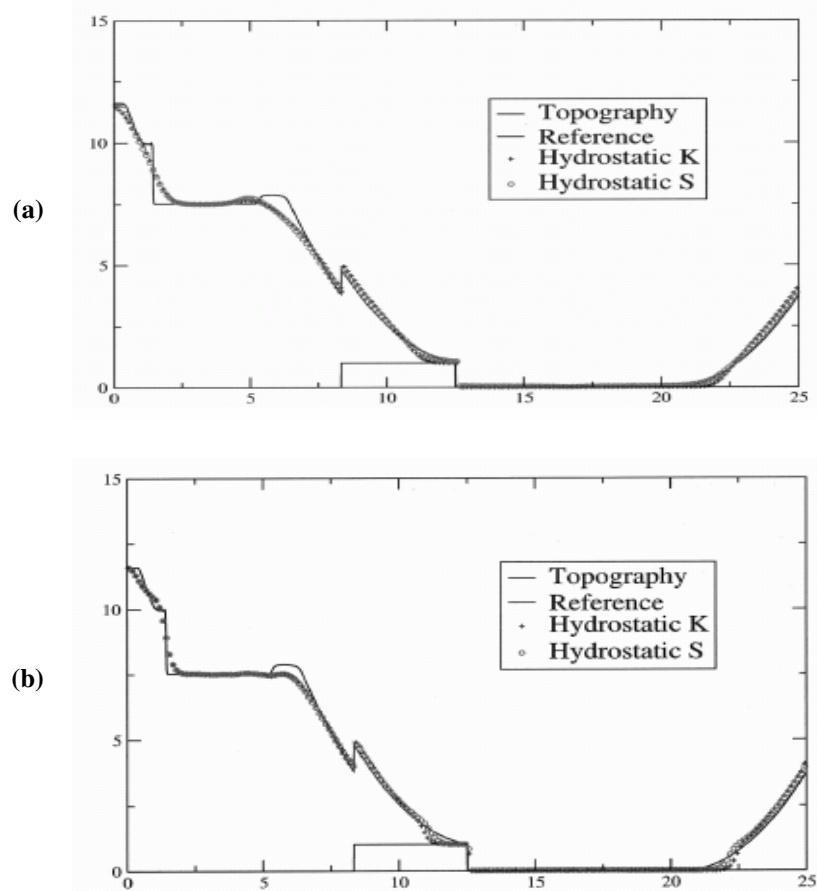
Figure 4.16. Various numerical solutions for the double rarefaction problem over discontinuous topography directly borrowed from [10]. (a) The first-order. (b) The second-order.

The magnitudes for ε, are chosen to 0.2 and 0.01 respectively and again the f-wave method is used to determine the wave speeds. The solution is obtained at time t=0.7s, using CFL=0.9 and with simple zero-order extrapolation boundary condition. Figure 4.17, illustrates the numerical results for the wave propagation problem with $\varepsilon = 0.2$. The analytical solution for this benchmark is calculated with 2000 grid cells as a fine grid based on wave propagation algorithm defined by LeVeque [46]. Close up plots for both perturbations $\varepsilon = 0.2$ and $\varepsilon = 0.01$ are depicted in Figure 4.17b and 4.17c. As can be seen in this Figure the f-wave approach provides a very close results to the LeVeque's method [46]. Theoretically for this problem the disturbance splits into waves propagating to left and right at the characteristic speeds equal to $\pm\sqrt{gh}$. Many numerical methods have difficulty for solving small perturbation problems [46]. The f-wave approach can be robustly applied for the quasi-steady and small perturbation problems and is much easier than the first wave propagation algorithm firstly described by LeVeque in [46] because the source terms are
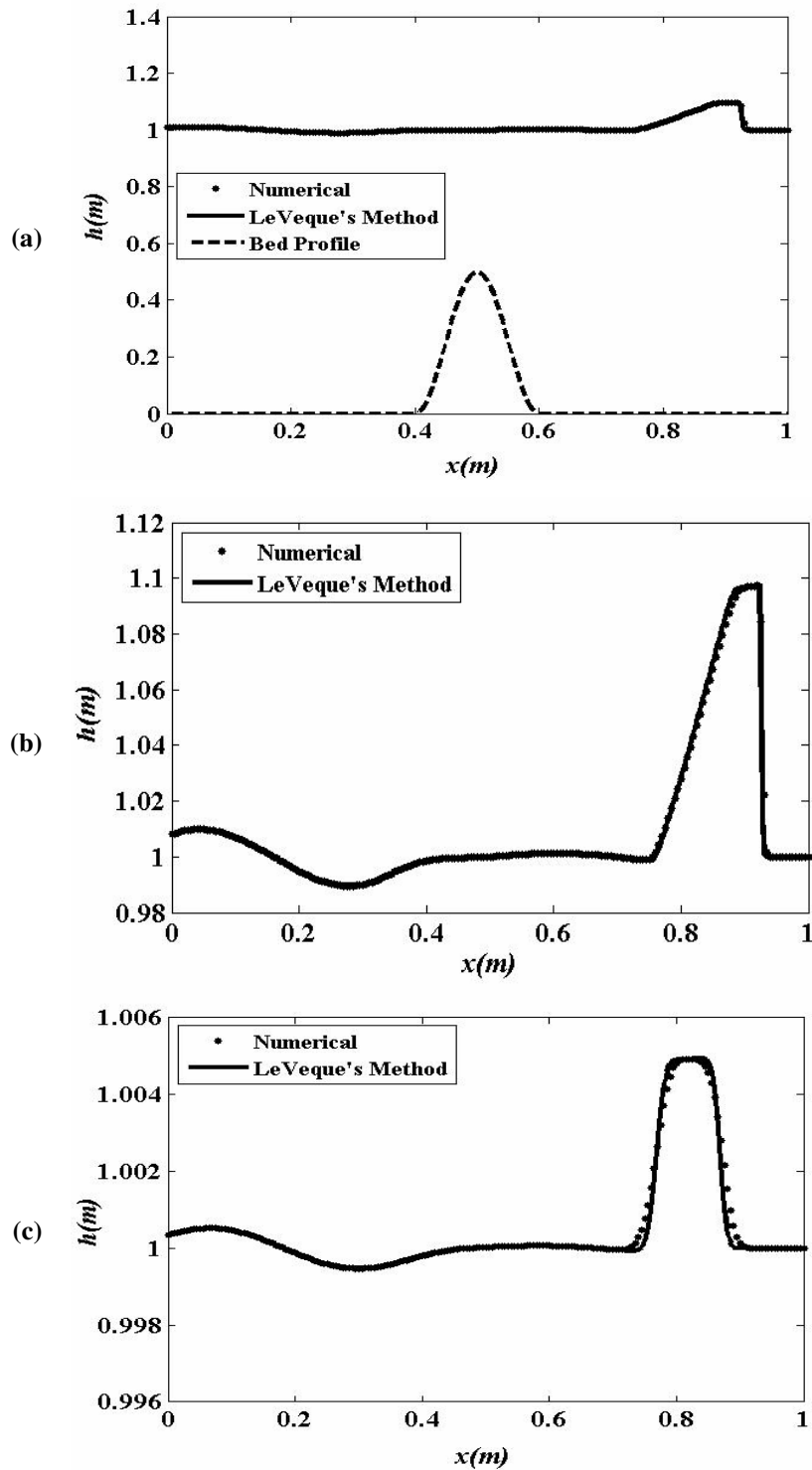
Figure 4.17. Perturbation problems solved based on the f-wave approach. (a) With perturbation $\varepsilon = 0.2$ **over the hump. (b) A close up to the solution for the perturbation with** $\varepsilon = 0.2$ **. (c) A close up to the solution for the perturbation with** $\varepsilon = 0.01$ **.**

directly treated within the flux differencing and no additional condition is needed for splitting the source terms.

4.2 Part II: The SWEs with the Efflux/Influx Source Terms

As mentioned at the beginning of this Chapter in this Section we will describe the shallow water problems with the efflux/influx source terms in the continuity equations. Comparisons then are made by the STAR-CD solver. This is applied as a two-phase volume-of-fluid (VOF) solver for water and air. The flow is generally assumed laminar and at a solid boundary there are no slip boundary conditions. Surface tension is included at a free surface. Including a turbulence modelling option $(k - \varepsilon)$ had little effect on the results as would be expected for flows dominated by inertia and gravity. The SWEs are solved with slip conditions for comparison with analytical results and with no slip conditions and bed friction for comparison with the Navier-Stokes solver. Comparison with the dry-bed dam-break case indicates that a friction coefficient $C_f = 0.015$ gives reasonable agreement with the Navier-Stokes solver and this value is used throughout. The CFL number and the computational mesh are mentioned separately for each particular test case. The modified Harten entropy fix condition [30] was used with the wave propagation algorithm to avoid non-physical results.

4.2.1 Dry Bed Dam-Break Problem

The purpose of this test case is to compare the SWE solver with the slip boundary condition with Ritter's analytical solution [35] and to compare the SWE solutions with no slip with the Navier-Stokes solver. Experimental results have shown that the flow is approximately predicted by the SWEs after the initial bore development [78]. The water depth is set to 0.3m, the depth used in the experiments, and the downstream bed is dry. The dam face is initially situated at $x = 0$ in a channel of 6m length. The numerical results obtained with the SWEs are shown in Figure 4.18 along with the computed Navier-Stokes result and the analytical solution for the water motion at different times. The solution was evaluated at times $t = 0.4$s, 0.6s, 0.8s and t=1s with 512 grid cells for the SWEs and a CFL number equal to 0.9. In order to plot the free-surface for the VOF-based Navier-Stokes STAR-CD solver, the interface VOF value to define the free surface is 0.5, the value for water being 1 and for air 0. Ritter's analytical solution for the problem is given by [35]

$$u = \frac{2}{3}\left(\frac{x'}{t} + \sqrt{gh_u}\right), \quad c = \frac{1}{3}\left(2\sqrt{gh_u} - \frac{x'}{t}\right); \quad c = \sqrt{gh}, \tag{4.7}$$

where h_u is the initial water depth and x' represents the horizontal distance from the initial dam location at time t. As can be seen here the frictionless SWEs show very good agreement with Ritter's solution whilst the SWEs with bed friction and $C_f = 0.015$ approximately coincide with the Navier-Stokes solutions. This value of C_f will be used in all simulations and justifies the use of the Navier-Stokes solver for further comparisons.

4.2.2   Efflux over a Dry Bed

This problem is defined by the efflux number $En = V / \sqrt{gl}$ where g is acceleration due to gravity, l is the width of efflux slot and V denotes velocity of the efflux (other dimensionless numbers are possible which may include the depth, or the horizontal depth-averaged velocity, but these become difficult to apply and generalise when effluxes are flowing over initially dry beds). The slot width is set somewhat arbitrarily to 10cm with exit velocities of 1m/s, 0.5m/s, 0.3 and 0.2m/s giving Efflux numbers En = 1.009, 0.504, 0.302 and 0.201 which will be seen to be a relevant range. The computational domain is 20m in length with the slot situated at the origin between -5cm and 5cm in the longitudinal direction. For the waves propagating over dry areas no shock waves exist and only rarefaction waves should appear in the solutions. Results are shown in Figures 4.19 to 4.21 for En= 1.009, 0.504 and 0.302 at times t=0.5s, t=1s, t=4s and t=8s. Note that a non-dimensional time could be given by $t / \sqrt{l/g}$ or tV / l but since it is not clear which is most appropriate we describe the results in terms of real time. The plots show the upwards jet of water, and water flowing away from the entry slot. As can be seen in Figure 4.19, there is a noticeable discrepancy between the SWE and the Navier-Stokes results for En= 1.009 at time t=0.5s and t=1s. The Navier-Stokes results show symmetric air cavities as the jet propagates upwards as a fountain and then falls down. This effect becomes less marked but is still visible for time t=4s and t=8s and the SWEs capture the front positions quite well. The air cavities are just visible with En= 0.504 and as the efflux number decreases the effect of the flow above the slot become less prominent and the SWEs exhibit closer agreement with the Navier-Stokes solution for the earlier times, as seen in Figures 4.20 and 4.21. For the SWEs computation 1024 grid cells with a CFL number equal to 0.35
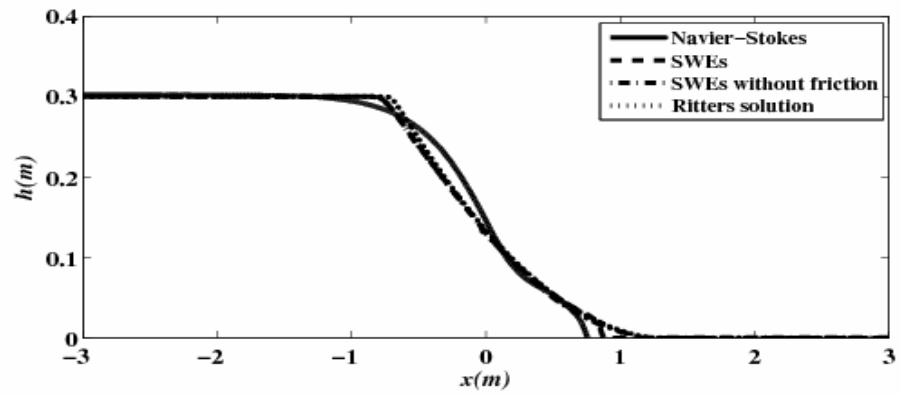
(a) *t*=0.4s
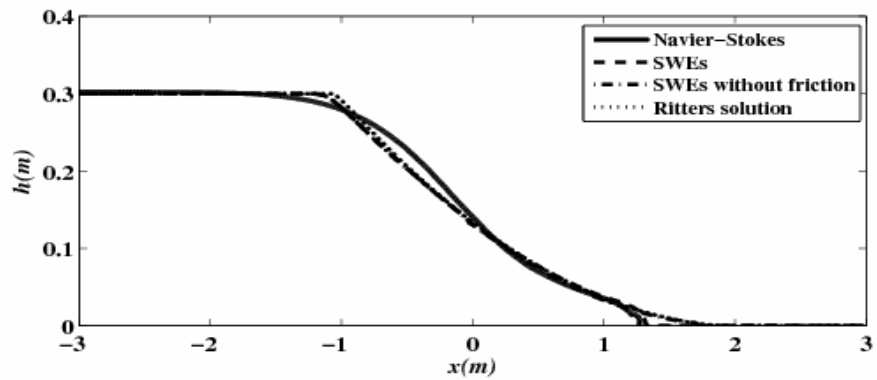
(b) *t*=0.6s
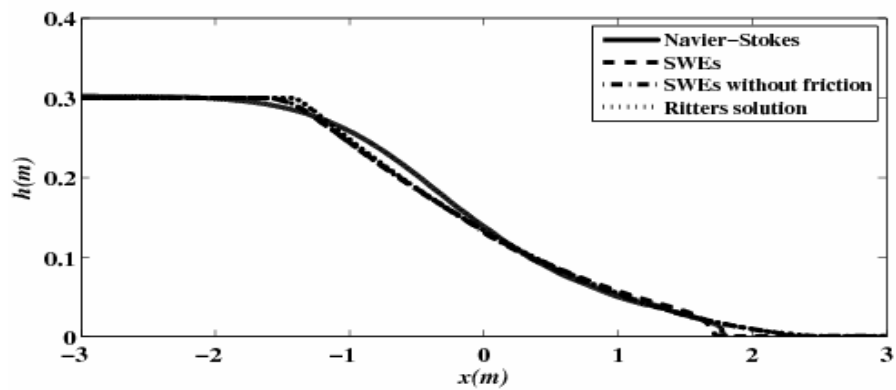
(c) *t*=0.8s
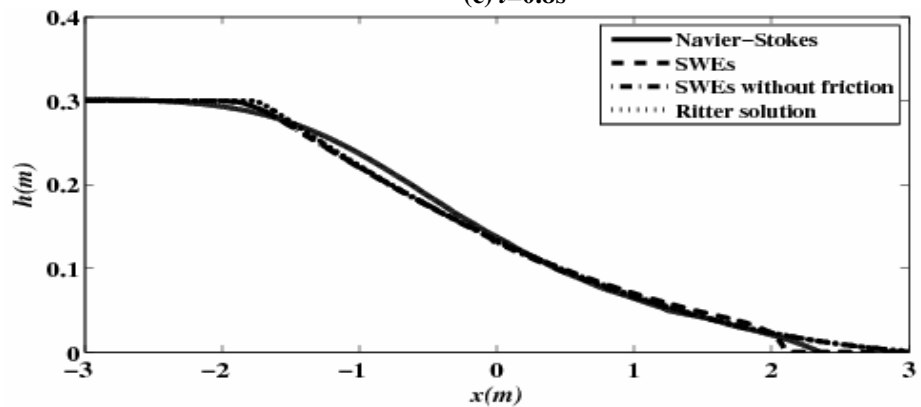
(d) *t*=1s

Figure 4.18.The dam-break problem with initial water depth h=0.3 for different times solved based on Navier-Stokes equation, frictionless SWEs, SWEs with the friction term and the Ritter's solution.
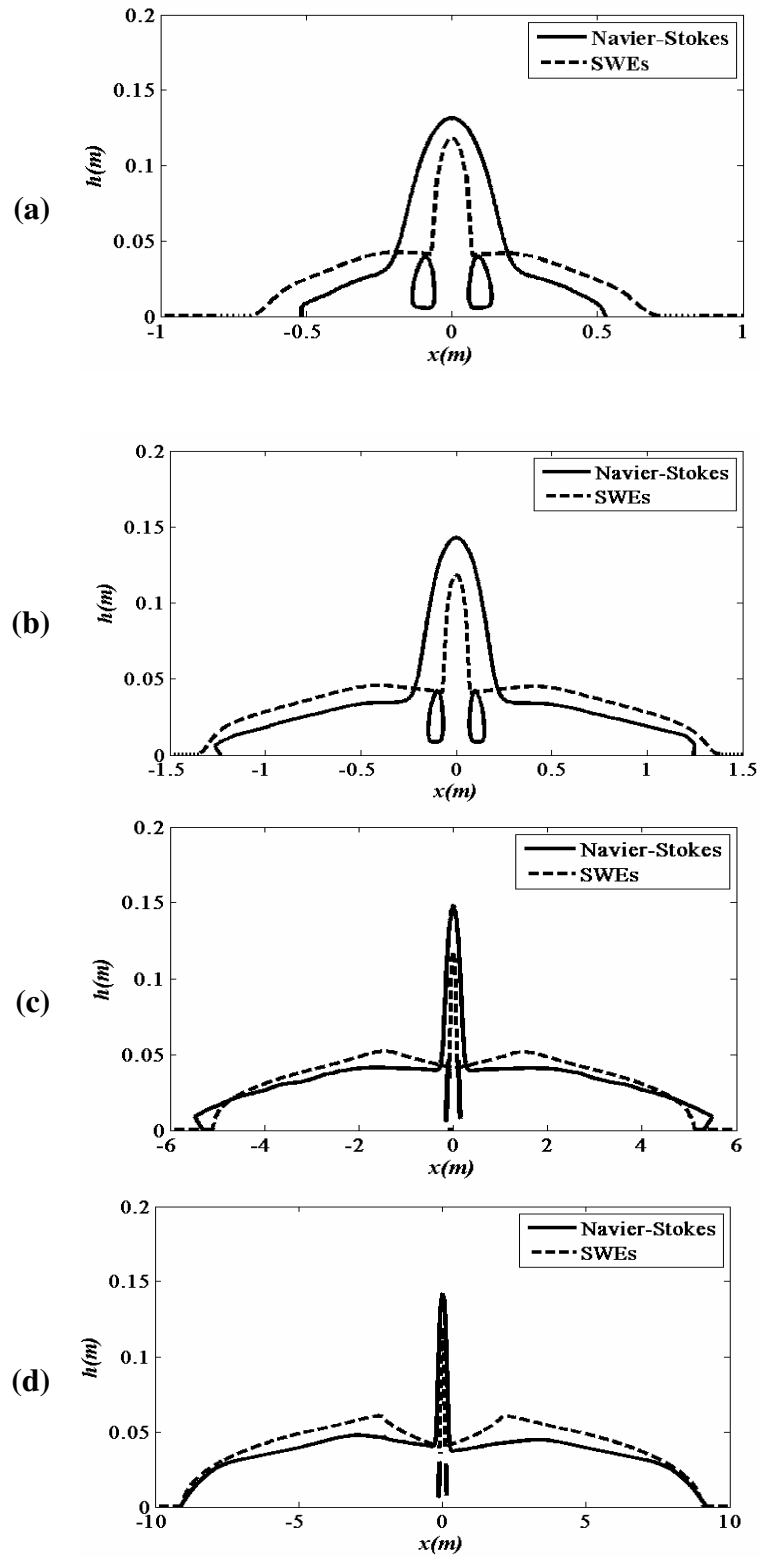
Figure 4.19. Efflux problem over dry-state for *En*=1.009 for time *t*=0.5s, *t*=1s, *t*=4s and *t*=8s (a-d).
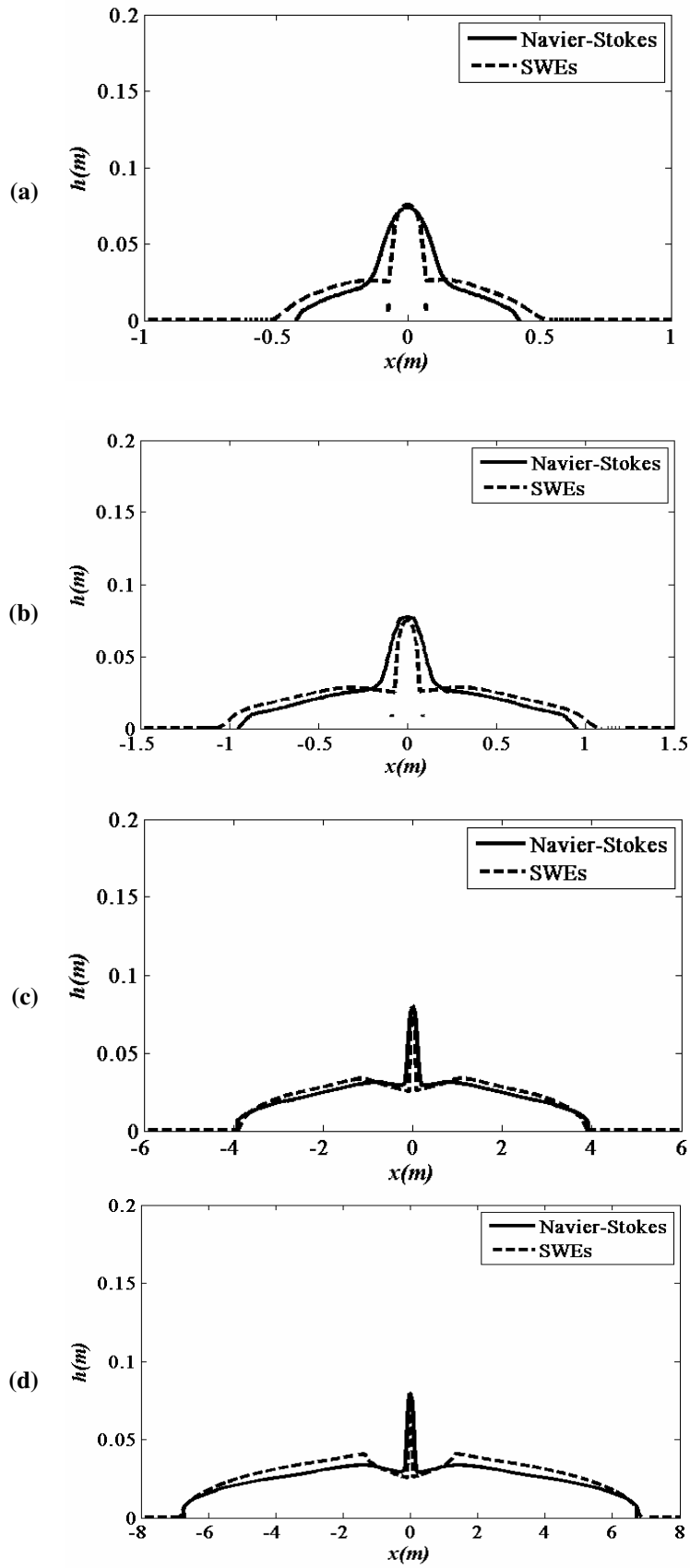
Figure 4.20. Efflux problem over dry-state for *En*=0.504 for time *t*=0.5s, *t*=1s, *t*=4s and *t*=8s (a-d).
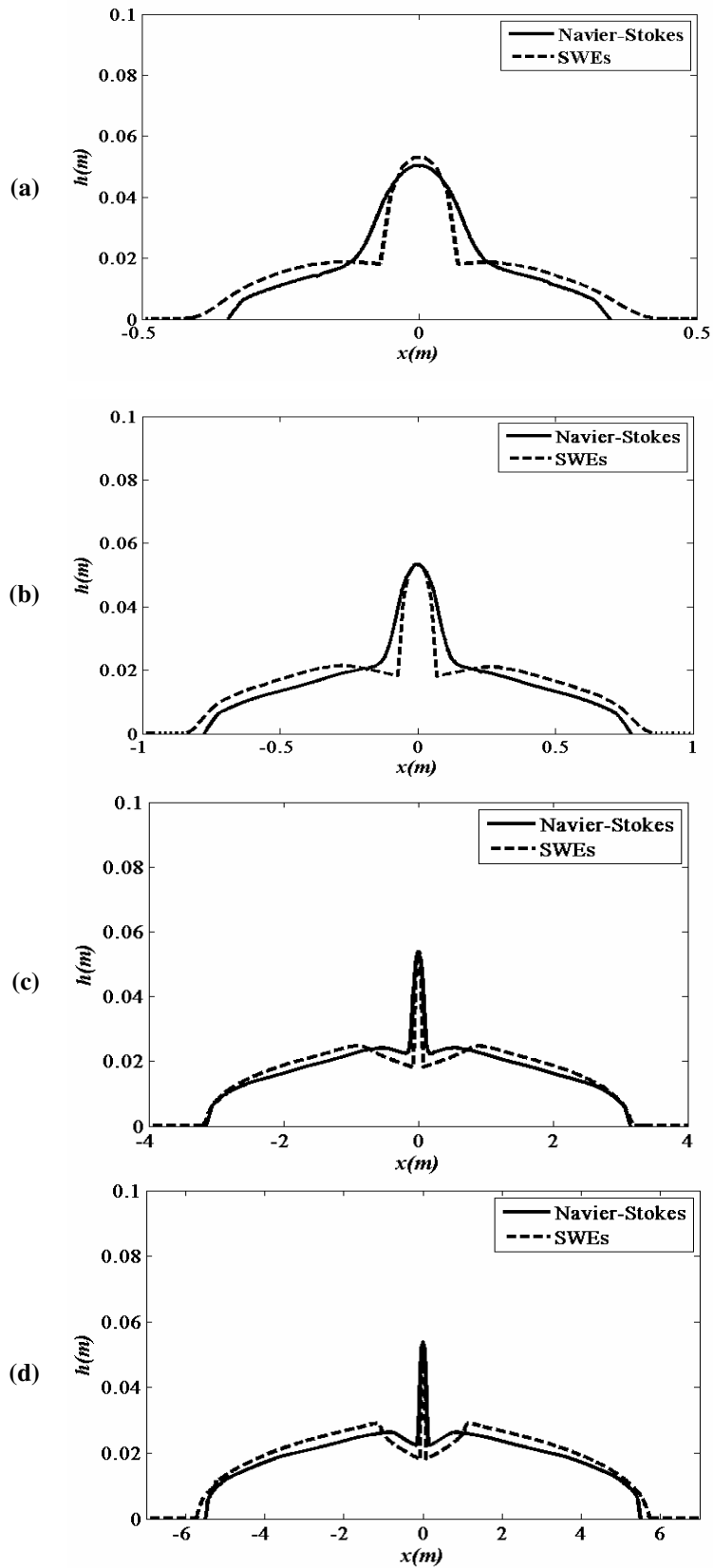
Figure 4.21. Efflux problem over dry-state for *En*=0.302 for time *t*=0.5s, *t*=1s, *t*=4s and *t*=8s (a-d).

(a)

(b)

(c)

(d)

(e)

(f)
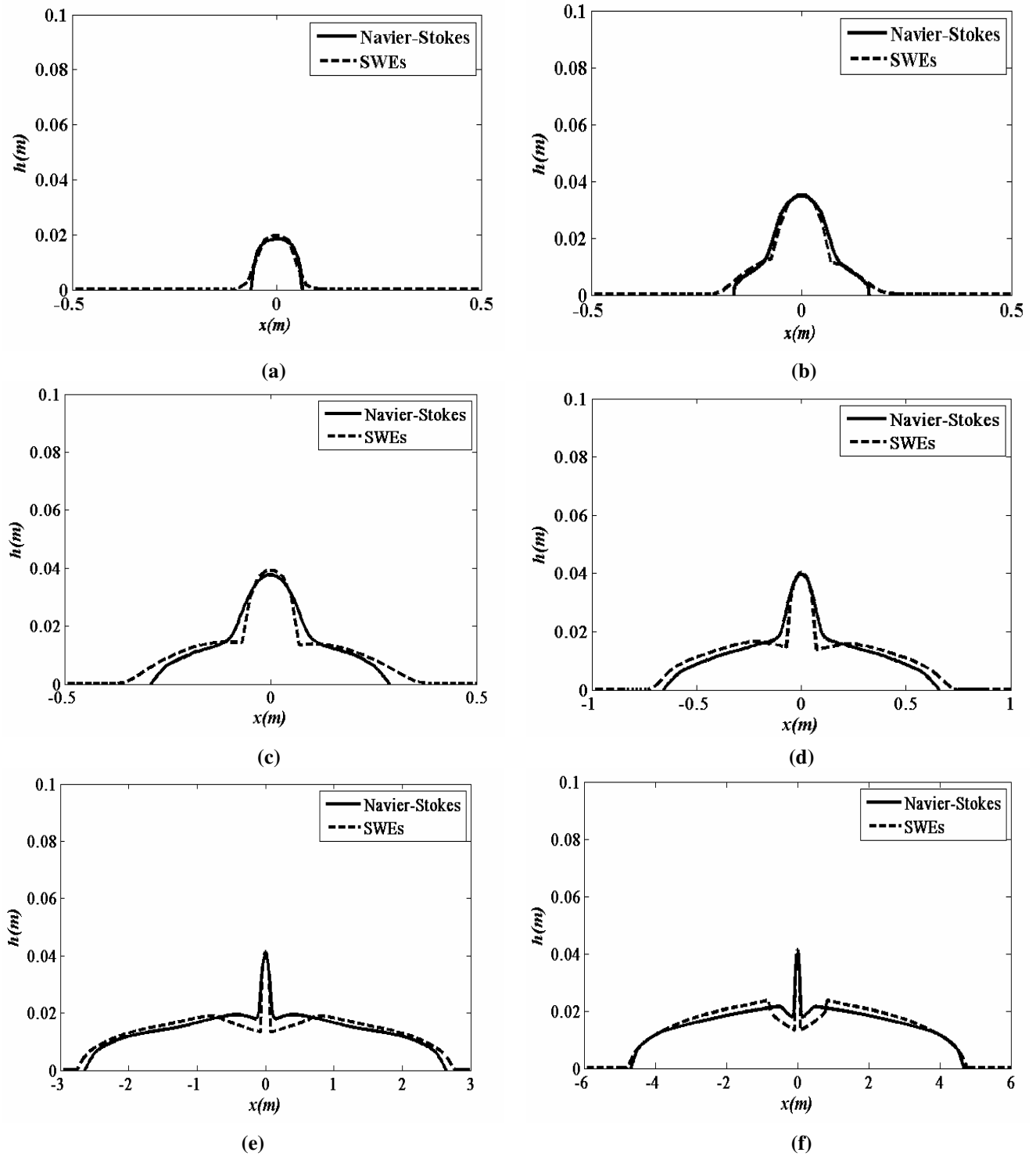
Figure 4.22. Efflux problem over dry-state for different for *En* number equal to 0.201 for time for time t=0.1s, *t*=0.3s, *t*=0.5s, *t*=1s, *t*=4s and *t*=8s (a-f).

were used. The VOF calculation used 4096 longitudinal and 64 vertical cells. Halving the number of cells had no effect on the results within plotting accuracy. Figure 4.22 shows results for the efflux velocity of 0.2m/s giving $En= 0.201$ for $t= 0.1$s and 0.3s as well as 0.5s, 1s, 4s and 8s. This shows the remarkably close agreement with the Navier-Stokes solutions for very small times. Tables 4.1-4.4 show the l_2 and l_∞ error between the SWEs and Navier-Stokes equation which were calculated as

$$l_2 = \frac{\sqrt{\sum_i (ds_i)^2}}{N} \qquad and \qquad l_\infty = \max(ds_i),$$ (4.8)

where ds_i denotes the discrepancy between the SWEs and Navier Stokes depth obtained based on STAR-CD that is, $ds_i = d_{N-S} - d_{SWEs}$. We also computed the non-dimensional error evaluated by dividing over the maximum depth for the STAR-CD solver and indicate the percentage error. Using l_∞ allows us to quantify the largest difference for water elevation between STAR-CD and the SWEs, while l_2 allows us to quantify the average error over the domain. As can be seen in these tables and Figures 4.19-4.22, the maximum of the error is seen at the location of the slot or at the wave front which may be due to the viscous terms or non-hydrostatic pressure. The values for l_2 show that for the low efflux numbers, the average error is less than 5%, while for the higher efflux numbers, the average error is less than 8%.

4.2.3 Efflux over a Wet Bed

This case examines the behaviour of the scheme with outflow into areas that are already wet, using the same dimensions. The initial depth of water in the channel was assumed to be 0.012m. The numerical SWE scheme again was used with 1024 computational cells with a CFL number of 0.35. The STAR-CD simulation was performed using a converged mesh containing 2048 horizontal and 32 vertical grid cells. Figures 4.23-4.26 show results for $En= 1.009, 0.504, 0.302$ and 0.201 given by efflux velocity $V = 1$m/s, 0.5m/s, 0.3 and 0.2m/s, for different times. As can be seen again in Figure 4.23, similar to the dry states cases in the previous Section, the Navier-Stokes results show symmetric air cavities as the

Table 4.1. The l_2 and l_∞ error and non-dimensional norms for the efflux problem over dry-state and *En*= 1.009.

Time(s)	l_2	l_2/d_{max}	l_∞	l_∞/d_{max}
0.5	7.5×10^{-3}	5.7×10^{-2}	7.9×10^{-2}	6×10^{-1}
1	9.3×10^{-3}	6.5×10^{-2}	9.2×10^{-2}	6.4×10^{-1}
4	1×10^{-2}	7.3×10^{-2}	9.8×10^{-2}	6.6×10^{-1}
8	1.1×10^{-2}	7.8×10^{-2}	9.4×10^{-2}	6.7×10^{-1}

Table 4.2. The l_2 and l_∞ error and non-dimensional norms for the efflux problem over dry-state and *En*= 0.504.

Time(s)	l_2	l_2/d_{max}	l_∞	l_∞/d_{max}
0.5	2.5×10^{-3}	3.1×10^{-2}	1.8×10^{-2}	2.4×10^{-1}
1	3.3×10^{-3}	4.1×10^{-2}	4.2×10^{-2}	5.6×10^{-1}
4	3.6×10^{-3}	4.5×10^{-2}	4.2×10^{-2}	5.6×10^{-1}
8	5.1×10^{-3}	6.3×10^{-2}	4.2×10^{-2}	5.6×10^{-1}

Table 4.3. The l_2 and l_∞ error and non-dimensional norms for the efflux problem over dry-state and *En*= 0.302.

Time(s)	l_2	l_2/d_{max}	l_∞	l_∞/d_{max}
0.5	1.2×10^{-3}	1.2×10^{-2}	7×10^{-3}	1.3×10^{-1}
1	1.6×10^{-3}	2.9×10^{-2}	2.2×10^{-2}	4×10^{-1}
4	1.9×10^{-3}	3.5×10^{-2}	2.3×10^{-2}	4.2×10^{-1}
8	2.7×10^{-3}	5×10^{-2}	2.3×10^{-2}	4.2×10^{-1}

Table 4.4. The l_2 and l_∞ error and non-dimensional norms for the efflux problem over dry-state and *En*= 0.201.

Time(s)	l_2	l_2/d_{max}	l_∞	l_∞/d_{max}
0.1	5.4×10^{-4}	1.3×10^{-2}	3.7×10^{-3}	8.9×10^{-2}
0.3	3.8×10^{-4}	9.2×10^{-2}	4.7×10^{-3}	1.1×10^{-1}
0.5	6.9×10^{-4}	1.6×10^{-2}	6.1×10^{-3}	1.4×10^{-1}
1	9.3×10^{-4}	2.2×10^{-2}	4.9×10^{-3}	1.2×10^{-1}
4	1.5×10^{-3}	3.6×10^{-2}	4.9×10^{-3}	1.2×10^{-1}
8	1.9×10^{-3}	4.6×10^{-2}	3.1×10^{-3}	7.5×10^{-2}

jet propagates upwards. For the initial times a large difference is observed between the STAR-CD solver and the SWEs again due to the non-hydrostatic pressure in the Navier-Stokes equations. This effect becomes less important for the larger times and both equations give the same results for the water fronts propagating over wet states. For the progressively smaller efflux velocities in Figures 4.24-4.26, initially both schemes show the same behaviour as expected. For larger times the SWE scheme predicts shock waves propagating over a wet bed. The Navier-Stokes solution predicts a slightly smoother transition to still water in keeping with experimental observation [78]. Tables 4.5-4.8 show the l_2 and l_∞ errors for the SWEs and Navier-Stokes; the maximum discrepancy occurs at the slot and the average error or discrepancy for long times remains less than 4% for $En=$ 0.504, 0.302 and 0.201, (for $En=$ 0.201, the average error reaches 9% due to initial transients) but for $En=$ 1.009 the average error is much larger, 40%, due to the non-hydrostatic pressure effects.

4.2.4 Dam-Break over a Dry Bed with Efflux

This test case represents a step towards a dam-break with multiple bed connections. Only efflux is considered to study the resulting interaction of rarefaction waves which lead to shock waves. Clearly this is quite a complex flow because of the collision of two rarefaction waves on the dry area which has not previously been studied using Godunov-type methods to our knowledge. Similar initial conditions are set up but the domain is now 6 m long with the dam front at the mid point (x=0m). The efflux slot is situated between x = 1.24m and 1.74m in the dry bed. At the initiation of the dam-break an efflux velocity of 0.1m/s is also imposed, giving a small efflux number of 0.0452. For the SWEs the CFL condition was 0.5 and 512 grid cells were used. For the STAR-CD calculation a converged mesh of 1024×32 cells in the horizontal and vertical directions was used.

Numerical results are presented in Figure 4.27 for different times. In Figure 4.27a, we can see the dam-break flow approaching the efflux region. In successive plots we can see that rarefaction waves approach each other around x =1.2m which creates a sharp vertical upthrust of water when they collide which is higher than the efflux discharge. In general, the results of the SWEs are in good agreement with the Navier-Stokes solution including the shock created at the collision point. As expected due to their depth-averaged nature, the greatest discrepancy occurs at the tip of this collision point where the SWEs cannot model the rapid change in vertical acceleration.
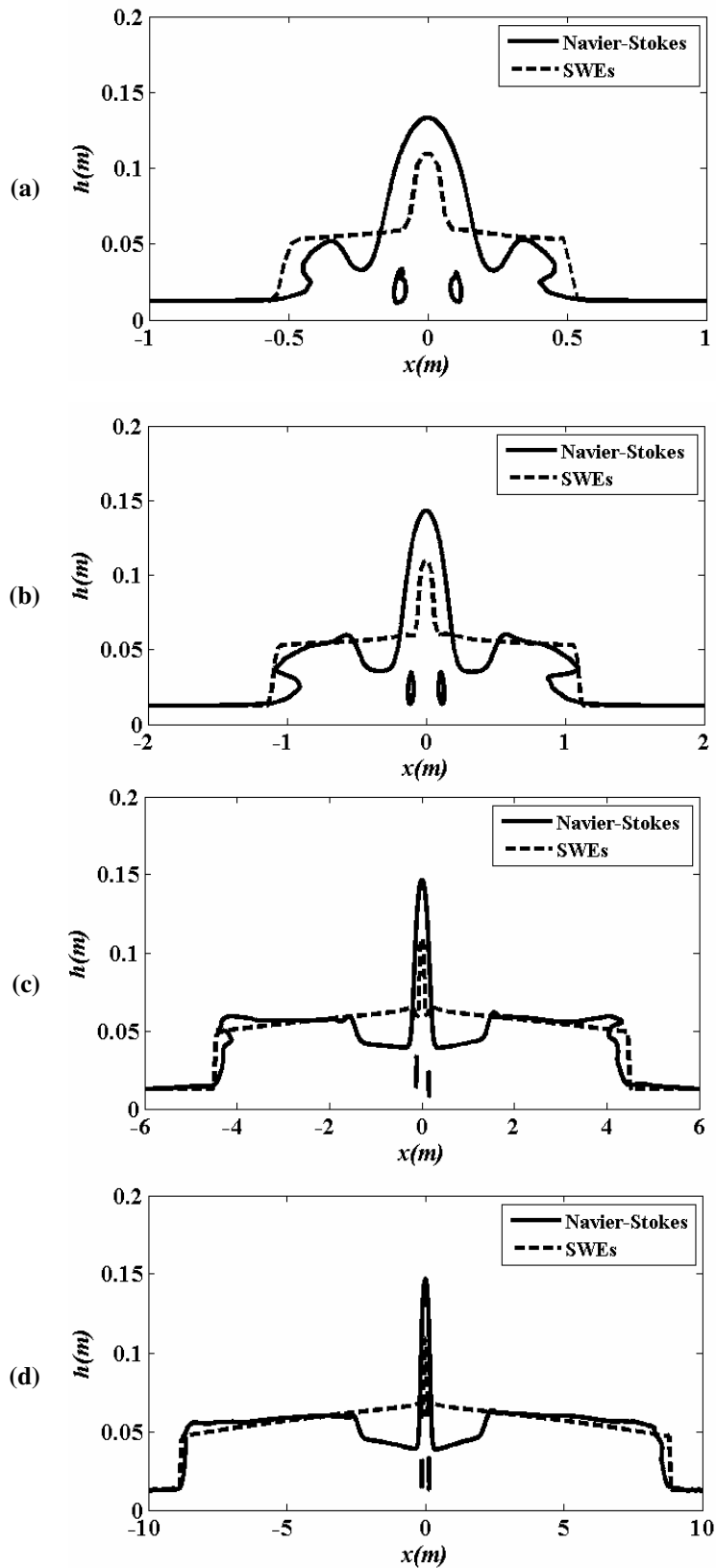
Figure 4.23. Efflux problem over wet states for different times and the *En* number equal to 1.009 for time for time *t*=0.5s, *t*=1s, *t*=4s and *t*=8s (a-e).
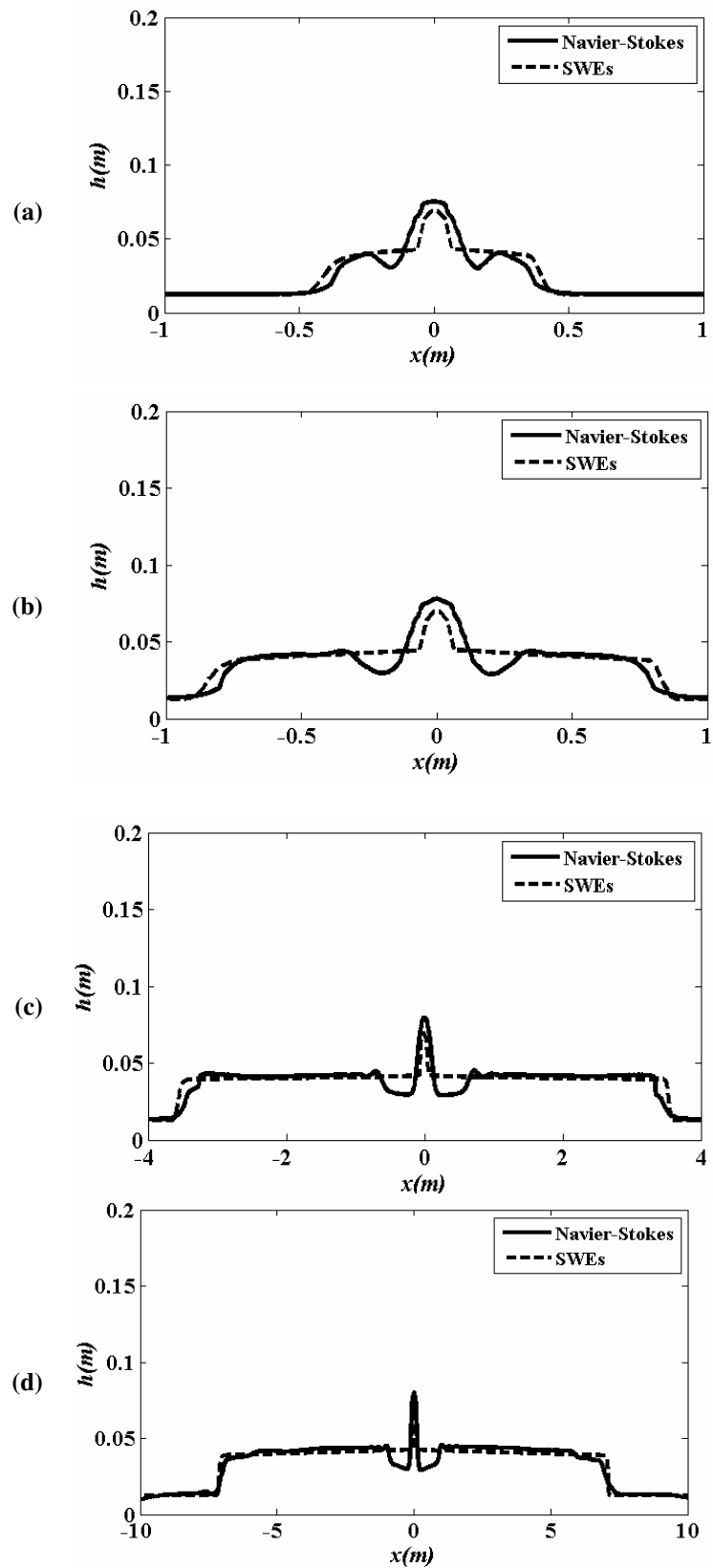
Figure 4.24. Efflux problem over wet states for different times and the _En_ number equal to 0.501 for time for time t=0.5s, t=1s, t=4s and t=8s (a-d).
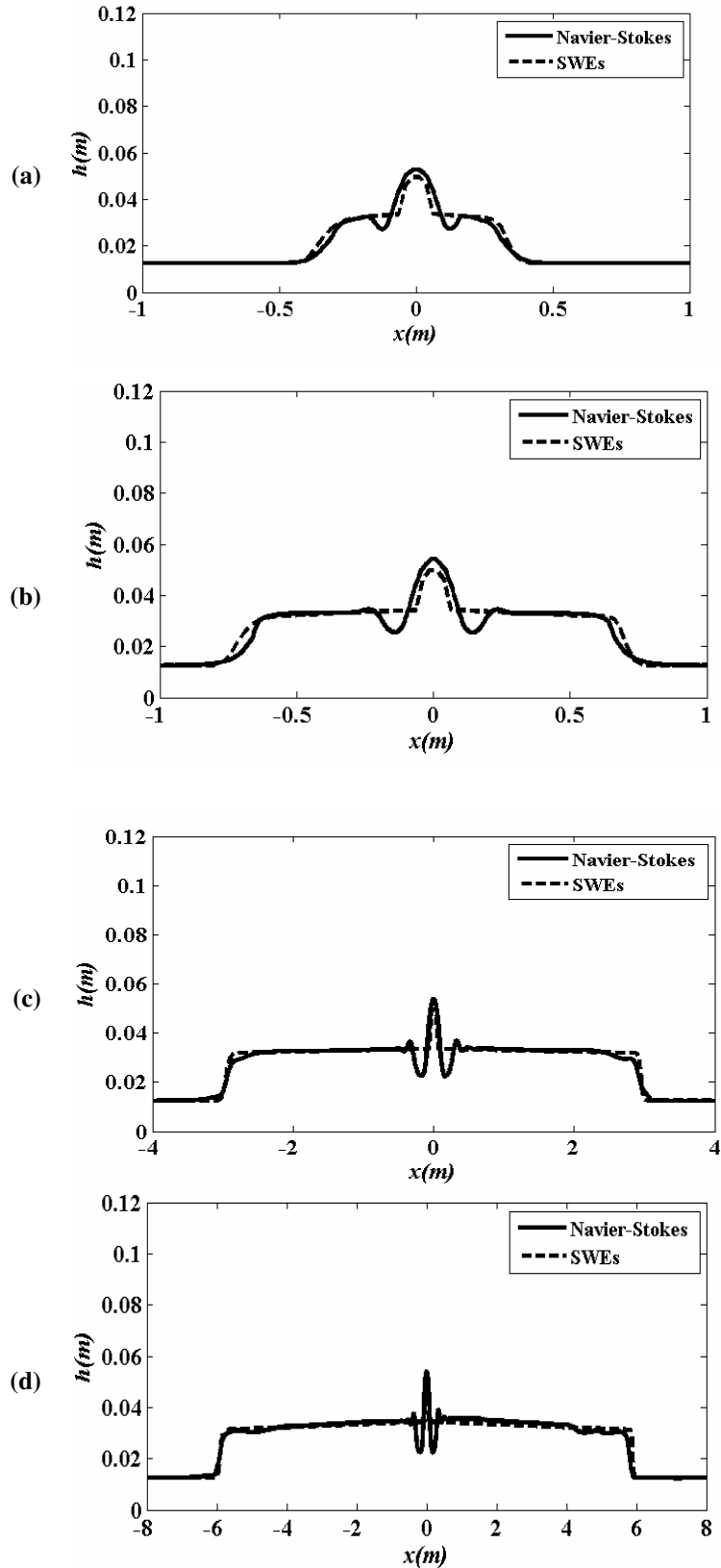
Figure 4.25. Efflux problem over wet states for different times and the *En* number equal to 0.3501 for time for time *t*=0.5s, *t*=1s, *t*=4s and *t*=8s (a-d).

(a) t=0.1s

(b) t=0.3s

(c) t=0.5s

(d) t=1s

(e) t=4s

(f) t=8s
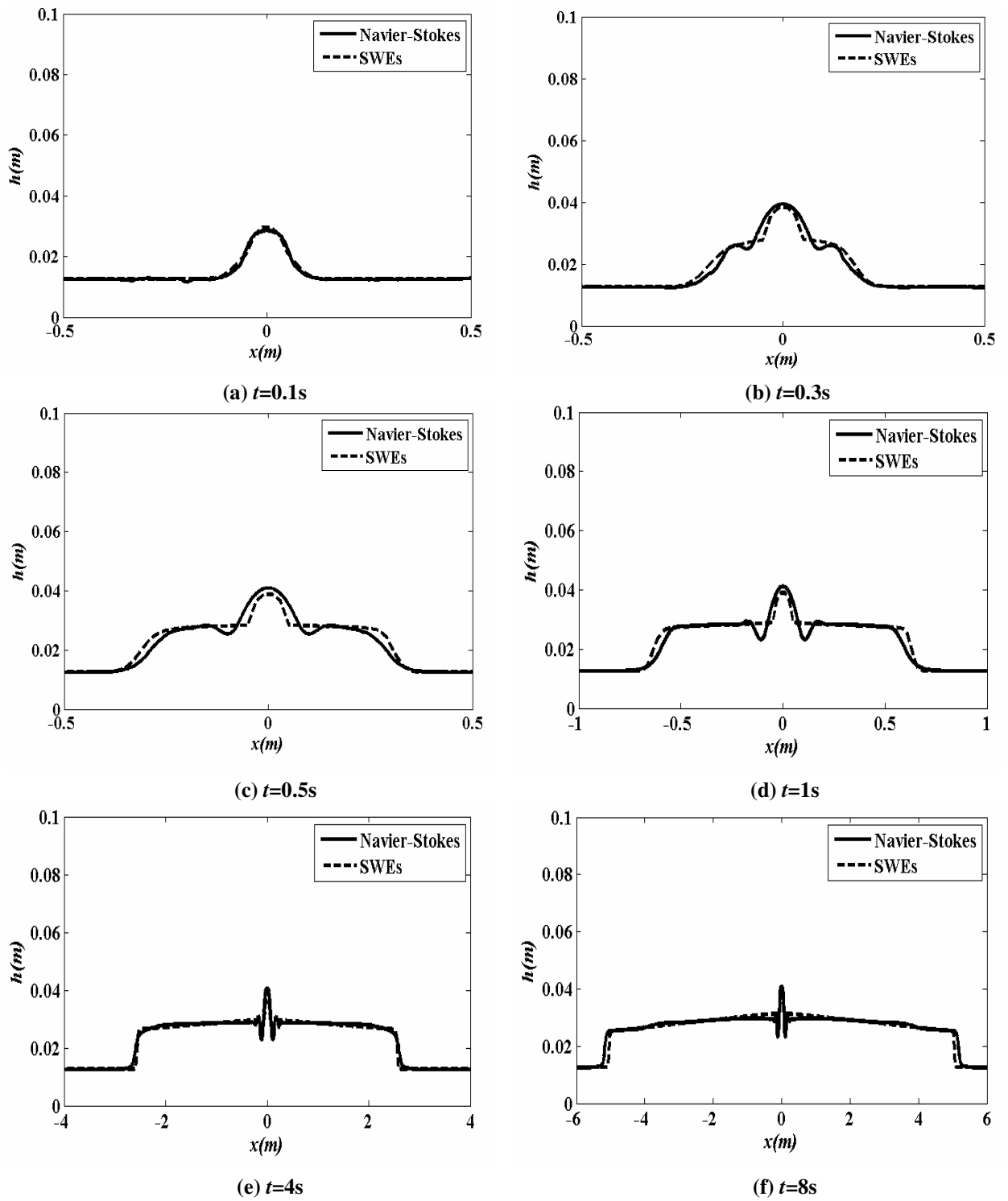
Figure 4.26. Efflux problem over wet states for different times and the *En* number equal to 0.201 for time for time t=0.1s, t=0.3s, t=0.5s, t=1s, t=4s and t=8s (a-f).

Table 4.5. The l_2 and l_∞ error and non-dimensional norms for the efflux problem over wet-state and *En=1.009.*

Time(s)	l_2	l_2 / d_{max}	l_∞	l_∞ / d_{max}
0.5	1.8×10^{-2}	1.3×10^{-1}	2.0×10^{-2}	1.5×10^{-1}
1	3.5×10^{-2}	2.5×10^{-1}	2.1×10^{-2}	1.5×10^{-1}
4	5.7×10^{-2}	3.9×10^{-1}	2.4×10^{-2}	1.7×10^{-1}
8	6.1×10^{-2}	4.1×10^{-1}	2.9×10^{-2}	1.9×10^{-1}

Table 4.6. The l_2 and l_∞ error and non-dimensional norms for the efflux problem over wet-state and *En= 0.501.*

Time(s)	l_2	l_2 / d_{max}	l_∞	l_∞ / d_{max}
0.5	1.0×10^{-3}	1.3×10^{-2}	1.4×10^{-2}	1.8×10^{-1}
1	1.3×10^{-3}	1.7×10^{-2}	1.5×10^{-2}	2.0×10^{-1}
4	2.2×10^{-3}	2.7×10^{-2}	1.7×10^{-2}	2.1×10^{-1}
8	2.6×10^{-3}	3.2×10^{-2}	1.6×10^{-2}	2.0×10^{-1}

Table 4.7. The l_2 and l_∞ error and non-dimensional norms for the efflux problem over wet-state and *En= 0.301.*

Time(s)	l_2	l_2 / d_{max}	l_∞	l_∞ / d_{max}
0.5	3.8×10^{-4}	7.3×10^{-3}	5.8×10^{-3}	1.1×10^{-1}
1	5.7×10^{-4}	1.0×10^{-2}	8.6×10^{-3}	1.5×10^{-1}
4	8.0×10^{-4}	1.4×10^{-2}	1.1×10^{-2}	2.0×10^{-1}
8	1.1×10^{-3}	1.9×10^{-2}	1.0×10^{-2}	1.9×10^{-1}

Table 4.8. The l_2 and l_∞ error and non-dimensional norms for the efflux problem over wet-state and *En= 0.201.*

Time(s)	l_2	l_2 / d_{max}	l_∞	l_∞ / d_{max}
0.1	1.3×10^{-4}	3.1×10^{-3}	1.7×10^{-3}	4.2×10^{-2}
0.3	3.8×10^{-4}	9.0×10^{-2}	3.6×10^{-3}	8.9×10^{-2}
0.5	5.2×10^{-4}	1.2×10^{-2}	4.5×10^{-3}	1.1×10^{-1}
1	6.9×10^{-4}	1.6×10^{-2}	6.8×10^{-3}	1.7×10^{-1}
4	8.8×10^{-4}	2.1×10^{-2}	7.0×10^{-3}	1.7×10^{-1}
8	1.6×10^{-3}	3.0×10^{-2}	8.4×10^{-3}	2.0×10^{-1}

Importantly, away from this region, the agreement between the SWEs and the Navier-Stokes solutions in Figure 4.27f, is very close for the location of the propagating flood wave. Hence, this demonstrates that the modified SWEs offer an accurate scheme for modelling the larger plan-scale effects of such a case without accurately representing the efflux process. Table 4.9 shows similar behaviour for the error norms for dam-break with the efflux problem. The maximum depth for this particular test case was chosen equal to 0.3m.

4.2.5 Dam-Break over a Dry Bed Driving Connected Influx and Efflux

A similar set up is used with both influx and efflux slot sizes of 6cm a distance of 1.75m apart, centred at x= 0.5m to 2.25m respectively. The connecting pipe is full of water. The initial conditions and the channel geometry are shown in Figure 4.28. The SWE scheme used 512 computational cells with a CFL number of 0.9. This set up was not possible with STAR-CD. After the dam-break the rarefaction wave approaches the entrance of the first slot (point A). The free-surface flow then passes over the first slot driving water through it and out of the downstream slot. The inflow discharge at point (A) for the pipe can be computed as follows,

$$Q_i = C_M \sqrt{2g\,(h_{av})}\Delta x,$$ (4.9)

Table 4.9. The l_2 and l_∞ error and non-dimensional norms for dam-break over dry bed with efflux.

Time(s)	l_2	l_2 / d_{max}	l_∞	l_∞ / d_{max}
0.4	9.6×10^{-3}	3.2×10^{-2}	3.3×10^{-2}	1.1×10^{-1}
0.6	6.9×10^{-3}	2.3×10^{-2}	6.3×10^{-2}	2.1×10^{-1}
0.8	7.1×10^{-3}	2.3×10^{-2}	4.9×10^{-2}	1.6×10^{-1}
1	6.9×10^{-3}	2.3×10^{-2}	4.3×10^{-2}	1.4×10^{-1}
1.2	6.1×10^{-3}	2×10^{-2}	1.8×10^{-2}	6×10^{-2}
1.4	8×10^{-3}	2.6×10^{-2}	1.9×10^{-2}	6.3×10^{-2}

(a) *t* = 0.4s

(b) *t* = 0.6s

(c) *t* = 0.8s

(d) *t* = 1.0s

(e) *t* = 1.2s

(f) *t* = 1.4s
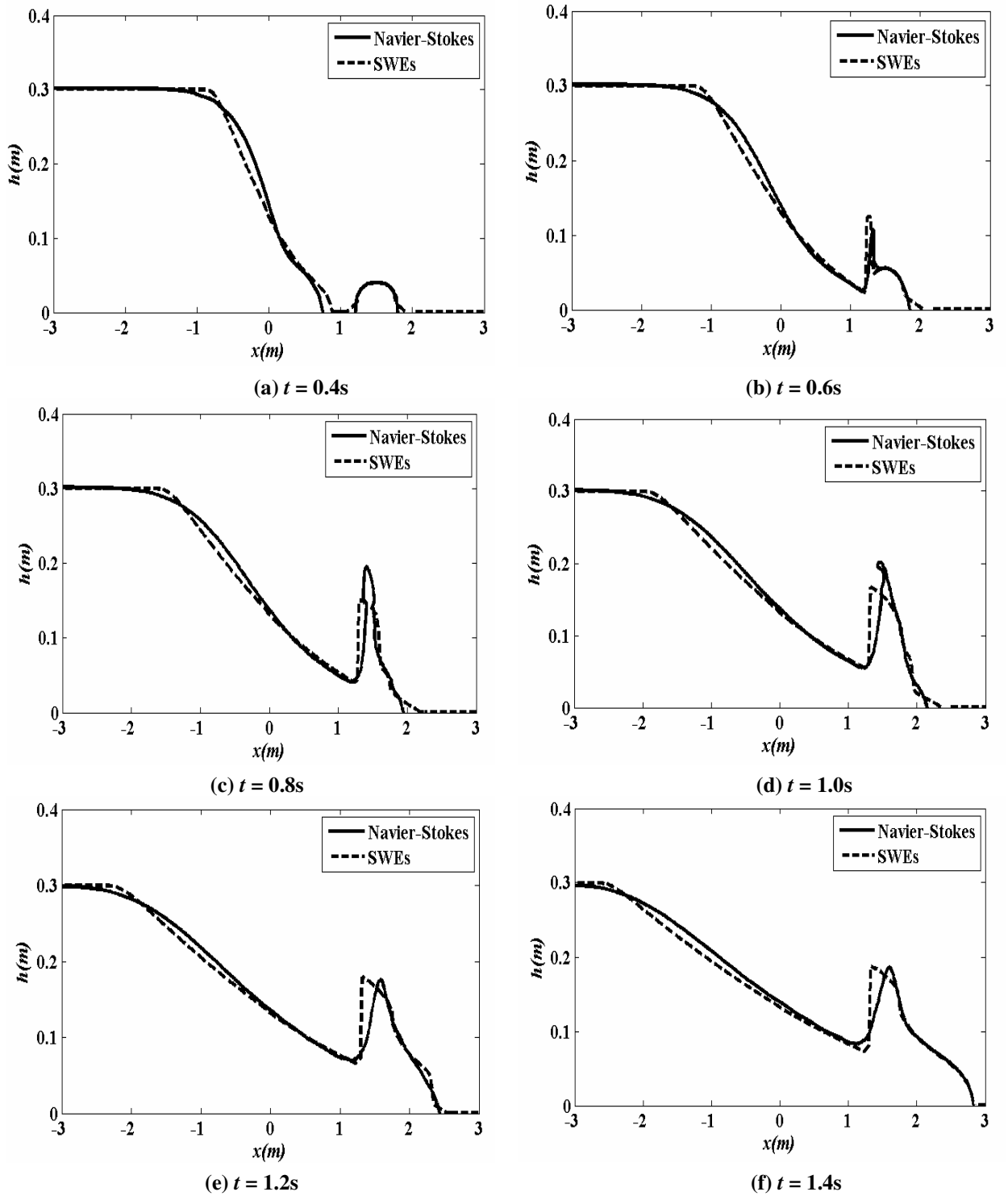
Figure 4.27. Dam -break problem over dry area with efflux discharge.
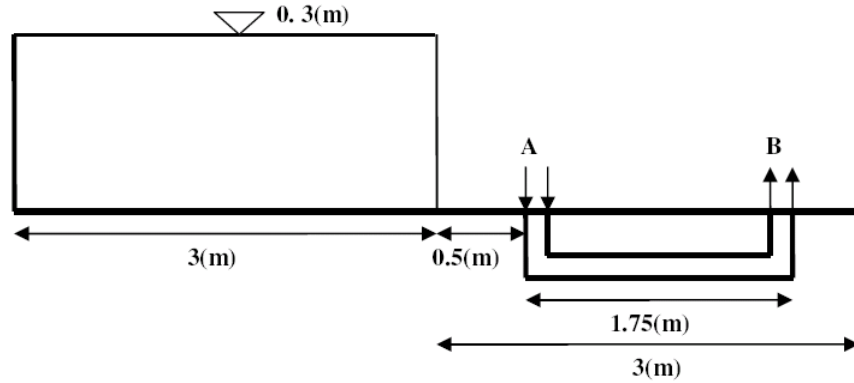
Figure 4.28. The initial problem for the dam-break problem over connected influx and efflux.

where Q_i denotes the intake flow imposed into the pipe as the dam flow crosses point A, $h_{av} = (h_i + h_{i-1})/2$ is the fluid depth entering the pipe obtained by averaging the depth of the neighbouring cells, Δx describes the slot length and C_M is the discharge coefficient for the pipe which was set to a typical value of 0.55. This discharge generates the efflux flow at point B onto the dry bed. Figure 4.29 shows the evolution of the surface profiles for different times. The rarefaction wave due to the dam-break propagates towards point A (Fig.4.29a), and when the free-surface has passed over the first slot, water is discharged at point B (Fig.4.29b). The dam bore then further collides with the exiting front and the fronts merge (Figs.4.29 c-e). This complex interaction is considered realistic since the elements have been tested against VOF Navier-Stokes solutions. The maximum slot efflux number does not exceed 0.5 and accurate predictions by the SWEs are thus expected.

4.3 Conclusions

In this Chapter we have presented the numerical results for one-dimensional SWEs with either the source terms in the momentum or continuity equations based on the wave propagation algorithm defined in the previous Chapter. In the first part of this Chapter, the reliability of scheme has been examined for the existence of strong rarefaction waves over dry-state with either homogenous (incipient cavitation) or inhomogeneous (vacuum with discontinuity) problems. Additionally the suitability of scheme has been validated for the steady-state cases with bathymetry deviations and demonstrated that the proposed Riemann solver can accurately balance the source term and flux gradient terms compared to other well-balanced approaches defined by other researchers. In part 2 the shallow water equations (SWEs) with local bed efflux and influx has been developed based on a modified wave
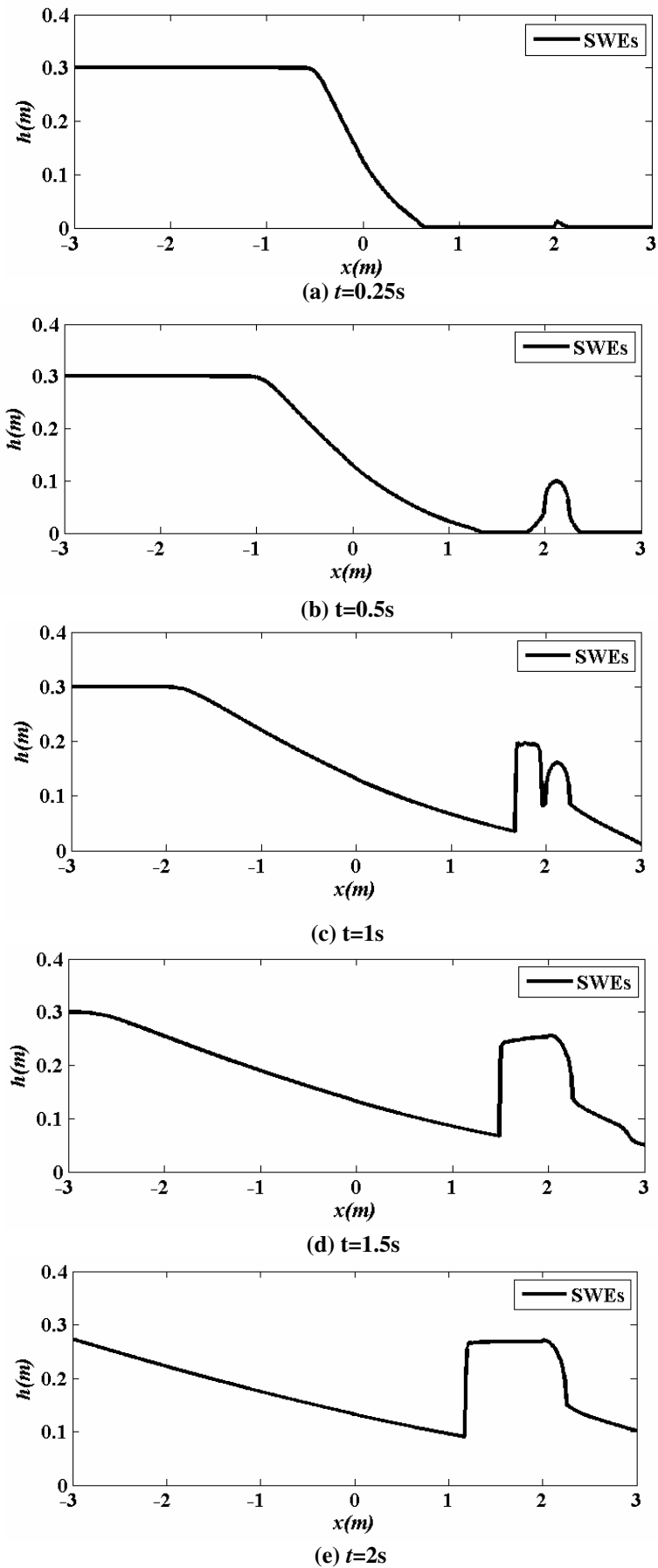
Figure 4.29. The dam-break problem over fully sewage pipe solved based on wave propagation (a-e).

propagation algorithm. The efflux/influx is included as a source term in the continuity equation. The modified wave propagation algorithm generates new Riemann speeds which improve the behaviour in dry states. Results in one-dimensional have been compared with two-dimensional vertical plane results from the VOF Navier-Stokes solver STAR-CD.

For dam-break flow, close agreement with the VOF method (with no slip wall boundaries) is obtained using an appropriate bed friction coefficient (estimated to be 0.015). For efflux only into an initially dry domain agreement with VOF results was close for all times with efflux numbers less than about 0.5. The bore front prediction at larger times was well predicted even with a higher efflux number of unity, although the flow local to the exit slot was quite different. For efflux into a wet domain the VOF method gave slightly smoother fronts than the SWE method as might be expected. For dam-break flow over a dry bed including efflux the agreement between VOF and SWE methods was good (for low efflux numbers). The SWE method was then demonstrated for the complex case of dam-break flow over a full pipe/tunnel with influx and efflux. In the next Chapter the two-dimensional mathematical extension for the SWEs and the f-wave approach is presented.

Chapter 5 : TWO-DIMENSIONAL EXTENSION FOR THE SHALLOW WATER EQUATIONS

In this Chapter we will introduce two-dimensional systems for the SWEs along with the extension of the theory and algorithms. First, we briefly describe the two-dimensional conservation laws, next the derivation of the conservation laws is explained from a fundamental integral form, then the general numerical methods for the multidimensional systems are concisely introduced and the remainder of this Chapter is devoted to the wave propagation algorithm for the two-dimensional shallow schemes which comprises the development of the new choice of wave speeds and treat with the source terms for two-dimensional shallow water problems. To obtaining second-order accuracy, the high-resolution terms and some transverse derivative terms will be introduced. The two-dimensional numerical results will be explained in Chapters 6 and 7.

5.1 Two-Dimensional Conservation Laws

The two-dimensional conservation laws are given as (neglecting the source terms)

$$U_t + F(U)_x + G(U)_y = 0, \tag{5.1}$$

where U denotes the vector of conserved unknowns, $F(U)$ and $G(U)$ show the flux functions in the x- and y-direction. For the linear hyperbolic systems the flux functions $F(U)$ and $G(U)$ can be described as AU_x and BU_y where A and B are specific matrices obtained based on conserved variables. So, for the quasi-linear systems equation (5.1) takes the form

$$U_t + AU_x + BU_y = 0. \tag{5.2}$$

5.2 Derivation of Conservation Laws

In this Section we describe the derivation of two-dimensional conservation laws from the fundamental integral form. Assume that the boundary of the spatial domain Ω is denoted by $\partial\Omega$ and contains only the conserved vector of U. This means that the vector of U varies only due the flux differencing across the boundary and therefore we have

$$\frac{d}{dt} \iint_\Omega U(x, y, t)dxdy = net\ flux, \tag{5.3}$$

The flux differencing across the boundary can be interpreted as a vector of flux function, say, $\vec{F}(U) = (F(U), G(U))$ which can be used with the divergence theorem to obtain the integral form of conservation law, that is

$$\frac{d}{dt} \iint_\Omega U(x, y, t)dxdy = -\iint_\Omega \vec{\nabla}.\vec{F}(U)dxdy, \tag{5.4}$$

where the divergence of the flux function can be calculated as

$$\vec{\nabla}.\vec{F}(U) = F(U)_x + G(U)_y, \tag{5.5}$$

and provided that the U is a smooth function Equation (5.4) becomes

$$\iint_\Omega (U_t + \vec{\nabla}.\vec{F}(U))dxdy = 0. \tag{5.6}$$

Equation (5.6) is the integral form of conservation law which leads to the differential form (5.1) for the smooth functions.

5.3 Two-Dimensional SWEs

The two-dimensional SWEs may be expressed as

$$U_t + F(U)_x + G(U)_y = S(U, x, y), \tag{5.7}$$

where now

$$U = \begin{bmatrix} h \\ hu \\ hv \end{bmatrix}, \quad F(U) = \begin{bmatrix} hu \\ hu^2 + \frac{1}{2}gh^2 \\ huv \end{bmatrix}, \quad G(U) = \begin{bmatrix} hv \\ huv \\ hv^2 + \frac{1}{2}gh^2 \end{bmatrix}. \tag{5.8}$$

where u, v are the horizontal depth-averaged velocities in the x- and y-directions respectively, and h is the water depth. The source term vector $S(U, x, y)$, including the

bathymetry gradient and friction terms in the momentum equations and the efflux/influx terms in the continuity equation, can be expressed as

$$S = \begin{bmatrix} \omega \\ -gh\dfrac{\partial z_b}{\partial x} - \dfrac{\tau_{fx}}{\rho} \\ -gh\dfrac{\partial z_b}{\partial y} - \dfrac{\tau_{fy}}{\rho} \end{bmatrix},$$

(5.9)

where ω is again efflux velocity and z_b is bed elevation. τ_{fx} and τ_{fy} denote the bed shear stress in orthogonal horizontal directions which can be defined by $\tau_{fx} = \frac{1}{2}C_f \rho u \sqrt{u^2 + v^2}$ and $\tau_{fy} = \frac{1}{2}C_f \rho v \sqrt{u^2 + v^2}$ respectively. C_f is the bed friction coefficient and ρ denotes water density. The Jacobian matrices of system (5.8) can be written as

$$F'(U) = A = \begin{bmatrix} 0 & 1 & 0 \\ -u^2 + c^2 & 2u & 0 \\ -uv & v & u \end{bmatrix}, \quad G'(U) = B = \begin{bmatrix} 0 & 0 & 1 \\ -uv & v & u \\ -v^2 + c^2 & 0 & 2v \end{bmatrix},$$

(5.10)

such that Equation (5.1) can be written as

$$U_t + F'(U)U_x + G'(U)U_y = S(U, x, y).$$

(5.11)

The eigenvalues of the Jacobian matrices A and B are

$$\lambda_1^F = u - c, \quad \lambda_2^F = u, \quad \lambda_3^F = u + c,$$

(5.12)

and

$$\lambda_1^G = v - c, \quad \lambda_2^G = v, \quad \lambda_3^G = v + c.$$

(5.13)

where $c = \sqrt{gh}$ is wave velocity. The corresponding eigenvectors for the eigenvalues (5.12) and (5.13) can be calculated as

$$\boldsymbol{r}_1^F = \begin{bmatrix} 1 \\ u-c \\ v \end{bmatrix}, \quad \boldsymbol{r}_2^F = \begin{bmatrix} 0 \\ 0 \\ 1 \end{bmatrix}, \quad \boldsymbol{r}_3^F = \begin{bmatrix} 1 \\ u+c \\ v \end{bmatrix}. \tag{5.14}$$

and

$$\boldsymbol{r}_1^G = \begin{bmatrix} 1 \\ u \\ v-c \end{bmatrix}, \quad \boldsymbol{r}_2^G = \begin{bmatrix} 0 \\ -1 \\ 0 \end{bmatrix}, \quad \boldsymbol{r}_3^G = \begin{bmatrix} 1 \\ u \\ v+c \end{bmatrix}. \tag{5.15}$$

5.4 Finite Volume Methods for Two-Dimensional Systems

In this Section we explain the finite volume methods for solving two-dimensional hyperbolic systems which is based on the numerical approximation of the cell average over the Cartesian grid. The numerical solution of the cell average $\tilde{\boldsymbol{U}}_{ij}$ can be approximated as

$$\tilde{\boldsymbol{U}}_{ij} = \frac{1}{\Delta x \Delta y} \iint_{C_{ij}} \boldsymbol{U}(x,y,t^n) dx dy , \tag{5.16}$$

where $C_{ij} = \left\{ [x_{i-1/2}, x_{i+1/2}] \times [y_{j-1/2}, y_{j+1/2}] \right\}$ is the rectangular grid cell and is shown in Figure 5.1. The cell average amount can be used in the differential or integral form of conservation laws formulae that is Equations (5.2) or (5.3). As described in Section 5.2 the conserved vector of unknowns can only vary because of the discrepancy between the incoming and outgoing fluxes through the particular computational cell edges. These flux differencing are used in the descretisation schemes for the hyperbolic systems. Here, we will begin with the linear form of conservation laws, and then obtain the second-order solution based on two-dimensional Lax-Wendroff scheme. Thereafter, the Lax-Wendroff method is explained based on the finite volume methods. The major part of this Section has been borrowed from [47] which are later used to derive a modified f-wave approach for the two-dimensional problems.
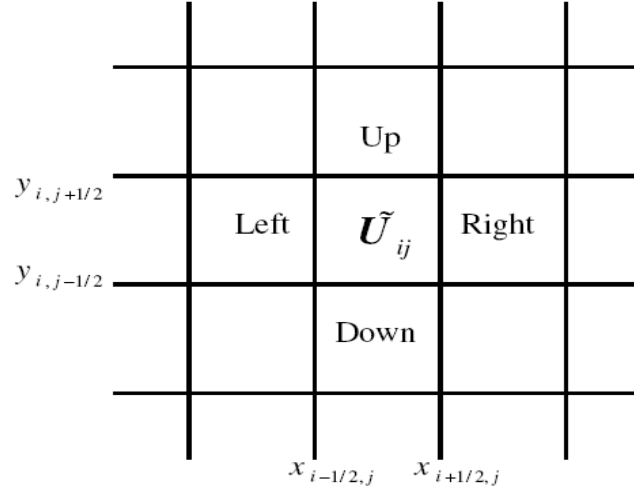
Figure 5.1. Two-dimensional finite volume cell for the wave propagation algorithm where $\tilde{U}_{ij}$ implies the cell average for the cell $\left[x_{i-1/2}, x_{i+1/2}\right] \times \left[y_{j-1/2}, y_{j+1/2}\right]$.

The high-order derivative for the linear conservation laws can be calculated via

$$U_{tt} = A^2 U_{xx} + ABU_{yx} + BAU_{xy} + B^2 U_{yy} . \tag{5.17}$$

If we use Taylor series expansion at point (x_i, y_i) for the next time step ($n+1$), then we have

$$U^{n+1} = U^n + \Delta t U_t + \frac{1}{2}\Delta t^2 U_{tt} + \cdots \tag{5.18}$$

If we replace the time derivatives in (5.18) by (5.2) and (5.17) then Equation (5.18) can be rewritten as

$$U^{n+1} = U^n - \Delta t \left(AU_x + BU_y\right) + \frac{1}{2}\Delta t^2 (A^2 U_{xx} + ABU_{yx} + BAU_{xy} + B^2 U_{yy}) + \cdots \tag{5.19}$$

The second-order spatial derivatives and cross-derivatives in Equation (5.17) can be approximated based on point-wise central finite difference scheme, say,

$$U_{xx} \approx \frac{1}{\Delta y^2}\left(\tilde{U}_{i,j-1}^n - 2\tilde{U}_{ij}^n + \tilde{U}_{i,j+1}^n\right), \quad U_{yy} \approx \frac{1}{\Delta x^2}\left(\tilde{U}_{i-1,j}^n - 2\tilde{U}_{ij}^n + \tilde{U}_{i+1,j}^n\right), \tag{5.20}$$

and

$$U_{xy} = U_{yx} \approx \frac{1}{\Delta x \Delta y} \left[\left(\tilde{U}_{i+1,j+1}^n - \tilde{U}_{i-1,j+1}^n \right) - \left(\tilde{U}_{i+1,j-1}^n - \tilde{U}_{i-1,j-1}^n \right) \right]. \tag{5.21}$$

Using Equation (5.19) and (5.20) into (5.18) leads to the Lax-Wendroff method

$$\tilde{U}_{ij}^{n+1} = \tilde{U}_{ij}^n - \frac{\Delta t}{2\Delta x} A \left(\tilde{U}_{i+1,j}^n - \tilde{U}_{i-1,j}^n \right) - \frac{\Delta t}{2\Delta y} B \left(\tilde{U}_{i,j+1}^n - \tilde{U}_{i,j-1}^n \right)$$

$$+ \frac{\Delta t^2}{2\Delta x^2} A^2 \left(\tilde{U}_{i+1,j}^n - 2\tilde{U}_{ij}^n + \tilde{U}_{i-1,j}^n \right) + \frac{\Delta t}{2\Delta y^2} B^2 \left(\tilde{U}_{i,j+1}^n - 2\tilde{U}_{ij}^n + \tilde{U}_{i,j-1}^n \right). \tag{5.22}$$

$$+ \frac{\Delta t^2}{8\Delta x \Delta y} (AB + BA) \left[\left(\tilde{U}_{i+1,j+1}^n - \tilde{U}_{i-1,j+1}^n \right) - \left(\tilde{U}_{i+1,j-1}^n - \tilde{U}_{i-1,j-1}^n \right) \right].$$

The two-dimensional Law-Wendroff method is inherently second-order accurate scheme. The only drawback of this method is that, for problems with the initial discontinuities, it produces non-physical oscillations around the sharp gradients. This can be effectively avoided by using flux limiters defined in the Chapter 2. To define a second-order wave propagation algorithm based on the finite volume approach, here, the major goal is to relate the proposed finite difference Lax-Wendroff method to its finite volume counterpart and fully explained in the remainder of this Chapter.

5.4.1 Fully Discrete Flux-Differencing Method

To derive a fully discrete two-dimensional method, the integral form of conservation laws should be applied around a computational cell C_{ij} affected by flux $F(U)$ along left and right edges and flux $G(U)$ along top and bottom of computational cell. Then, Equation (5.4) can be written as

$$\frac{\mathrm{d}}{\mathrm{dt}} \iint_{C_i} U(x,y,t) dx dy = \int_{y_{j-1/2}}^{y_{j+1/2}} F\left(U \left(U(x_{i+1/2}, y, t) \right) \right) dy - \int_{y_{j-1/2}}^{y_{j+1/2}} F\left(U \left(x_{i-1/2}, y, t \right) \right) dy +$$

$$\int_{x_{i-1/2}}^{x_{i+1/2}} G\left(U \left(x, y_{j+1/2}, t \right) \right) dx - \int_{x_{i-1/2}}^{x_{i+1/2}} G\left(U \left(x, y_{j-1/2}, t \right) \right) dx. \tag{5.23}$$

which leads to flux differencing method after integration and dividing over $\Delta x \, \Delta y$, that is

$$\tilde{U}_{ij}^{n+1} = \tilde{U}_{ij}^n - \frac{\Delta t}{\Delta x} \left[F_{i+1/2,j}^n - F_{i-1/2,j}^n \right] - \frac{\Delta t}{\Delta y} \left[G_{i,j+1/2}^n - G_{i,j-1/2}^n \right], \tag{5.24}$$

where fluxes are

$$F_{i-1/2,j}^{n} \approx \frac{1}{\Delta t \Delta y} \int_{t_n}^{t_{n+1}} \int_{y_{j-1/2}}^{y_{j+1/2}} F\left(U(x_{i-1/2}, y, t)\right) dy dt, \qquad (5.25a)$$

$$G_{i,j-1/2}^{n} \approx \frac{1}{\Delta t \Delta x} \int_{t_n}^{t_{n+1}} \int_{x_{i-1/2}}^{x_{i+1/2}} G\left(U(x, y_{j-1/2}, t)\right) dx dt. \qquad (5.25b)$$

The flux-differencing formula defined in Equation (5.24) can be simply related to the second-order Law-Wendroff method of the form (5.22). This can be done by choosing the fluxes $F_{i-1/2,j}$ and $G_{i,j-1/2}$ as

$$F_{i-1/2,j} = \frac{1}{2} A \left(\tilde{U}_{i-1,j} + \tilde{U}_{i,j}\right) - \frac{\Delta t}{2\Delta x} A^2 \left(\tilde{U}_{ij} - \tilde{U}_{i-1,j}\right)$$

$$- \frac{\Delta t}{8\Delta y} AB \left[\left(\tilde{U}_{i,j+1} - \tilde{U}_{ij}\right) + \left(\tilde{U}_{i-1,j+1} - \tilde{U}_{i-1,j}\right) + \left(\tilde{U}_{ij} - \tilde{U}_{i,j-1}\right) + \left(\tilde{U}_{i-1,j} - \tilde{U}_{i-1,j-1}\right)\right], \qquad (5.26a)$$

$$G_{i,j-1/2} = \frac{1}{2} B \left(\tilde{U}_{i,j-1} + \tilde{U}_{ij}\right) - \frac{\Delta t}{2\Delta y} B^2 \left(\tilde{U}_{ij} - \tilde{U}_{i,j-1}\right)$$

$$- \frac{\Delta t}{8\Delta x} BA \left[\left(\tilde{U}_{i+1,j} - \tilde{U}_{ij}\right) + \left(\tilde{U}_{i+1,j-1} - \tilde{U}_{i,j-1}\right) + \left(\tilde{U}_{ij} - \tilde{U}_{i-1,j}\right) + \left(\tilde{U}_{i,j-1} - \tilde{U}_{i-1,j-1}\right)\right]. \qquad (5.26b)$$

5.4.2 Godunov Method for the Wave Propagation Algorithm

For obtaining a general format of Godunov wave propagation algorithm from flux-differencing method mentioned in (5.24) one should relate the left- and right-going fluctuations in both directions to the flux vectors defined in (5.25a). The high-resolution version of the Godunov wave propagations for two-dimensional problems can be given as

$$\tilde{U}_{ij}^{n+1} = \tilde{U}_{ij} - \frac{\Delta t}{\Delta x}\left(A^+ \Delta \tilde{U}_{i-1/2,j} + A^- \Delta \tilde{U}_{i+1/2,j}\right) - \frac{\Delta t}{\Delta y}\left(B^+ \Delta \tilde{U}_{i,j-1/2} + B^- \Delta \tilde{U}_{i,j+1/2}\right)$$

$$- \frac{\Delta t}{\Delta x}\left(\tilde{F}_{i+1/2,j} - \tilde{F}_{i-1/2,j}\right) - \frac{\Delta t}{\Delta y}\left(\tilde{G}_{i,j+1/2} - \tilde{G}_{i,j-1/2}\right). \qquad (5.27)$$

$A^{\pm} \Delta U_{i\pm1/2,j}$ and $B^{\pm} \Delta U_{i,j\pm1/2}$ represent the left- and right-going fluctuations for the *x*- and *y*-directions. $\tilde{F}_{i\pm1/2,j}$ and $\tilde{G}_{i,j\pm1/2}$ are flux correction terms giving second-order accuracy [46, 47]. If $\tilde{F} = \tilde{G} = 0$, then the first-order Godunov method is obtained. Generally for two-dimensional conservation laws the fluctuations are defined as

$$A^+\Delta \tilde{U}_{i-1/2,j} = F(\tilde{U}_{ij}) - F(\tilde{U}_{i-1/2,j}), \tag{5.28a}$$

$$A^-\Delta \tilde{U}_{i-1/2,j} = F(\tilde{U}_{i-1/2,j}) - F(\tilde{U}_{i-1,j}), \tag{5.28b}$$

$$B^+\Delta \tilde{U}_{i,j-1/2} = G(\tilde{U}_{ij}) - G(\tilde{U}_{i,j-1/2}), \tag{5.28c}$$

$$B^-\Delta \tilde{U}_{i,j-1/2} = G(\tilde{U}_{i,j-1/2}) - G(\tilde{U}_{i,j-1}). \tag{5.28d}$$

where $F(\tilde{U}_{i-1/2,j})$ and $G(\tilde{U}_{i,j-1/2})$ show the flux term at cell interfaces in each direction. For calculating the left- and right-going fluctuations, each Riemann problem should be solved in the x- and y-directions by the dimensional-splitting method described in the next Section. This can be implemented by the f-wave method defined in [6] with the choice of Riemann speeds introduced in [60] for treating the dry bed propagation problem. The modified f-wave method for two-dimensional SWEs is described in the Section 5.6.

5.5 Dimensional-Splitting Method

The dimensional-splitting scheme leads to splitting the multidimensional Riemann problems into sequential one-dimensional problems. For example for non-linear two-dimensional system of the form $U_t + F(U)_x + G(U)_y = 0$, this can be done as

$$\begin{aligned} U_t + F(U)_x &= 0, \\ U_t + G(U)_y &= 0. \end{aligned} \tag{5.29}$$

In the x-sweeps, the one-dimensional Riemann problem is solved in the x-direction and the general one-dimensional Godunov method is used for calculating the intermediate state $\tilde{U}^*$, that is

$$\tilde{U}_{ij}^* = \tilde{U}_{ij} - \frac{\Delta t}{\Delta x}\left(A^+\Delta \tilde{U}_{i-1/2,j} + A^-\Delta \tilde{U}_{i+1/2,j}\right). \tag{5.30}$$

The calculated vector from x-sweep is used as a data for solving $U_t + G(U)_y = 0$ along y-direction which gives the vector of unknowns for the next time step,

$$\tilde{U}_{ij}^{n+1} = \tilde{U}_{ij}^* - \frac{\Delta t}{\Delta y}\left(B^+\Delta \tilde{U}_{i-1/2,j}^* + B^-\Delta \tilde{U}_{i+1/2,j}^*\right). \tag{5.31}$$

The correction flux terms can be added to the one-dimensional Riemann solver in each direction which is quite analogous to what was done for one-dimensional conservation laws. The only drawback for the method is the creation of splitting errors which are negligible compared to the descretisation error for the numerical schemes and for many cases the dimensional-splitting method gives very accurate results. For more detail see [46, 47]. Note that as mentioned above in this approach, it is not always possible to calculate the cross derivative terms existing in the Lax-Wendroff scheme. The dimensional-splitting method is later used with the f-wave approach for the inhomogeneous two-dimensional SWEs in the next Section. A very similar approach to the above method, is called *Strang-splitting* [45] which only contains a second intermediate state for the fluctuations in the *y*-direction and can be defined as follows

$$\tilde{U}_{ij}^{n+1} = \tilde{U}_{ij}^{n} - \frac{\Delta t}{2\Delta x}\left(A^{+}\Delta \tilde{U}_{i-1/2,j}^{**} + A^{-}\Delta \tilde{U}_{i+1/2,j}^{**}\right), \tag{5.32a}$$

$$\tilde{U}_{ij}^{**} = \tilde{U}_{ij}^{*} - \frac{\Delta t}{\Delta y}\left(B^{+}\Delta \tilde{U}_{i,j-1/2}^{*} + B^{-}\Delta \tilde{U}_{i,j+1/2}^{*}\right), \tag{5.31b}$$

$$\tilde{U}_{ij}^{n+1} = \tilde{U}_{ij}^{n} - \frac{\Delta t}{2\Delta x}\left(A^{+}\Delta \tilde{U}_{i-1/2,j}^{**} + A^{-}\Delta \tilde{U}_{i+1/2,j}^{**}\right). \tag{5.31c}$$

The only advantage of calculating the second intermediate state is for obtaining terms modelling $A(BU_{y})_{x}$ which are needed in the Taylor-series expansion. This causes little difference between this method and the dimensional-splitting scheme and in practice the proposed method often gives worse results than the original splitting method [47].

5.6 The F-wave Approach for Two-Dimensional SWEs

Here, we will explain the modified f-wave approach defined in Chapter 3 for two-dimensional SWEs. As mentioned above the wave propagation algorithm is computed by splitting the system into two one-dimensional problems. For example, in the *x*-direction the inhomogeneous equation $U_{t} + F(U)_{x} = S_{1}$ is solved by the f-wave approach to determine the fluctuations $A^{\pm}\Delta U_{i\pm1/2,j}$. The only additional term in two dimensions is the contact discontinuity which creates another flux wave compared to the one-dimensional problem. The f-wave formula for the two-dimensional SWEs can be expressed as [6, 47]

$$F(U_{i}) - F(U_{i-1}) - S_{1}\Delta x = \sum_{k=1}^{M_{w}}\xi_{k,i-1/2}, \tag{5.33}$$

where $\xi_{k,i-1/2}$ shows the flux wave obtained by multiplication of the constant coefficients $\beta_{k,i-1/2}$ into the eigenvector of the form (5.14), say, $\beta_{k,i-1/2}r^{F}_{k,i-1/2}$ and M_{w} denotes the number of waves. For two-dimensional efflux problems the efflux discharge ω should be split into $(\alpha_{x}\omega, \alpha_{y}\omega)$ where $\alpha_{x}+\alpha_{y}=1$. Here and for the efflux problems $(\omega,0)$, $\left(\dfrac{\omega}{2},\dfrac{\omega}{2}\right)$ and $(0,\omega)$ have been tested and give the same results for test cases as would be expected. The $\left(\dfrac{\omega}{2},\dfrac{\omega}{2}\right)$ split has been applied generally. The flux terms and the source terms for the x-direction take the form

$$\mathbf{F(U)}=\left(hu, hu^{2}+1/2gh^{2}, huv\right)^{T} \text{ and } \mathbf{S}_{1}=\left(\frac{\omega_{i-1/2,j}}{2}, -gh\frac{\partial z_{b}}{\partial x}-\frac{\tau_{fx}}{\rho}, 0\right)^{T}. \tag{5.34}$$

If we replace the flux wave $\xi_{k,i-1/2}$ by the multiplication of the eigenvectors by constant coefficients $\beta_{k,i-1/2}$, then Equation (5.33) becomes

$$\begin{bmatrix} h_{i}u_{i}-h_{i-1}u_{i-1}-\dfrac{\Delta x}{2}\omega_{i-1/2} \\[2mm] (h_{i}u_{i}^{2}+1/2gh_{i}^{2})-(h_{i-1}u_{i-1}^{2}+1/2gh_{i-1}^{2})+\Delta x\left(-gh\dfrac{\partial z_{b}}{\partial x}-\dfrac{\tau_{fx}}{\rho}\right) \\[2mm] h_{i}u_{i}v_{i}-h_{i-1}u_{i-1}v_{i-1} \end{bmatrix} =$$

$$\beta_{1,i-1/2}\begin{bmatrix}1\\ s_{1,i-1.2}\\ ve_{i-1/2}\end{bmatrix}+\beta_{2,i-1/2}\begin{bmatrix}0\\ 0\\ 1\end{bmatrix}+\beta_{3,i-1/2}\begin{bmatrix}1\\ s_{3,i-1/2}\\ ve_{i-1/2}\end{bmatrix}, \tag{5.35}$$

where $s_{1,i-1/2}$ and $s_{3,i-1/2}$ are the first and third wave speeds calculated based on s_{ARWS1} and s_{ARWS2} formulae proposed in [60]. $ve_{i-1/2}$, is a wave speed in the y-direction which can be obtained from

$$ve_{i-1/2}=\frac{ve_{i-1}+ve_{i}}{2}, \tag{5.36a}$$

114

$$ve_{i-1} = \min\left(v_{Roe}, v_{i-1}\right), \quad ve_i = \max\left(v_{Roe}, v_i\right). \tag{5.36b}$$

and v_{Roe} is calculated based on a Roe speed, that is

$$v_{Roe} = \frac{\sqrt{h_{i-1}}v_{i-1} + \sqrt{h_i}v_i}{\sqrt{h_{i-1}} + \sqrt{h_i}}. \tag{5.37}$$

Then, the coefficients $\beta_{k,i-1/2}$ can be calculated as

$$\beta_{1,i-1/2} = \frac{\Gamma_2 - s_{3,i-1/2}}{s_{1,i-1/2} - s_{3,i-1/2}}, \quad \beta_{2,i-1/2} = \Gamma_3 - ve_{i-1/2}\Gamma_1, \quad \beta_{3,i-1/2} = \frac{s_1\Gamma_1 - \Gamma_2}{s_{1,i-1/2} - s_{3,i-1/2}}, \tag{5.38}$$

where

$$\Gamma_1 = h_i u_i - h_{i-1}u_{i-1} - \frac{\Delta x}{2}\omega_{i-1/2}, \tag{5.39a}$$

$$\Gamma_2 = (h_i u_i^2 + 1/2 gh_i^2) - (h_{i-1}u_{i-1}^2 + 1/2 gh_{i-1}^2) + \Delta x\left(-gh\frac{\partial z_b}{\partial x} - \frac{\tau_{fx}}{\rho}\right), \tag{5.39b}$$

$$\Gamma_3 = h_i u_i v_i - h_{i-1}u_{i-1}v_{i-1}. \tag{5.39c}$$

The $s_{1,i-1/2}$ and $s_{3,i-1/2}$ speeds, used for the f-wave approach here, employ the combination of the exact and approximate Riemann speeds to overcome the difficulties for the original f-wave method regarding propagation over dry or nearly dry beds where the fluid depth is close to zero (see [60] for a discussion). By calculating the coefficients for the f-wave approach, the left- and right-going fluctuations $A^{\pm}\Delta U_{i\pm1/2,j}$, can be computed via $A^-\Delta U_{i-1/2} = \sum_{k:s_{i-1/2}<0}\xi_{k,i-1/2}$ and $A^+\Delta U_{i-1/2} = \sum_{k:s_{i-1/2}>0}\xi_{k,i-1/2}$ respectively which are later used in Equation (5.27) to compute the updated version for the Godunov method. In a similar way $B^{\pm}\Delta U_{i,j\pm1/2}$ can be evaluated by solving $U_t + G(U)_y = S_2$ in the y–direction where the flux term and source term can be defined as

$$\boldsymbol{G(U)} = \left(hv\,, huv\,, hv^2 + 1/2\,gh^2 \right)^T \quad \text{and} \quad \boldsymbol{S}_2 = \left(\frac{\omega_{i-1/2,j}}{2}, 0, -gh\frac{\partial z_b}{\partial y} - \frac{\tau_{fy}}{\rho} \right)^T. \tag{5.40}$$

As mentioned earlier the cross-derivative terms for second-order accuracy can be added to the correction fluxes $\tilde{F}_{i\pm1/2,j}$ and $\tilde{G}_{i,j\pm1/2}$ in each direction by splitting the left- and right-going fluctuations $\boldsymbol{A}^{\pm}\Delta U_{i\pm1/2,j}$ into additional left- and right-going transverse terms. This requires the solution of another Riemann problem for the orthogonal direction. This has been described in [47] for the multidimensional conservation laws and here we will briefly explain the method for the modified f-wave approach. For two-dimensional SWEs based on the wave propagation algorithm the right-going fluctuations should be decomposed into the eigenvector of the matrix $\boldsymbol{B}$, that is

$$\boldsymbol{A}^{+}\Delta U_{k,i\text{-}1/2} = \sum_{k=1}^{M_w} \alpha_{k,i-1/2}\boldsymbol{r}^{G}_{k,i-1/2}. \tag{5.41}$$

which can be rewritten as

$$\begin{bmatrix} A^{+}\Delta U_{1,i-1/2} \\ A^{+}\Delta U_{2,i-1/2} \\ A^{+}\Delta U_{3,i-1/2} \end{bmatrix} = \alpha_{1,i-1/2}\begin{bmatrix} 1 \\ ue_{i-1/2} \\ s_{1,i-1/2} \end{bmatrix} + \alpha_{2,i-1/2}\begin{bmatrix} 0 \\ -1 \\ 0 \end{bmatrix} + \alpha_{3,i-1/2}\begin{bmatrix} 1 \\ ue_{i-1/2} \\ s_{3,i-1/2} \end{bmatrix}, \tag{5.42}$$

$s_{1,i-1/2}$ and $s_{3,i-1/2}$ should be computed for the $v_{i-1/2}$ (depth-averaged velocity in the y-direction) and $ue_{i-1/2}$ is equal to second eigenvalue for eigenvectors $\boldsymbol{r}^{F}_{k,i-1/2}$. The relevant coefficients, $\alpha_{k,i-1/2}$ can be computed as follows

$$\alpha_{1,i-1/2} = \frac{A^{+}\Delta U_{3,i\text{-}1/2} - s_{3,i-1/2}A^{+}\Delta U_{1,i\text{-}1/2}}{s_{1,i-1/2} - s_{3,i-1/2}}, \tag{5.43a}$$

$$\alpha_{2,i-1/2} = ue_{i-1/2}A^{+}\Delta U_{1,i\text{-}1/2} - A^{+}\Delta U_{2,i\text{-}1/2}, \tag{5.43b}$$

$$\alpha_{3,i-1/2} = \frac{A^{+}\Delta U_{1,i\text{-}1/2}s_{1,i-1/2} - A^{+}\Delta U_{3,i\text{-}1/2}}{s_{1,i-1/2} - s_{3,i-1/2}}. \tag{5.43c}$$

Then, the transverse fluctuation are defined

$$\boldsymbol{B}^{\pm}\boldsymbol{A}^{+}\Delta\boldsymbol{U}_{k,i-1/2} = \sum_{k=1}^{M_w}\left(\lambda_k^G\right)^{\pm}\alpha_{k,i-1/2}\boldsymbol{r}_{k,i-1/2}^{G} \tag{5.44}$$

where $\boldsymbol{B}^{+}\boldsymbol{A}^{+}\Delta\boldsymbol{U}_{i-1/2,j}$ and $\boldsymbol{B}^{-}\boldsymbol{A}^{+}\Delta\boldsymbol{U}_{i-1/2,j}$ are the up- and down-going transverse derivatives [47] for the right-going fluctuation. The up-going and down-going transverse derivative for the left-going fluctuation is obtained in a similar way. These transverse fluctuations are then used to update the correction fluxes above and below cell C_{ij} [47]

$$\tilde{\boldsymbol{G}}_{i,j+1/2}^{new} = \tilde{\boldsymbol{G}}_{i,j+1/2} - \frac{\Delta t}{2\Delta x}\boldsymbol{B}^{+}\boldsymbol{A}^{+}\Delta\boldsymbol{U}_{i-1/2,j}, \tag{5.45a}$$

$$\tilde{\boldsymbol{G}}_{i,j-1/2}^{new} = \tilde{\boldsymbol{G}}_{i,j-1/2} - \frac{\Delta t}{2\Delta x}\boldsymbol{B}^{-}\boldsymbol{A}^{+}\Delta\boldsymbol{U}_{i-1/2,j}. \tag{5.45b}$$

and the correction flux updating for the left-going fluctuation should be applied above and below cell $C_{i-1,j}$ and is defined as

$$\tilde{\boldsymbol{G}}_{i-1,j+1/2}^{new} = \tilde{\boldsymbol{G}}_{i-1,j+1/2} - \frac{\Delta t}{2\Delta x}\boldsymbol{B}^{+}\boldsymbol{A}^{-}\Delta\boldsymbol{U}_{i-1/2,j}, \tag{5.46a}$$

$$\tilde{\boldsymbol{G}}_{i-1,j-1/2}^{new} = \tilde{\boldsymbol{G}}_{i-1,j-1/2} - \frac{\Delta t}{2\Delta x}\boldsymbol{B}^{-}\boldsymbol{A}^{-}\Delta\boldsymbol{U}_{i-1/2,j}. \tag{5.46b}$$

The Equations (5.40-5.45) should be repeated for the Riemann problem in the y-directions to compute the effect of cross-derivatives terms for the correction flux $\tilde{\boldsymbol{F}}_{i\pm1/2,j}$.

5.7 CFL Conditions

The stability condition for the two-dimensional SWEs is determined by the Courant-Friedrichs–Lewy criterion (CFL) for time step Δt. For the two-dimensional wave propagation algorithm based on dimensional-splitting method this requires for each one-dimensional Riemann problem

$$\Delta t = \min(\Delta t_x, \Delta t_y), \tag{5.47}$$

where $\qquad \Delta t_x = \dfrac{Cr\Delta x}{\max(|s_1|,|s_3|)}$ and $\Delta t_y = \dfrac{Cr\Delta y}{\max(|s_1|,|s_3|)}$,

where Cr is the Courant or CFL number and $0 < Cr \leq 0$. Here and in this thesis for most two-dimensional test cases we generally use $Cr=0.2$.

5.8 Conclusions

The numerical approach explained in this Chapter employs the modified f-wave method for the two-dimensional SWEs with source terms in the continuity and momentum equations. To solve the two-dimensional SWEs each one-dimensional Riemann problem is solved in the x- and y-directions separately. The cross-derivative terms for second-order accuracy are incorporated by solving another Riemann problem in the orthogonal direction. The main advantage of the proposed scheme is that the source terms can be simply treated by flux-differencing which maintains precisely mass-conservation for stationary and steady-state flow. Additionally the method takes advantage of the new choice of wave speeds which enables the scheme to model wave propagation over a dry bed with multiple bore interactions. The only difficulty for the scheme is defining the magnitude of epsilon (ε) which determines the depth below which the bed is nearly-dry [60] and this needs to be solved based on the exact Riemann speeds. However, for most of numerical test cases within this paper the range of epsilon between 0.003-0.007m provides depth-positive results for the wave propagation algorithm including the second-order accurate terms. The proposed technique will be validated in the Chapter 6 for the standard shallow water benchmarks and the shallow water problem with the efflux terms.

Chapter 6 : NUMERICAL RESULTS FOR TWO-DIMENSIONAL SHALLOW WATER EQUATIONS

In this Chapter we will present the numerical results for shallow water benchmarks to validate the wave propagation algorithm based on the new choice of wave speed for two-dimensional problems. This Chapter is again presented in two parts. In the first part the standard shallow water benchmark are examined based on the modified f-wave approach. The results with very fine grids are also considered to investigate the convergence property of the scheme. The second part includes the results with the efflux/influx terms in the continuity equations. To examine the validity of the efflux velocities for two-dimensional problems comparisons are again made by STAR-CD with different efflux number.

6.1 Part I: The Standard Two-Dimensional Shallow Water Benchmarks

In this Section the standard shallow water benchmarks introduced in the literature are validated based on the modified f-wave approach and dimensional-splitting method explained in the previous Chapter. In this part, first, the circular dam-break problem over the wet and dry states is presented. Then, the rectangular dam-break behind the wall is examined with the wave propagation algorithm. The final test case in this Section concerns the dam propagation over three-humps which examine the suitability of the proposed scheme to deal with complex bed topography and friction terms.

6.1.1 Radial Dam-Break over Wet-State.

This test case was suggested in [47, 85] which shows the effect of circular water column propagating over a wet-state. For the idealised case considered here the water depth is initially chosen equal to $h = 2\text{m}$ inside a circular column of water centred at the origin and $h = 1\text{m}$ outside. The diameter of the water column was selected equal to 0.5. We have exactly used the initial condition defined in [47]. Figure 6.1a, demonstrates the initial condition for the circular dam-break. Figure 6.2 illustrates the numerical results including 3-D water surface and contour plots at time steps t=0.25s, 0.5s, 1s and 1.5s. After the dam's failure, the shock waves move radially outwards while the rarefaction waves travel inside toward to centre of computational domain. This is quite similar to one-dimensional dam-break problem and the only difference is due to the radial propagation.
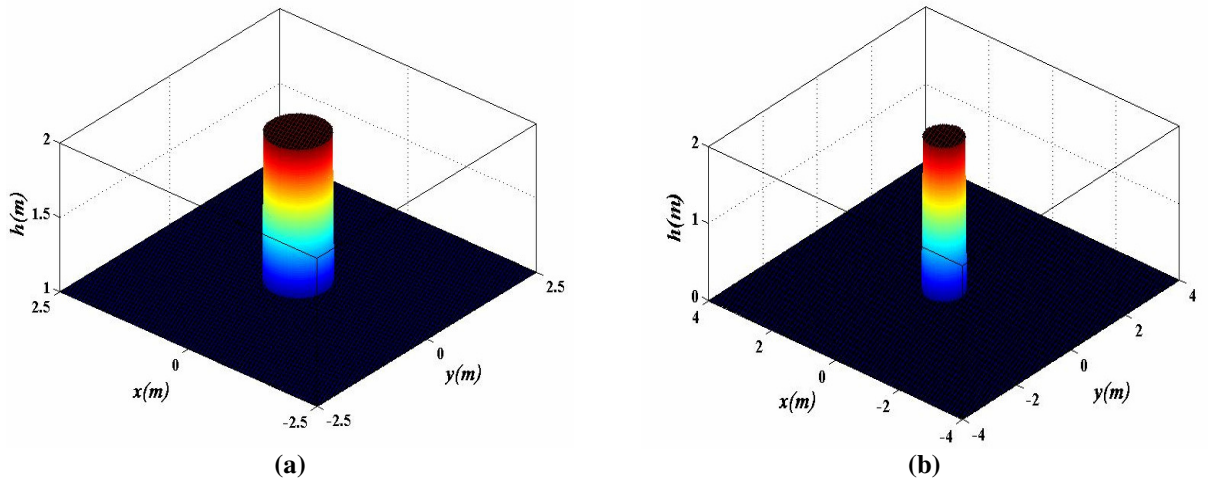
Figure 6.1. The initial condition for the radial dam-break problem. (a): Wet state, (b): Dry-state.

At time t=0.5s the rarefaction waves approximately reach to the centre of domain and start to reflect outwards again. By time t=1s the reflected rarefaction waves are accelerated and cause the free-surface reaches nearly to bed. Additionally, at this time the secondary shock waves start to propagate vertically through the centre. The creation of secondary shock wave is probably due to over expansion of the reflected rarefaction waves [85]. At time t=2s the secondary circular shock wave is moving radially toward domain boundaries. The number of grid cells and the Courant number (Cr) were selected equal to 128×128 and 0.2 respectively. The obtained numerical results are in a close agreement with [47, 85]. Figure 6.3 illustrates the results for the circular dam-break problem performed based on 1024×1024 grid cells.

6.1.2 Radial Dam-Break over Dry-State

The aim of this test case is to verify the reliability of the method to deal with shallow water problems over dry areas. Here, again a circular dam was considered at the centre of the rectangular domain $[-4\text{m}, 4\text{m}] \times [-4\text{m}, 4\text{m}]$ with an initial water depth h=2m inside and a dry depth for the rest of domain. The diameter for the circular thin dam again was chosen equal to 5cm. The initial condition for this problem is depicted in Figure 6.1b. As the wall of circular dam is removed only the rarefaction waves radially travel outward and no shock wave is created over dry-state. Figure 6.4 presents three-dimensional (3-D) free-surface views and contour plots at time t=0.25s, t=0.5s, t=1s and t=1.5s with the modified f-wave approach and dimensional-splitting method. As can be seen here, the results indicate that

t=0.25s

t=0.5s

t=1s

t=1.5s
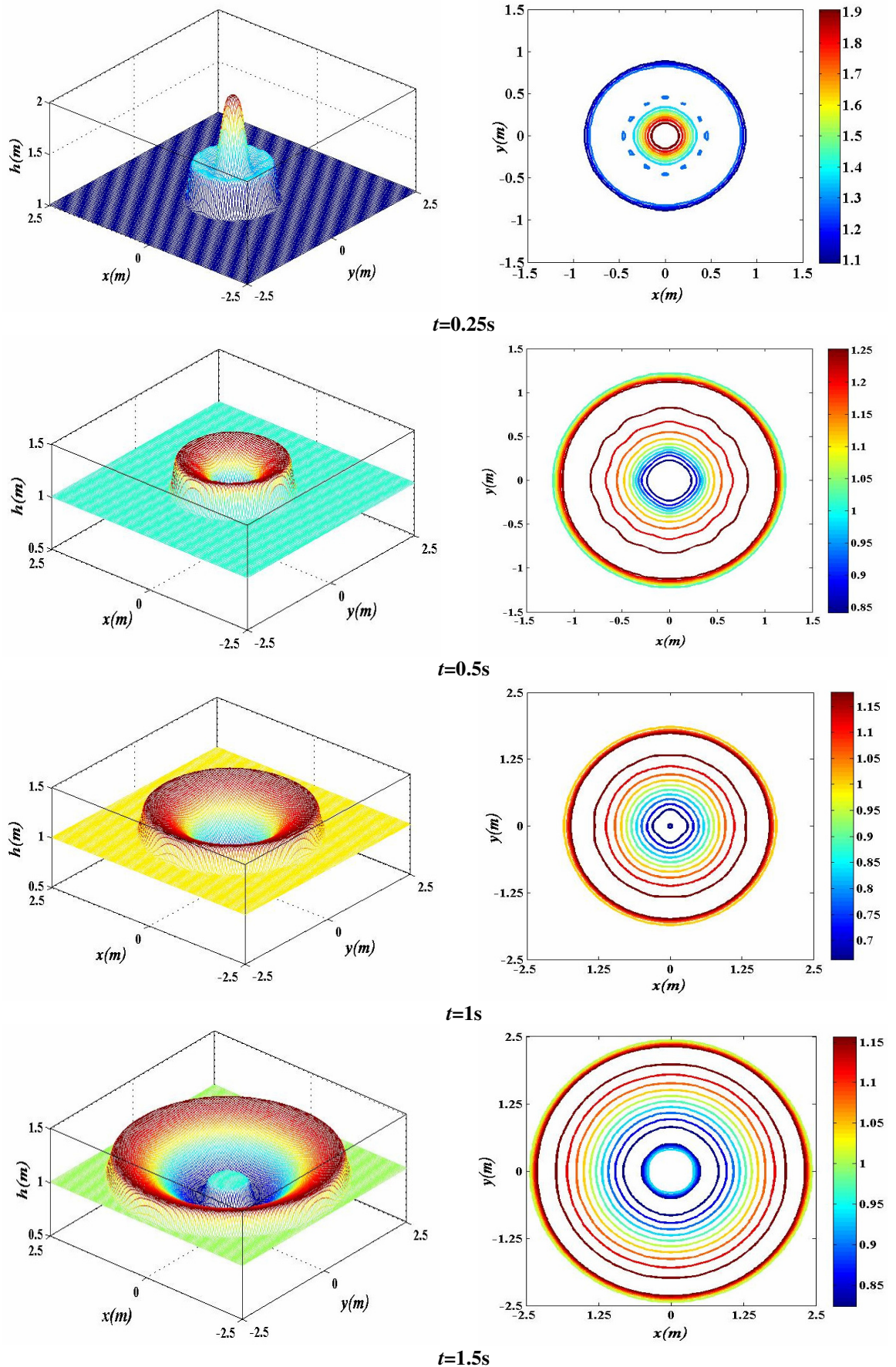
Figure 6.2. Radial dam-break over wet state (water depth contours and 3-D water surface plots) with a f-wave approach and for 128×128 grid cells.

t=0.25s

t=0.5s

t=1s

t=1.5
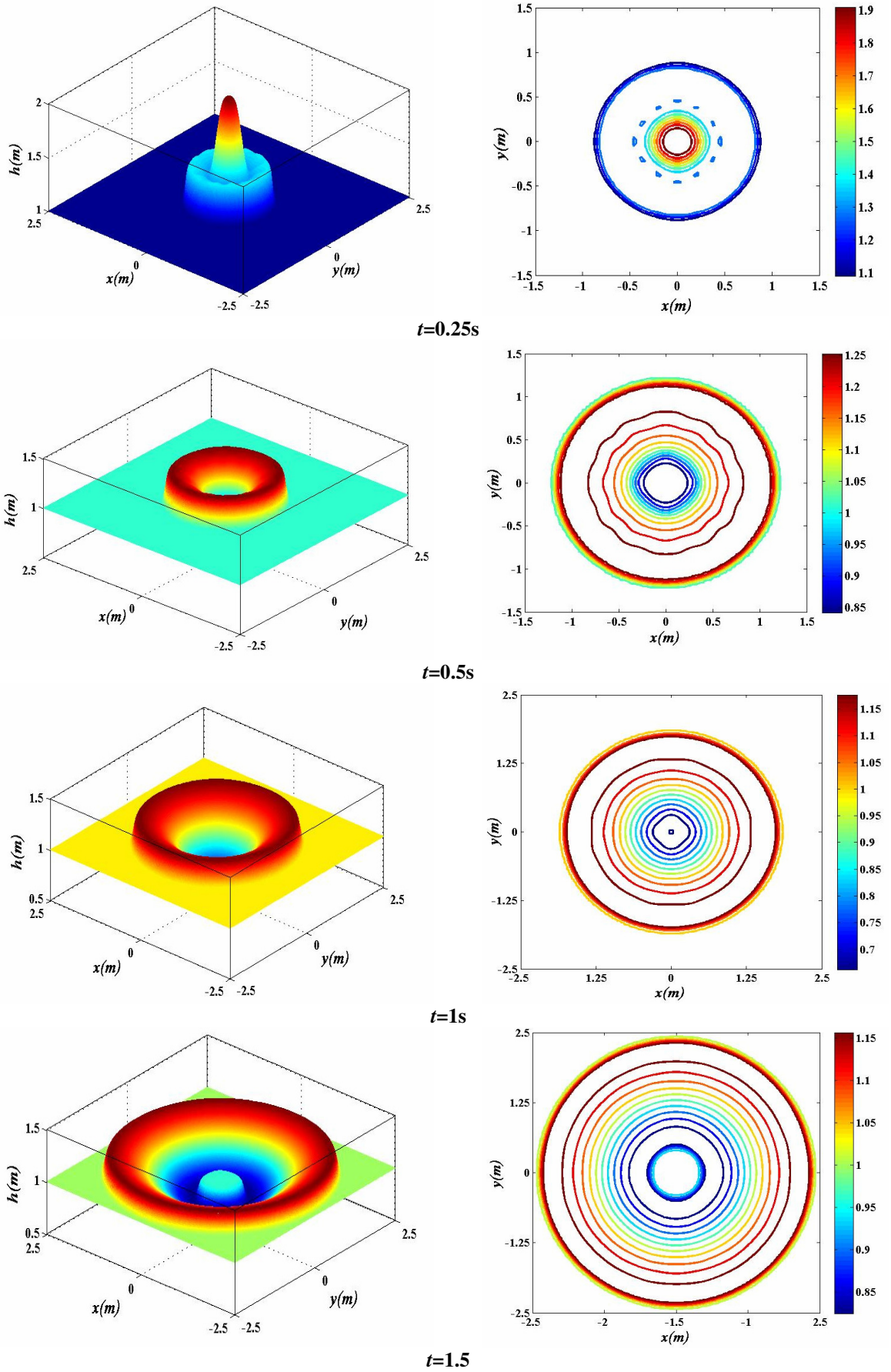
Figure 6.3. Radial dam-break over wet state (water depth contours and 3-D water surface plot) with a modified f-wave approach and for 1024×1024 grid cells.

122
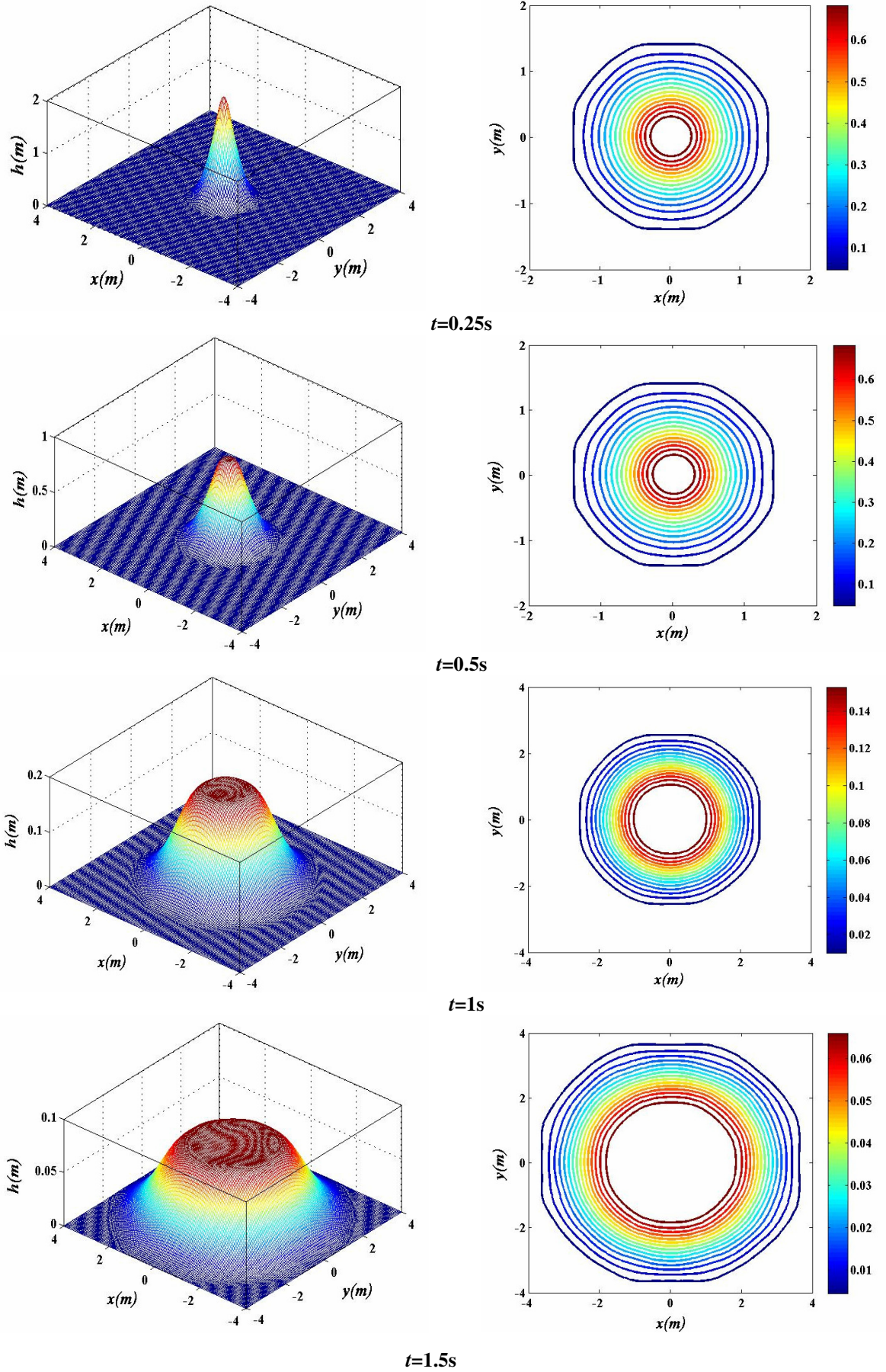
Figure 6.4. Radial dam-break over dry-state (water depth contours and 3-D water surface plots) with a modified f-wave approach and for 128×128 grid cells.

123

t=0.25s

t=0.5s

t=1s

t=1.5s
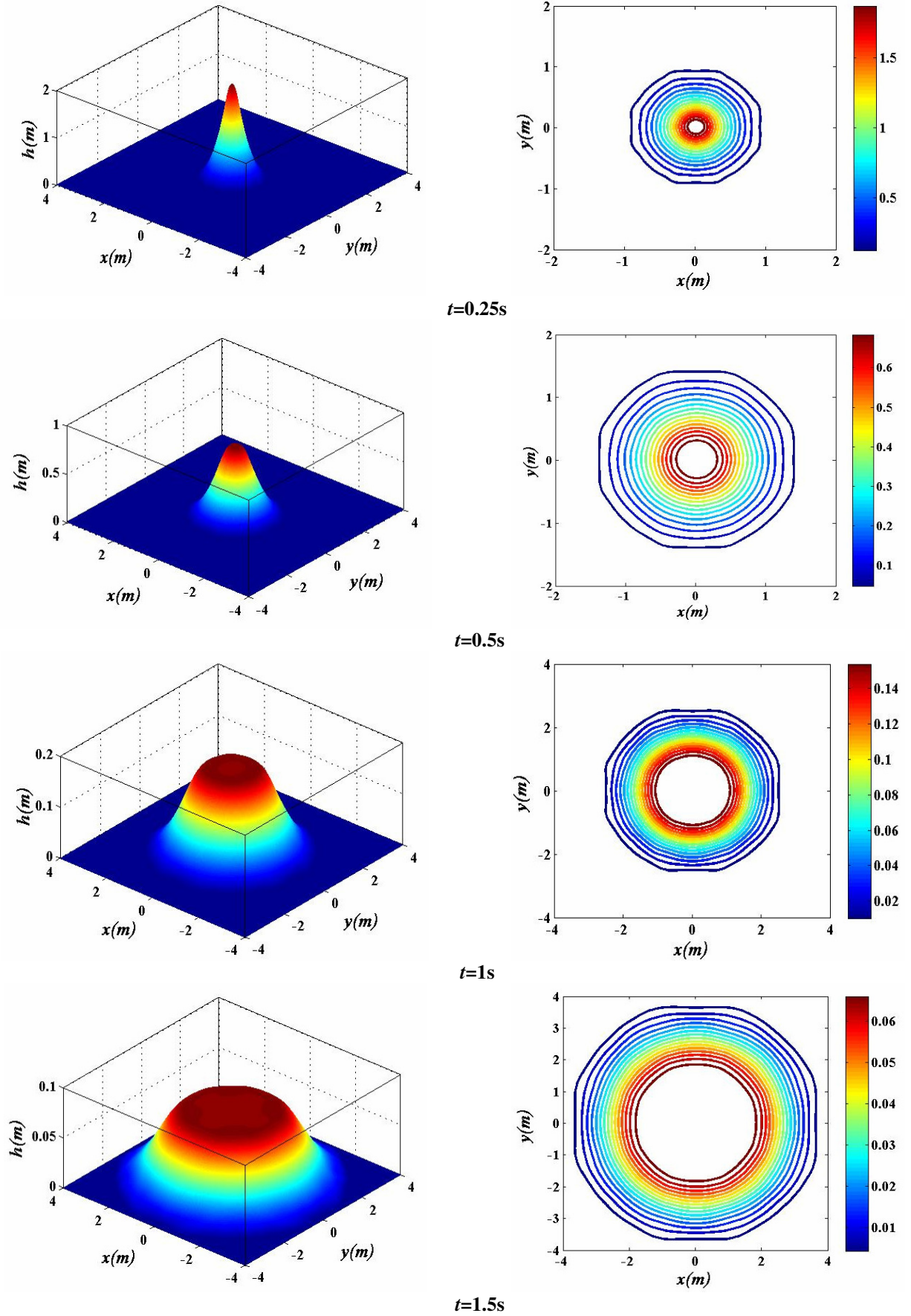
Figure 6.5. Radial dam-break over dry-state (water depth contours and 3-D water surface plot) with a modified f-wave approach and for 1024×1024 grid cells.

the current numerical technique with a new choice of wave speeds can cope with the propagation of rarefaction waves over the dry-state. The oscillatory portion observed in the counter lines may be due to the effect of MC limiter over the dry-state or due to the use of Cartesian cells. This is also reported for other approximate Riemann solvers (for instance see [85]). The number of grid cells and Courant number used here were chosen to 128×128 and 0.2 respectively. Figure 6.5 provides the free-surface and contour plots for the converged mesh obtained based on 1024×1024 grid cells and for the same time duration. Note that for the radial dam-break cases the acceleration due to gravity, g, was selected equal to $1\,\text{m/s}^2$ as was suggested in [47].

6.1.3 Rectangular Dam-Break over Wet-State

This test case was first proposed in [3] and contains a square $200\times200\text{m}^2$ tank divided into two equal portions with the area $200\times100\text{m}^2$. The initial water depth at upstream was chosen equal to be 10m while the depth of water at downstream is 5m. The water portions were separated with a very thin wall abruptly opened at time t=0s with a 70m gap. The initial condition for the problem is shown in Figure 6.6. Figures 6.7 and 6.8 provide the 3-D views for water depth elevation and contour plots respectively obtained at time t=7.2s and based on dimensional-splitting method. As can be seen in this Figure the shock wave
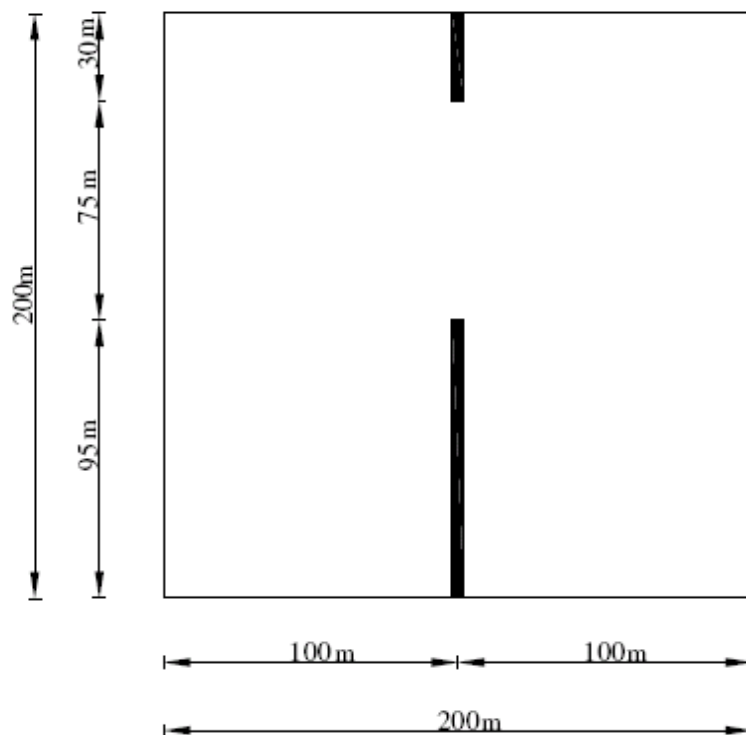
Figure 6.6. The initial condition for the rectangular dam-break.

125
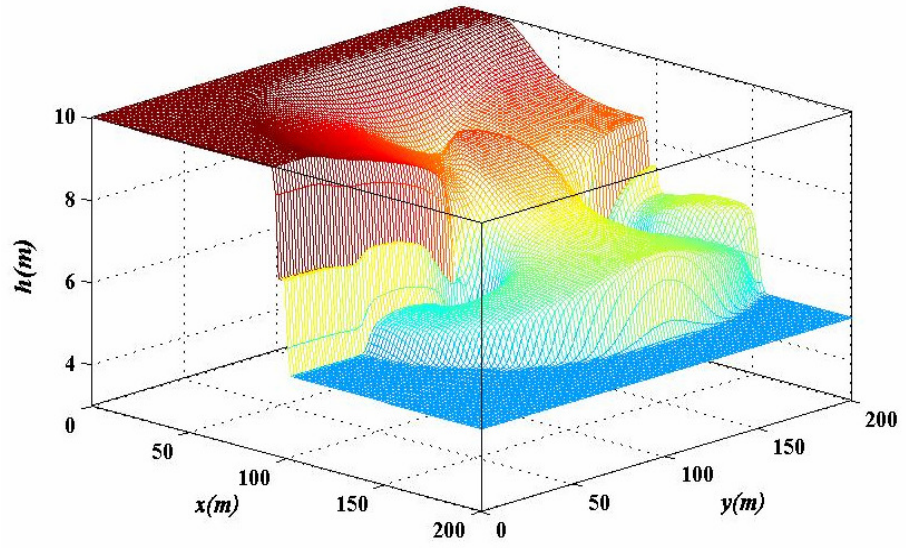
Figure 6.7. Water surface profile for the rectangular dam-break problem at time *t*=7.2s, calculation was performed based on 100×100 grid cells.
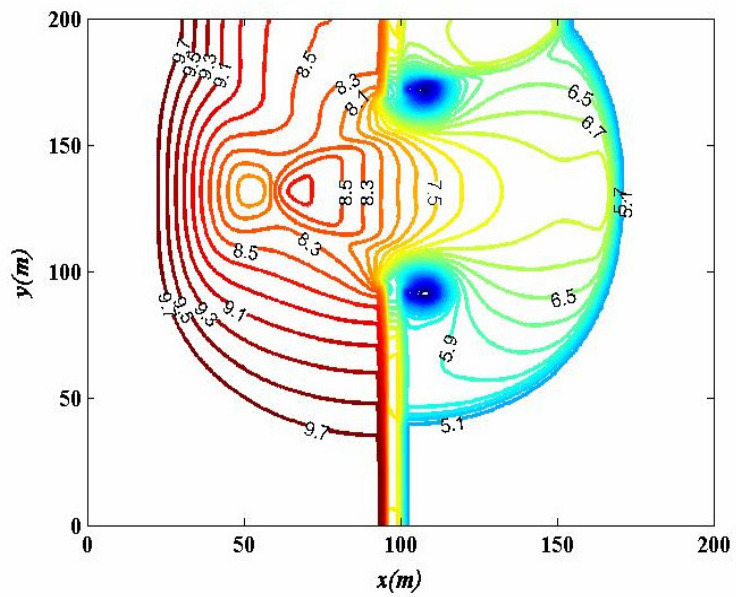
Figure 6.8. Counter plots for the rectangular dam-break problem computed for 100×100 grid cells.
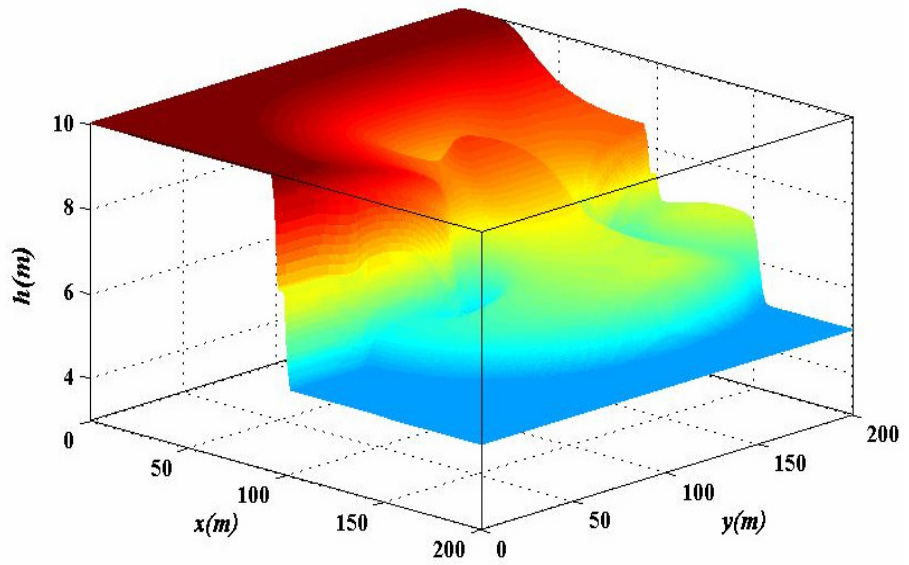
Figure 6.9. Water surface profile for the rectangular dam-break problem at time *t*=7.2s, calculation was performed based on 1024×1024 grid cells.
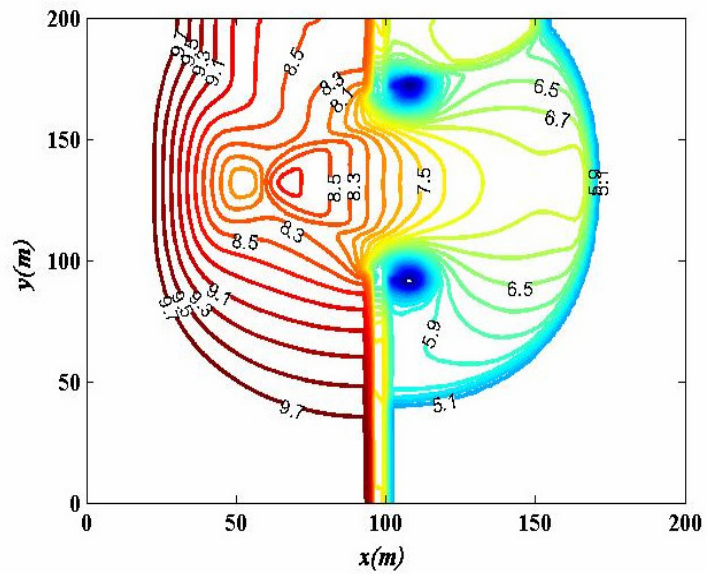
Figure 6.10. Counter plots for the rectangular dam-break problem computed for 1024×1024 grid cells.

again appears on the right side of the breach and the rarefaction waves move to opposite direction causes a dip in the free-surface. The vortices observed at the both side of breach (on the right-hand side of wall) may be created by the curved rarefaction waves travelling radially like the circular dam-break test case. The results are in close agreement with those reported in literature (see [3, 56, 69] for more details). For modelling the thin wall separating two levels of water, the mirror boundary conditions were employed which was explained in Chapter 3. The number of grid cells and the Courant number for the coarse mesh calculation were selected 100 ×100 and 0.5 respectively. Figures 6.9 and 6.10 demonstrate the results for fine grid computation achieved based on 1024×1024 computational cells.

6.1.4 Dam-Break Problem over Three Humps and Dry-State

Now a dam-break propagation over a dry-bed with complex topography is investigated. This problem was originally proposed in [37] and here, we will examine the test case with the initial condition defined in [51]. Very similar problems have been investigated by other researchers, [11, 17] . In a channel, 75m long and 30m wide, the dam is situated at 16m in the x-direction as shown in Figure 6.11. The initial water depth is 1.875m and the bed topography profile is defined by the following equations

$$z_b(x,y) = \max\left[0, 1 - \frac{1}{8}\sqrt{(x-30)^2 + (y-6)^2}, \right.$$
$$\left. 1 - \frac{1}{8}\sqrt{(x-30)^2 + (y-24)^2}, 3 - \frac{3}{10}\sqrt{(x-47.5)^2 + (y-15)^2} \right]. \tag{6.1}$$

For this particular problem the friction coefficient is evaluated as $C_f = 2gn_m^2/h^{1/3}$ to create the same friction terms given in [37] where $n_m = 0.018$ denotes the Manning coefficient. Figure 6.12 presents sequential plots for water surface and water depth at times $t = 0$s, 2s, $t=6$s, $t=12$s, $t=30$s, $t=40$s. The steady-state condition is reached after approximately $t=300$s. At time $t=2$s the flood waves with the wet/dry fronts reach the small hills and start to interact behind them. At time $t=6$s the small humps are partially inundated and the wet/dry fronts propagate around the higher mound. By time $t=12$s the higher mound is completely surrounded by the flood water and the water waves move toward the right boundary. At time $t=30$s the wave has collided with the right boundary, creating reflected shock waves that propagate back toward the higher mound. By time $t=40$s the reflected waves have

passed the small hills and reach to the left boundary. The process is continued until a stationary steady-state is reached, shown at time t=300s. Figure 6.13 illustrates a 3-D visualization for the water depth and discharge at the steady-state. The numerical results obtained here are in qualitative agreement with the results presented in [11, 17, 51]. The number of grid cells for this particular test-case was 512×512 and Cr=0.2. Note that the wall boundary condition is modelled by reflecting the interior data across the boundary and the discharge is made negative (see e.g. [46]). The mass error for the steady-state condition is less than 3.5×10^{-3} and is obtained based on the difference between the initial volume at time t=0s (1.875×30×16) and t=300s (899.9965).
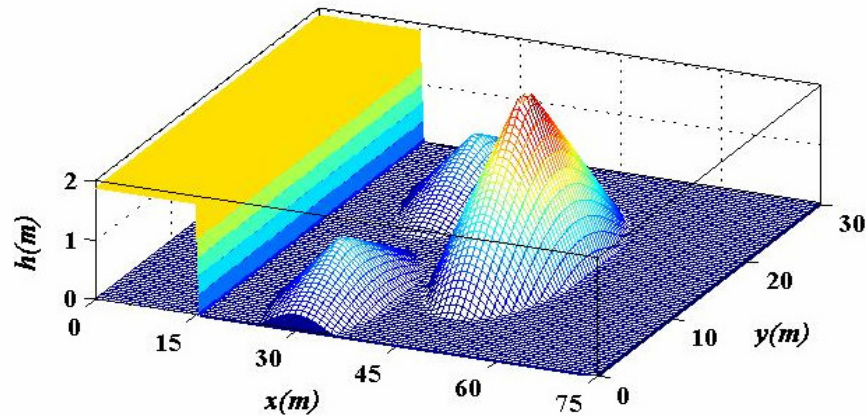
Figure 6.11. The initial condition for the dam-break problem over three humps.

6.2 Part II: The Two-Dimensional Shallow Water Results with the Efflux/Influx Source Terms

As mentioned above, this Section concerns the two-dimensional shallow water equations with the efflux/influx source term in the continuity equation. For the two-dimensional SWEs the efflux number takes the form $En = V / \sqrt{gD}$ where D is the sewage pipe diameter. For idealised efflux/influx cases comparisons will be made with the commercial Navier-Stokes solver STAR-CD with the free-surface represented by the volume of fluid (VOF) approach for the range of efflux number $En \leq 0.5$ (the same as one-dimensional problem) and the choice of $(k - \varepsilon)$ with high-Reynolds number. However, for the efflux test cases modelled by the Navier-Stokes equations no obvious difference is observed between the laminar and turbulent flow and with the laminar assumptions approximately the same results can be obtained. Here, first the case of an isolated efflux is solved based on the shallow water solver and good agreement is shown with results from the 3-D VOF
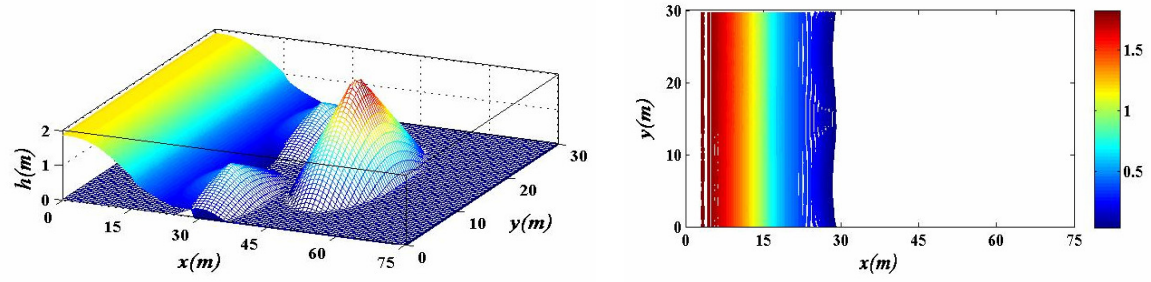
(a)   *t*=2s
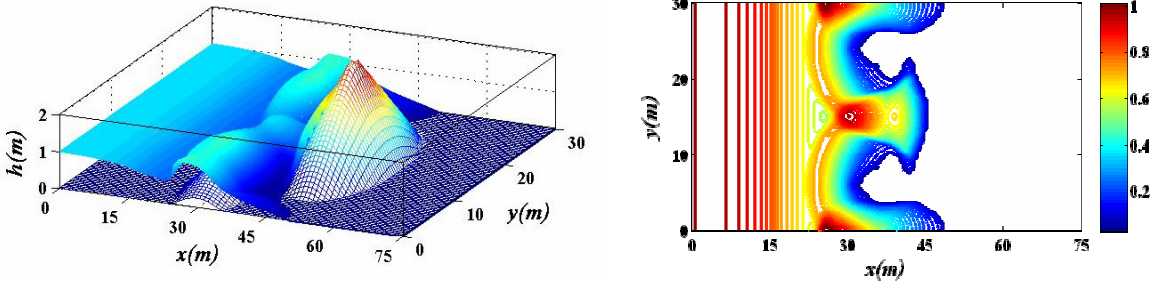
(b)   *t*=6s
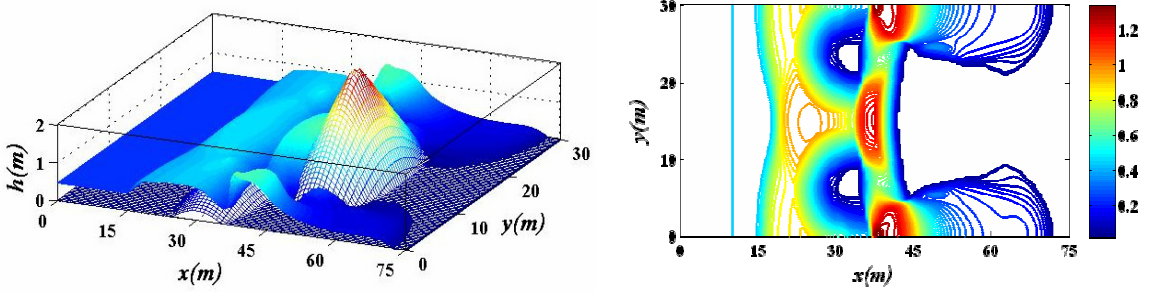
(c)   *t*=12s
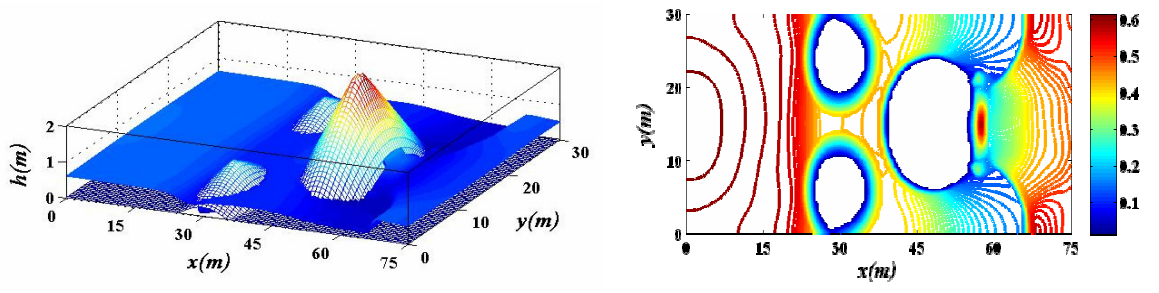
(d)   *t*=30s
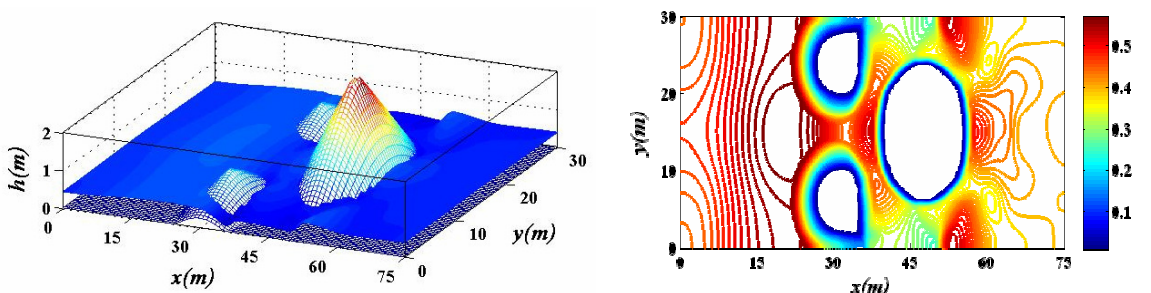
(e)   *t*=40s

Figure 6.12. The dam-break propagation over the three humps. The 3-D visualisation of water surface (Left column). Top view plans for water depth. (Right column).
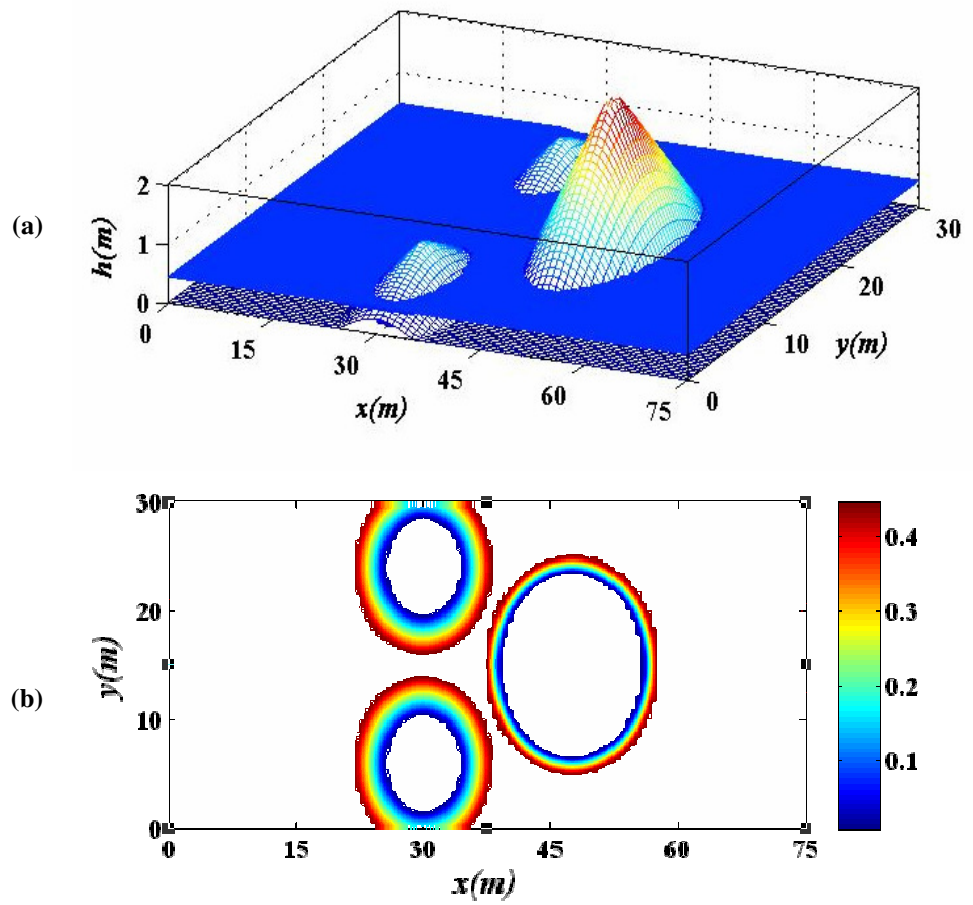
Figure 6.13. Steady-state condition for the dam-break propagation over three humps obtained approximately at *t*=300s. (a): 3-D visualisation. (b): Top view plan.

solver STAR-CD. Dam-break flow over an isolated efflux is then considered and good agreement is again shown between the shallow water solver and STAR-CD. The CFL number and the number of numerical mesh cells for both STAR-CD and shallow water solvers are defined separately for each numerical test case. A major portion of this part is also presented in [59].

6.2.1 Two-Dimensional Efflux Problem over Dry-State

This test case compares results from the two-dimensional SWEs with efflux source terms with results from the STAR-CD VOF code, where the assumption of laminar flow or k-ε turbulence modelling made negligible difference. A VOF factor of 0.5 defined the fluid surface in the normal way. In this problem efflux vertical velocities of 0.3m/s and 0.5m/s are imposed in a dry domain [-2m, 2m] × [-2m, 2m] through the discharge hole with a diameter of 0.25m located at origin of the domain. These exit velocities produce efflux numbers equal to $En=0.2$ and $En=0.32$ respectively. Note that for the isolated efflux in 1-D $C_f = 0.015$ gave good agreement with STAR-CD with a no-slip solid boundary condition [60] and in two-dimensional agreement is also close but $C_f = 0.03$ gives best agreement. The reason for the higher value in two-dimensional problems is probably to account for the radial dissipation of energy over an expanding arc. Figures 6.14 and 6.15 show 3-D plots for the water surface at time 0.5s, 1s, 1.5s and 2s calculated from both the SWEs and the STAR-CD VOF code. As can be seen here, the SWEs and the VOF code give nearly identical results for the efflux velocity $V=0.5$m/s. The only discrepancies appear at the wave fronts where the shallow water code produces smoother profiles. The intercept plots for the vertical slice located at y=0m were depicted in Figures 6.16 and 6.17 for the efflux velocities 0.3m/s and 0.5m/s respectively. The shallow water solver takes approximately 392s to reach time $t=2$s while the STAR-CD calculation takes 34200s on the same computer processor. For the STAR-CD calculation a uniform mesh of 256×256×40 cells was used with additional refined cells around the exit. The SWEs used 512×512 cells with the CFL number of $Cr = 0.2$. Tables 6.1 and 6.2 show the l_2 and l_∞ differences between the SWEs and the VOF code, which were calculated as

$$l_2 = \frac{\sqrt{\sum_i (dh_i)^2}}{N} \qquad \text{and} \qquad l_\infty = \max(dh_i), \qquad (6.2)$$

(a) *t*=0.5s (SWEs)

(b) *t*=0.5s (N-S)

(c) *t*=1s (SWEs)

(d) *t*=1s (N-S)

(e) *t*=1.5s (SWEs)

(f) *t*=1.5s (N-S)

(g) *t*=2s (SWEs)

(h) *t*=2s (N-S)
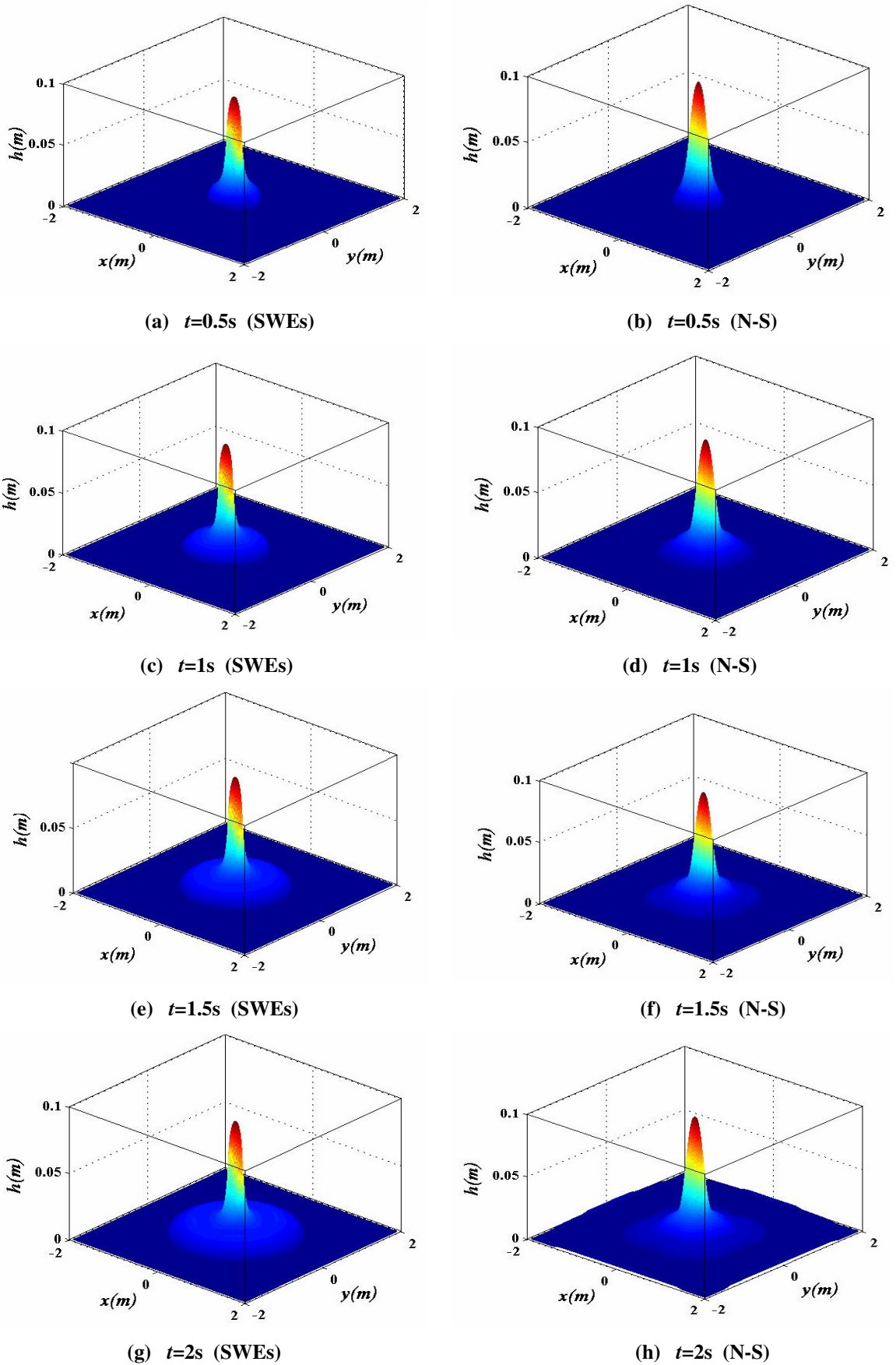
Figure 6.14. The 3-D water depth plots for efflux problem over dry-state with the efflux velocity *V*=0.5 m/s and *En*=0.32for *t*=0.5, 1, 1.5 and 2. Left column: two-dimensional SWEs results (a, c, e and g). Right column: Navier-Stokes results solved base on STAR-CD (b, d, f and h) and with the VOF=0.5.

133
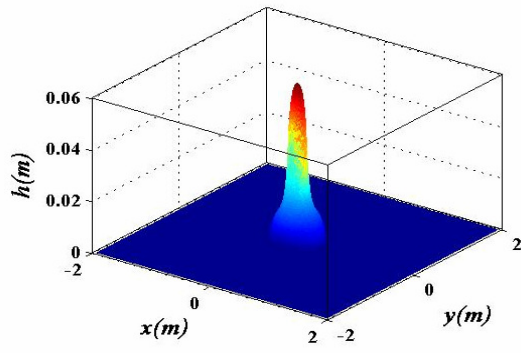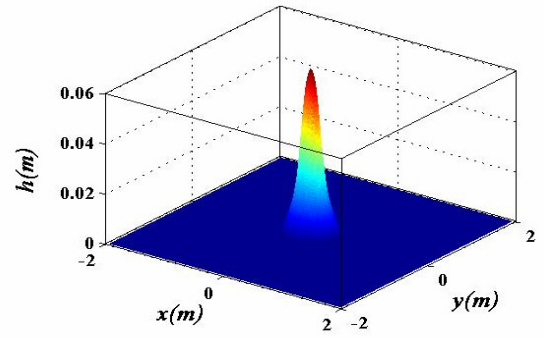
(a) *t*=0.5s (SWEs)
(b) *t*=0.5s (N-S)
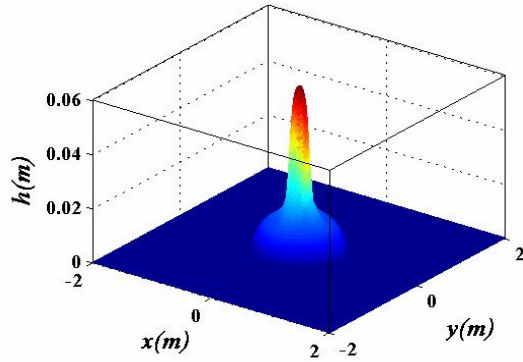
(c) *t*=1s (SWEs)
(d) *t*=1s (N-S)
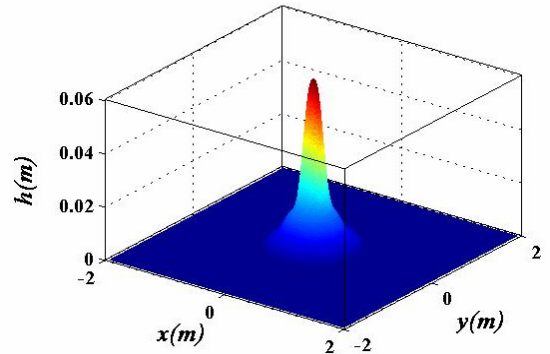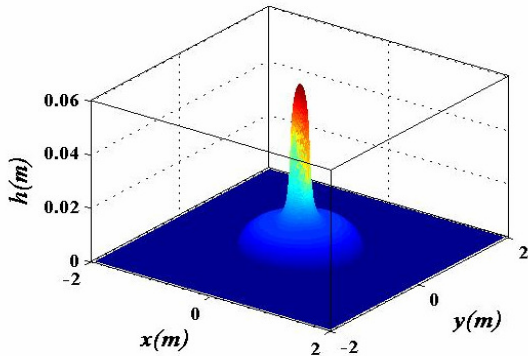
(e) *t*=1.5s (SWEs)
(f) *t*=1.5s (N-S)
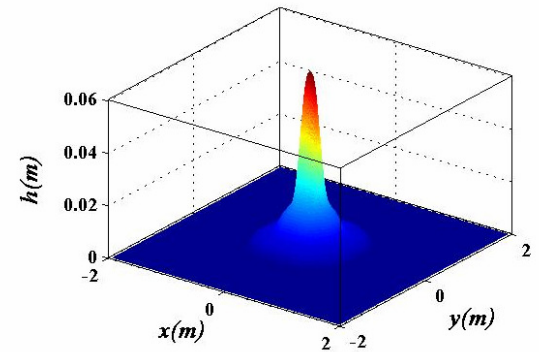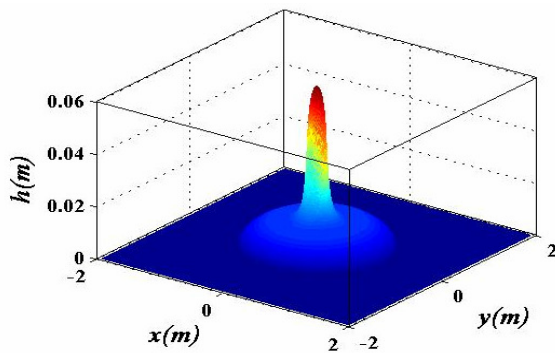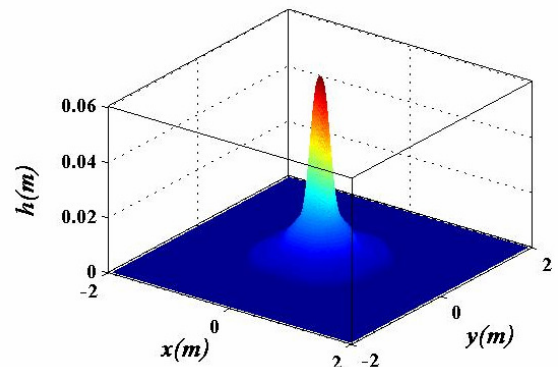
(g) *t*=2s (SWEs)
(h) *t*=2s (N-S)

Figure 6.15. The 3-D water depth plots for efflux problem over dry-state with the efflux velocity *V*=0.3 m/s and *En*=0. 2 for*t*=0.5, 1, 1.5 and 2. Left column: two-dimensional SWEs results (a, c, e and g). Right column: Navier-Stokes results solved based on STAR-CD (b, d, f and h) and with the VOF=0.5.
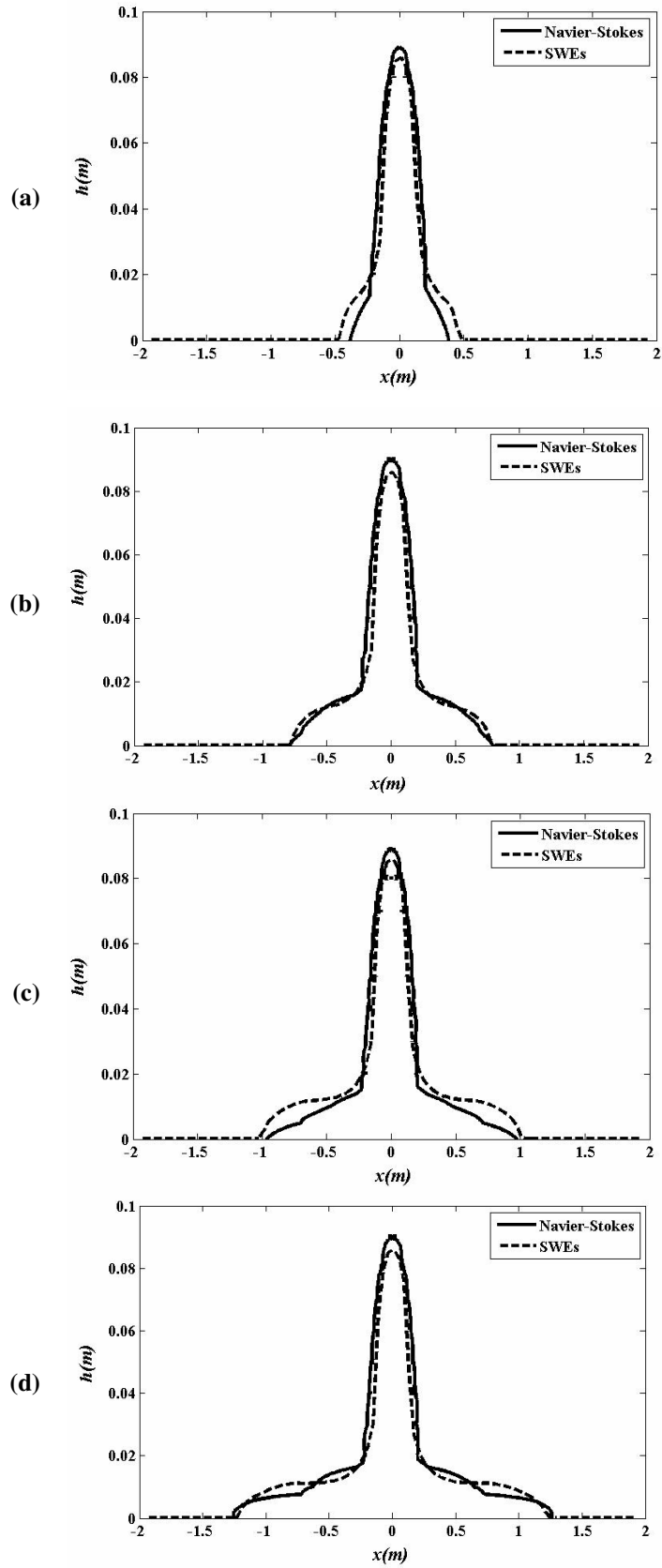
Figure 6.16. The intercept plots for efflux problem over dry-state with the efflux velocity *V*=0.5 m/s and *En*=0.32 for both STAR-CD (solid line) and SWEs (dashed line) for time *t*= 0.5, 1, 1.5 and 2s (a-d).
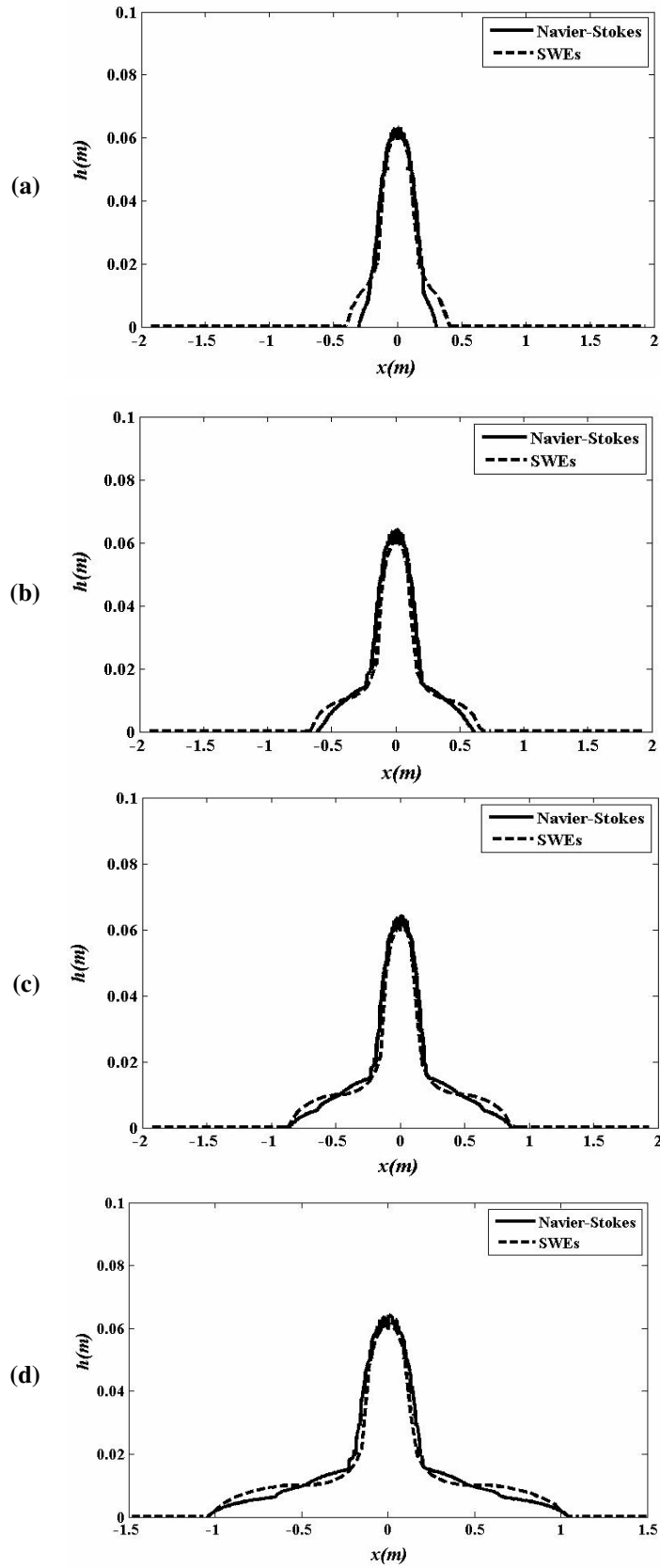
Figure 6.17. The intercept plots for efflux problem over dry-state with the efflux velocity V**=0.3 m/s and** En**=0.22 for both STAR-CD (solid line) and SWEs (dashed line) for time** t**= 0.5, 1, 1.5 and 2s (a-d).**

Table 6.1. The l_2 and l_∞ error and non-dimensional norms for the efflux velocity V=0.3 m/s and En=0.2.

Time(s)	l_2	l_2/dh_{max}	dh_{max}	l_∞	l_∞/d_{max}
0.5	3.1×10^{-3}	4.9×10^{-2}	0.0630	1.2×10^{-2}	1.9×10^{-1}
1	1.3×10^{-3}	2×10^{-2}	0.0632	1.2×10^{-2}	1.8×10^{-1}
1.5	6.8×10^{-3}	1×10^{-1}	0.0632	1.2×10^{-2}	1.8×10^{-1}
2	8.1×10^{-3}	1.2×10^{-1}	0.0632	1.4×10^{-2}	2.2×10^{-1}

Table 6.2. The l_2 and l_∞ error and non-dimensional norms for the efflux velocity V=0.5 m/s and En=0. 32.

Time(s)	l_2	l_2/dh_{max}	dh_{max}	l_∞	l_∞/dh_{max}
0.5	5.3×10^{-3}	6.4×10^{-2}	0.0824	1.7×10^{-2}	2×10^{-1}
1	7.6×10^{-3}	9.1×10^{-2}	0.0832	1.6×10^{-2}	1.9×10^{-1}
1.5	1.2×10^{-2}	1.4×10^{-1}	0.0832	1.4×10^{-2}	1.6×10^{-1}
2	1.2×10^{-2}	1.4×10^{-1}	0.0832	2.2×10^{-2}	2.6×10^{-1}

where dhi is the difference between the SWEs and the VOF depth. The non-dimensional error was also computed by dividing by the maximum depth (dh_{max}). l_∞ gives the largest difference for water elevation between STAR-CD and the SWEs, whereas l_2 gives an estimate of the average error over the domain. As can be seen in Tables 6.1 and 6.2 the maximum difference between the shallow water and the STAR-CD results is observed at the wave fronts, due to the effect of viscous terms and non-hydrostatic pressure.

6.2.2 Two-Dimensional Dam-Break with Efflux

This test case investigates the interaction of dam-break flow over a dry bed with efflux from a circular hole. This test case involves the collision of interacting bores. The computational domain is set to [-2m, 2m] × [-0.75m, 0.75m] and the initial dam face is along x=0m with a depth of 0.3m. The domain contains the circular hole for efflux with a diameter 0.2m with centre at x=1m, y=0m. An efflux velocity V=0.2m/s is used giving an efflux number En=0.143. The numerical results for the SWEs and the VOF code are shown in Figure 6.18 (a-d). The interaction of dam-break propagation and efflux waves, start approximately at t=0.4s and the resulting waves spread out in both directions until collision with the solid wall at t=0.8s. In general, the SWE results are in close agreement with the VOF code. Surface profiles are shown in Figure 6.19 for the mid section vertical plane at y=0m, for the SWEs and the VOF code where the agreement is consistent with the results observed in 1-D presented in Chapter 4. For the SWEs 512×512 grid cells with a CFL number equal to 0.2 were used. The STAR-CD VOF run used 400×400×40 grid cells.

(a)　　　　　　　　**t=0.4s (SWEs)**　　　　　　　　　　　**t=0.4s (N-S)**

(b)　　　　　　　　**t=0.6s (SWEs)**　　　　　　　　　　　**t=0.6s (N-S)**

(c)　　　　　　　　**t=0.8s (SWEs)**　　　　　　　　　　　**t=0.8s (N-S)**

(d)　　　　　　　　**t=1s (SWEs)**　　　　　　　　　　　**t=1s (N-S)**
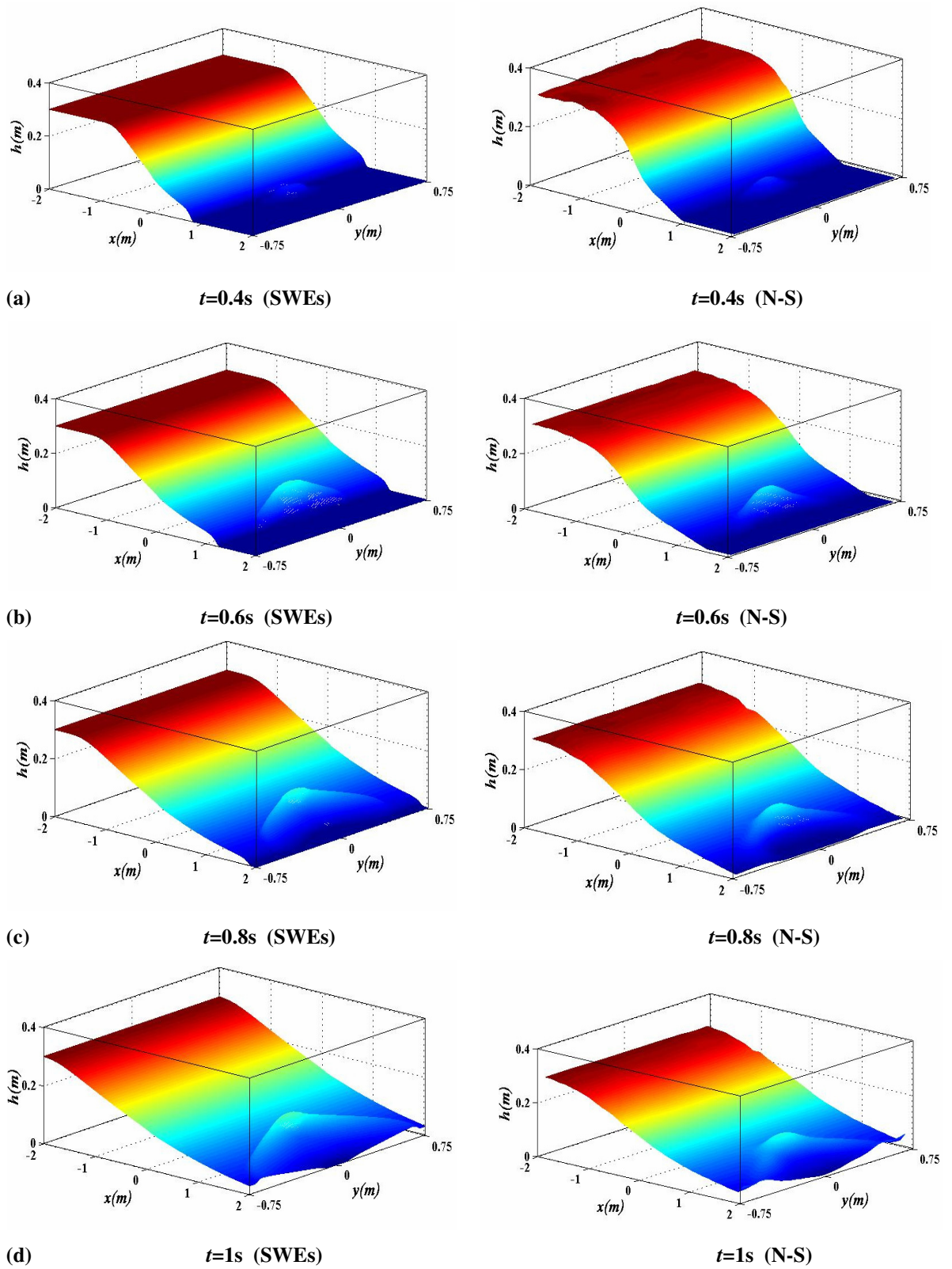
Figure 6.18. The 3-D view plots for the dam-break problem with the efflux discharge for both STAR-CD (VOF=0.5) and shallow water solver for time *t*=0.4, 0.6, 0.8 and 1s.
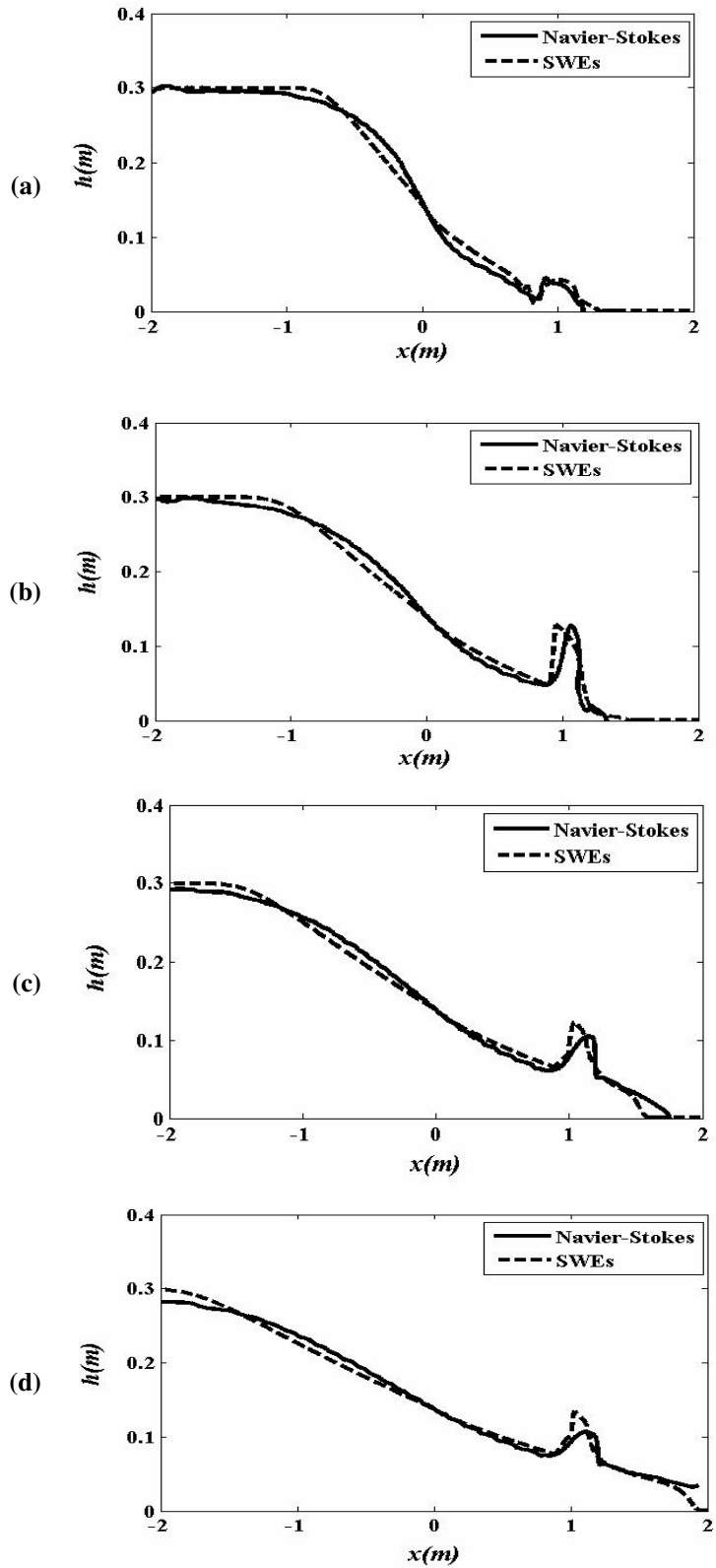
Figure 6.19. The mid section vertical plane for the dam-break problem with the efflux discharge for both STAR-CD (VOF=0.5) and shallow water solver for time *t*=0.4, 0.6, 0.8 and 1s (a-d).

Table 6.3 shows the difference analysis between the two approaches. This test case is also presented in [61].

Table 6.3. The l_2 and l_∞ error and non-dimensional norms Two-dimensional dam-break with efflux.

Time(s)	l_2	l_2 / dh_{max}	l_∞	l_∞ / d_{max}
0.4	1.2×10^{-2}	3.6×10^{-2}	2.2×10^{-2}	7.3×10^{-3}
0.6	1.1×10^{-2}	3.6×10^{-2}	2.1×10^{-2}	7×10^{-3}
0.8	2.5×10^{-2}	4.6×10^{-2}	2.2×10^{-2}	7.3×10^{-3}
1	9.8×10^{-2}	5.6×10^{-2}	2.2×10^{-2}	7.3×10^{-3}

6.3 Conclusions

In this Chapter we have presented the numerical results for two-dimensional SWEs based on a modified f-wave approach defined in Chapter 5 for two-dimensional SWEs. For the standard shallow water benchmarks a very close agreement has been obtained between the presented solver and other researcher work. Modelling flood propagation over complex terrain was then demonstrated. For efflux alone good agreement has been achieved between the SWEs and the STAR-CD VOF solver. For the dam-break with the efflux wave interaction results from the SWEs and VOF solvers are very close. In the next Chapter we will presented the inundation problems over underground pipe networks based on two-dimensional SWEs.

Chapter 7 : FLOOD PROPAGATION OVER URBAN AREAS WITH UNDERGROUND PIPE NETWORKS

In this Chapter a more realistic flood situation is considered which models the inundation over the complex underground sewage pipe network. The efflux number $En \le 0.5$ is again used to avoid the near field effect of non-hydrostatic pressure. We first explain a complete solution for the underground pipe network analysis. Then, the flood propagation over two different sewage network is presented. In fact, in this Chapter we have generalised the flood propagation in Section 4.2.5 for two-dimensional shallow water problems. The flooding over the sewage pipe networks with the multiple blockage scenarios is also presented as a final test case.

7.1 Underground Pipe Network Analysis

The mathematical method for computing the influx/efflux discharge due to an underground pipe network is described in this Section, assuming the pipes are initially full. As the free-surface flow moves over the underground pipes, the head of water causes influx through the closest ports, causing efflux through downstream ports in initially dry areas. Here, a port is the connection between a pipe node and the bed. The calculation of efflux requires the solution of a set of non-linear equations at each time step. The method with unknown effluxes is different from general pipe network analysis where the unknowns are the pipe discharges; here an additional set of equations has to be taken into account. In Figure 7.1, we have an example pipe network with 6 nodes and 7 pipes. In Figure 7.1a the head H_{t1} at point (1), created by dam-break propagation, causes efflux through the nodes (2-6). The red arrows show the initial assumption for the flow direction within the pipes. In general to compute the efflux from the ports, the following set of equations should be solved simultaneously,

1-   The Hydraulic Grade Lines (HGL) equations for $Nj - K$ junctions where Nj denotes the number of junctions and K represents the number of input heads (H_t) involved in the solution.

2-   The head loss equations within each pipe for $Np - P$ pipes where Np implies the number of pipes and P denotes the number of pipes with both junctions submerged and finally,

3-   The continuity equations for $Nj - K$ junctions to effluxes for unsubmerged junctions.

The HGL equations for each node j can be written as [40]
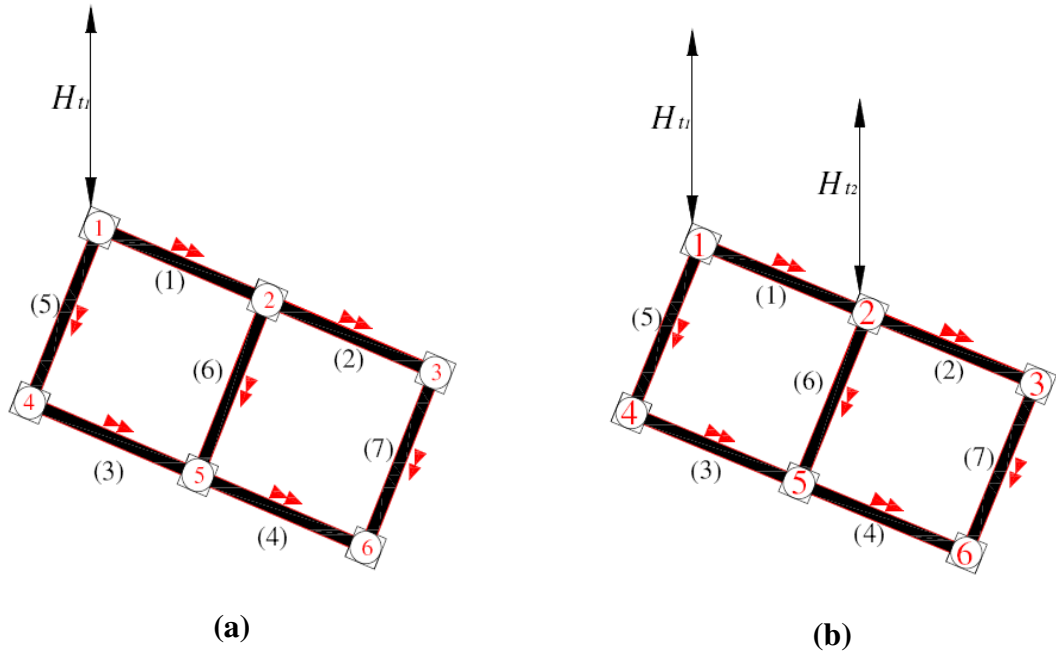
Figure 7.1. The sewage pipe network with 7 pipes and 6 nodes. (a): an underground pipe network with single total head. (b): an underground pipe network with two total heads.

$$Y_j = \frac{(qn_j/Cm_j)^2}{2gA_a^2} - HGL_j = 0, \tag{7.1}$$

where qn_j denotes the efflux and HGL implies the pressure head at junction j and Cm_j and A_a represent the orifice coefficient and the cross-sectional area of the ports. The total number of HGL equations is equal to the number of efflux junctions ($Nj - K$). The head loss for the pipe i connected between water elevation (H_t) and the node M, including velocity head can be expressed as

$$Y_{Nj-K+i} = H_t - HGL_M - (1 + f_i \frac{L_i}{D_i}) \frac{Q_i^2}{2gA_i^2} = 0. \tag{7.2}$$

For the rest of pipes connected between unsubmerged nodes M and N the head loss equations can be written as

$$Y_{Nj-K+i} = HGL_M - HGL_N - (f_i \frac{L_i}{D_i}) \frac{Q_i^2}{2gA_i^2} = 0, \tag{7.3}$$

where, f is the Darcy-Weisbach friction factor, $Q_{p+1}, Q_{P+2}, ..Q_{Np-P}$ indicate the discharge within each pipe and D_i is the pipe diameter and finally L_i is the pipe length. The values of friction factor, f_i, can be evaluated from the explicit Swamee-Jain formula defined in [79], given by

$$ f = \frac{0.25}{\left[\text{Log}(\frac{\varepsilon_p}{3.7D} + \frac{5.74}{Re^{0.9}}) \right]^2}, $$
(7.4)

where, ε_p is the roughness height of the pipe surface, and Re is the Reynolds number. Finally continuity is required for each junction, generating a further set of equations. For example, for the junction j, the continuity equation can be written as

$$ Y_{Np-P+Nj+j} = \sum Q_{MN} - qn_j = 0, $$
(7.5)

where $\sum Q_{MN}$ is the summation of ingoing and outgoing flows at node j . Therefore the vector Y is given by

$$ \begin{aligned} Y(Y_1, Y_2, &\cdots Y_{Nj-K}, Y_{Nj-K+1}, Y_{Nj-K+2,} \cdots Y_{Nj-K+Np-P}, \\ & Y_{Nj-K+Np-P+1}, Y_{Nj-K+Np-P+2}, \cdots Y_{2(Nj-K)+Np-P})^T . \end{aligned} $$
(7.6)

The vector Y is solved by a Newton iterative method for obtaining the vector of unknowns, X , which comprises the effluxes, hydraulic grade lines (HGL) and the discharge within the pipes where

$$ X = (qn_{k+1}, qn_{k+2,} \dots qn_{Nj-K}, HGL_{K+1}, HGL_{K+2}, \cdots, HGL_{Nj-K}, Q_{P+1}, Q_{P+2}, \cdots Q_{Np-P})^T . $$
(7.7)

Then, the Newton formula for the above system can be expressed as

$$ X^{m+1} = X^m + dY^m, $$
(7.8)

where m is the iteration number and dY is calculated by solving the following linear system,

$$J(X) \, \mathrm{d}Y \ = \text{-}Y(X) \, ,$$

(7.9)

where $J(X)$ is called the Jacobian matrix for the system $Y(X)$ described above and can be determined as

$$J(X) = \begin{bmatrix} \dfrac{\partial Y_1}{\partial X_1} & \dfrac{\partial Y_1}{\partial X_2} & \cdots & \dfrac{\partial Y_1}{\partial X_{2(Nj-k)+Np-P}} \\[2mm] \dfrac{\partial Y_2}{\partial X_1} & \dfrac{\partial Y_2}{\partial X_2} & \cdots & \dfrac{\partial Y_2}{\partial X_{2(Nj-k)+Np-p}} \\[2mm] \vdots & \vdots & \ddots & \vdots \\[2mm] \dfrac{\partial Y_{2(Nj-k)+Np-p}}{\partial X_1} & \dfrac{\partial Y_{2(Nj-k)+Np-p}}{\partial X_2} & \cdots & \dfrac{\partial Y_{2(Nj-k)+Np-p}}{\partial X_{2(Nj-k)+Np-p}} \end{bmatrix}.$$

(7.10)

The Jacobian matrix shown in Equation (7.10) is a sparse and non-positive definite matrix and standard solver is used for solving the linear system (7.9). We use the **LU** decomposition with partial pivoting using Crout's algorithm [66]. The number of iterations for the Newton approach is carried until the Euclidean norm for the vector of Y becomes less that 10^{-6} which is defined as

$$\|Y\|_2 = \left\{ \sum_{i=1,2Nj+Np} Y_i^{\,2} \right\}^{1/2}.$$

(7.11)

Less than 10 iterations are generally required. In summary therefore, the pipe network with unknown effluxes contain $2(Nj-K)+Np-P$ equations and may be solved using the Newton iterative scheme. For example for the pipe network depicted in Figure 7.1a ($Np = 7, Nj - 1 = 6$, $K = 1, P = 0$) 17 equations should be solved simultaneously. In the case that the water surface reaches point (2) (Figure 7.1b) the head (water elevation) at point (2) is also incorporated into the solution and the new K and P take the values of 2 and 1 respectively. Then, the initial approximation for discharge within the pipe (1) can be obtained by the following Equation

$$Q_1 = \left[\frac{H_{t1} - H_{t2}}{Kf_1} \right]^{0.5},$$

(7.12)

where H_{t2} shows the water elevation at junction 2 and $Kf_1 = \frac{8f_1 L}{g\pi^2 D_1^5}$ is a discharge

coefficient. This discharge should be considered as providing an additional head for the point 2, that is,

$$\Delta H_{t2} = \frac{Cm_1^2 Q_1^2}{2gA_a^2},$$

(7.13)

so the new total head for the node 2 (H_{t2}) can be corrected as $H_{t2} + \Delta H_{t2}$, and system described in Equation (7.9) should be solved for $2(Nj - 2) + Np - 1$ equations to determine the new efflux discharge for the downstream nodes. Note that in the above solution we have neglected the effect of junction losses for the efflux computation and only the friction terms were considered into the solution. However the effect of junction losses can be included into Equations (7.1) to (7.3) (see [40] for more details).

7.2 The Numerical Results for Flood Propagation over Underground Pipe Network

In this Section we will investigate several numerical results with the two-dimensional SWEs to simulate the flood propagation over underground pipeline systems. The surface flow solver is first coupled with an underground pipe network solver for general predictions. The pipe network is considered to be always full although this may be generalised for initially partially full pipes. Then the flood propagation over an idealised city with multiple efflux interaction is presented. In all of these test cases the efflux discharge is computed based on the numerical approach described in the previous Section. The CFL number and the number of computational cells are defined separately for each test case.

7.2.1 Dam-Break Propagation over Sewage Pipe Networks

Demonstration test cases are now considered with dry bed dam-break propagation over an underground pipe network causing multiple bed efflux/influx discharges. The flood domain is set to [0, 20m] × [0, 20m] and the dam face is located at *x*=4m with an initial

depth equal to 0.6m, released at t=0s. Free-surface propagation over two different pipe networks are shown. The initial conditions for the first pipe network are depicted in Figure 7.2. As shown the underground network comprises 12 pipes with 9 connecting ports above pipe junctions. The pipe network is in a horizontal plane with a square boundary with one side 11.5^o to the dam face (y-direction). The red arrows in this Figure show the initial assumption for the flow within the pipe network. Figure 7.3 displays isometric views and contour plots for dam-break propagation with efflux interaction. When the dam starts to break the flood wave moves towards the ports and reaches the first port (node 1) at time t≈0.3s and imposes a pressure head which causes efflux from the downstream ports. The efflux discharges are evaluated from the methodology given in Section 7.1. This means every time the surface waves reaches a port the water elevation at that point defines the total head.

By time t=2s the surface wave collides with the flows issuing from the second row of ports. Moreover there are lateral interactions between the pipe outflows and the resulting flood waves move towards the downstream ports. As water passes through the ports situated in the second row the influx discharge is imposed creating additional outflow flow from the downstream ports. At time t =4s the second row is fully submerged by the surface waves. The resulting curved bores propagate and hit the solid wall at the right boundary. Eventually, at time t=8s the reflected waves propagate toward the left boundary. Tables 7.1-7.4 indicate the network analysis and provide the data for the pipe discharge, efflux discharge, HGL (pressure head) and the water elevation over the ports (H_t) for different times t=0.4, 1, 2 and 4s. These tables demonstrate that the continuity conditions have been fully met around each junction. For instance at time t=2s the efflux discharge for junction 4 can be verified by flow within the pipes (7), (3) and (10) (1.1568-0.4547-0.5281=0.174). It can also be discerned from the tables that as the free-surface flow crosses over the second row of ports the efflux discharge is increased which is due to the effect of upstream heads over the ports. The maximum efflux number for this test case does not exceed En=0.44. For the SWEs computation there are 512×512 grid cells. The CFL number was 0.2 and the orifice coefficient defined in Equation (7.1) was chosen as 0.6. The total computer time for this test case to t=8s was 1724s.

 Figure 7.4 shows the initial condition for the dam propagation over a more complex pipe network which contains 40 pipes and 25 junctions. The numerical results for the free-
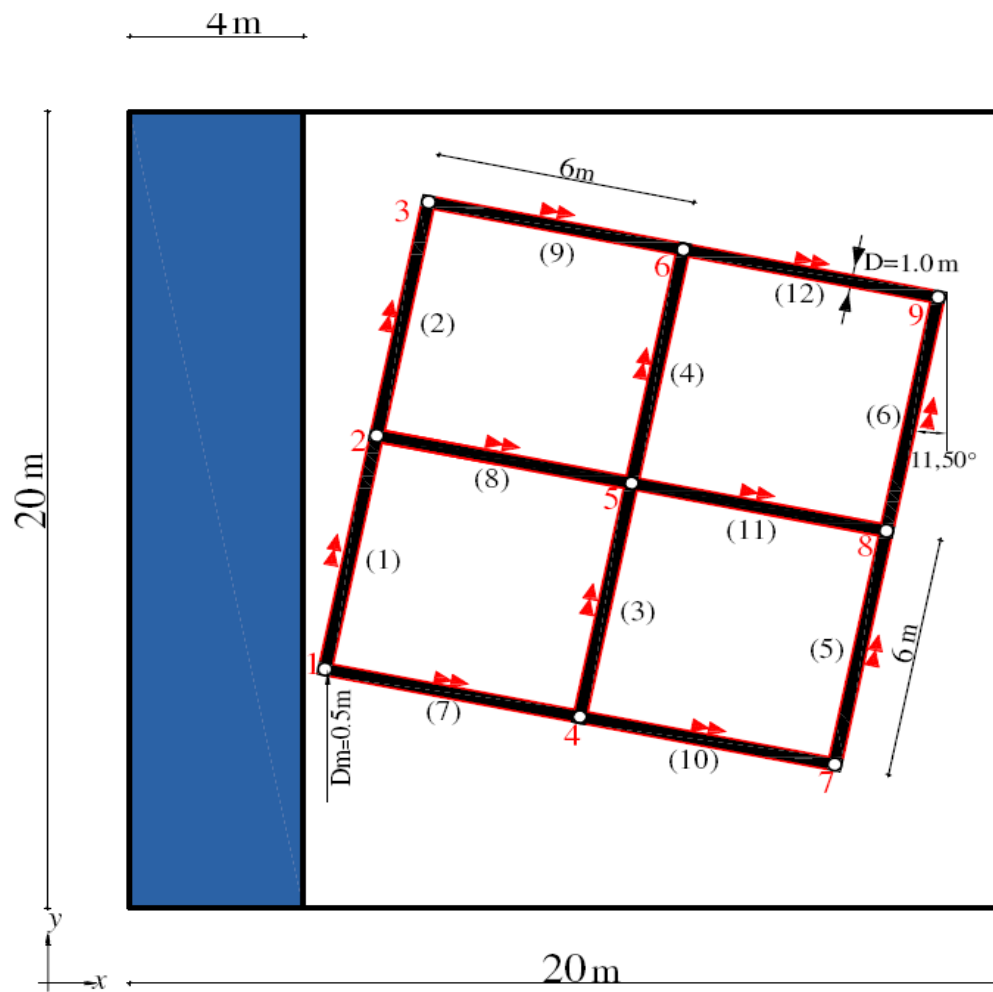
Figure 7.2. The initial problem for the dam-break over underground pipe networks with 12 pipes and 9 nodes. *Dm* is the port diameter and *D* shows pipe diameter.
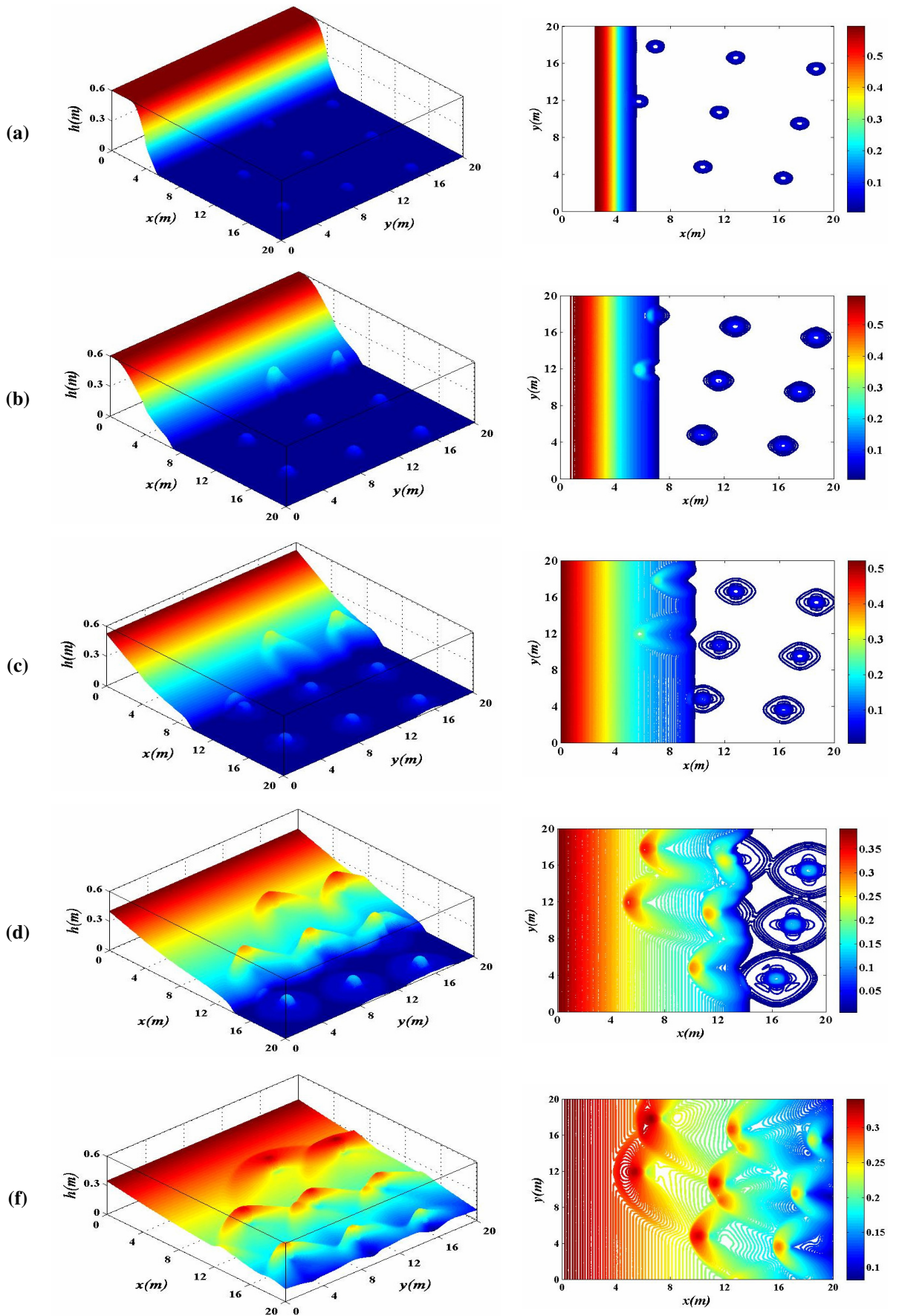
Figure 7.3. The dam-break propagation over sewage pipe network defined in Figure 7.2 for time *t*=0.4, 1, 2, 4 and 8s (a-f). Colours blue to red correspond to the water depth 0-0. 6m.

148

Table 7.1. Pipe discharges, nodal heads and the efflux discharge for the sewage network defined in Figure 7.2 at time *t*=0.4s.

Pipe Number	Q(m^3/s)	Node Number	Efflux Discharge	HGL(m)	Ht(m)
1	0.5380	1	----		0.1048
2	0.1273	2	0.1331	0.0775	-----
3	0.0372	3	0.1333	0.0777	-----
4	-0.2453	4	0.1339	0.0784	-----
5	0.2253	5	0.1339	0.0784	-----
6	0.5194	6	0.1333	0.0777	-----
7	0.5290	7	0.1326	0.0769	-----
8	0.2776	8	0.1321	0.0762	-----
9	-0.0060	9	0.1348	0.0794	-----
10	0.3579	-----	-----	-----	-----
11	0.4261	-----	-----	-----	-----
12	-0.3846	-----	-----	-----	-----

Table 7.2. Pipe discharges, nodal heads and the efflux discharge for the sewage network defined in Figure 7.2 at time *t*=1s.

Pipe Number	Q(m^3/s)	Node Number	Efflux Discharge	HGL(m)	Ht(m)
1	----	1	----	----	0.1766
2	----	2	----	----	0.1773
3	-0.2816	3	----	----	0.1292
4	-0.3429	4	0.1766	0.1364	-----
5	-0.7352	5	0.1760	0.1354	-----
6	-0.3619	6	0.1751	0.1340	-----
7	-0.6660	7	0.1742	0.1326	-----
8	0.6662	8	0.1783	0.1390	-----
9	1.0572	9	0.1773	0.1374	-----
10	-0.5610	-----	-----	-----	-----
11	0.5516	-----	-----	-----	-----
12	0.5392	-----	-----	-----	-----

Table 7.3. Pipe discharges, nodal heads and the efflux discharge for the sewage network defined in Figure 7.2 at time *t*=2s.

Pipe Number	Q(m^3/s)	Node Number	Efflux Discharge	HGL(m)	Ht(m)
1	----	1	----	----	0.2211
2	----	2	----	----	0.2375
3	0.4547	3	-----	-----	0.2157
4	0.8795	4	0.1740	0.1324	-----
5	0.3519	5	0.1756	0.1348	-----
6	0.6174	6	0.1814	0.1439	-----
7	1.1568	7	0.1761	0.1356	-----
8	1.0429	8	0.1771	0.1371	-----
9	-1.1355	9	0.1800	0.1416	-----
10	0.5281	-----	-----	-----	-----
11	0.4426	-----	-----	-----	-----
12	-0.4374	-----	-----	-----	-----

surface propagation over this pipe network are shown in Figure 7.5. As shown here the water surface crosses over the first surface port at time $t \approx 0.3s$. Note that at this point the Jacobian matrix for the underground solver, has the size of 88×88 which corresponds to ($2 \times 24 + 40 = 88$) unknowns. At time t=1s all of the ports in the first row are inundated by the free-surface flow. Differences in efflux discharges for the downstream nodes are evident. By time t=2s the flood waves and outflow discharges from the third row of ports are colliding together. The same behaviour is also observed for time t=4 s. At time t=8s all ports are submerged and the surface wave starts to propagate upstream. The run time up to t=8s is 1905s.

Table 7.4. Pipe discharges, nodal heads and the efflux discharge for the sewage network defined in Figure 7.2 at time t=4s.

Pipe Number	$Q(m^3/s)$	Node Number	Efflux Discharge	HGL(m)	Ht(m)
1	----	1	----	----	0.2508
2	----	2	----	----	0.2532
3	----	3	-----	-----	0.2453
4	----	4	----	-----	0.2013
5	-1.2240	5	----	-----	0.1719
6	-1.0127	6	-----	-----	0.1045
7	----	7	0.2315	0.2344	-----
8	----	8	0.2401	0.2519	-----
9	----	9	0.2457	0.2640	-----
10	-0.9925	-----	-----	-----	-----
11	0.4513	-----	-----	-----	-----
12	1.2585	-----	-----	-----	-----

7.2.2 Dam-Break Propagation over Sewage Pipe with Blocks Interaction

The final test case models an urban flooding situation over an idealised city with under ground pipe network propagation. A similar test case with just the blocks has been proposed in [76]. The numerical domain and initial condition for this test case is displayed in Figure 7.6. As was demonstrated here the number of pipes and nodes are set the same as the test case defined in Figure 7.2. The only difference is that here we have considered a square (2m×2m) block with 0.6m height in the middle of each rectangular network to represent some blockage scenarios during the flooding. In addition the orifice diameter for the sewage manholes was chosen equal to 0.4m. Obviously the test case is difficult because it includes the interaction between the free-surface flow and the solid structures along with the sewage efflux propagation. The solid blocks have been considered as the source terms in the momentum equation for the two-dimensional shallow water solver.
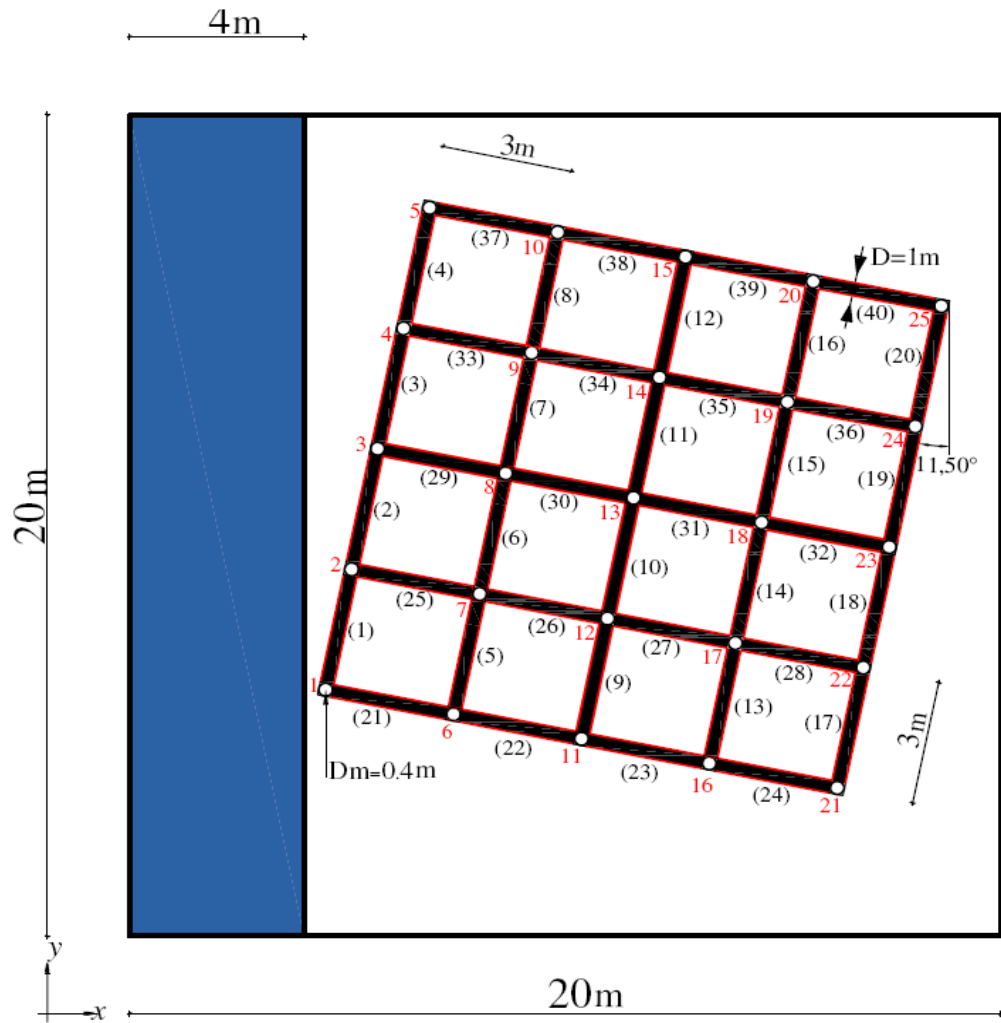
**Figure 7.4. The initial problem for the dam-break over underground pipe networks with 40 pipe and 25 nodes.**
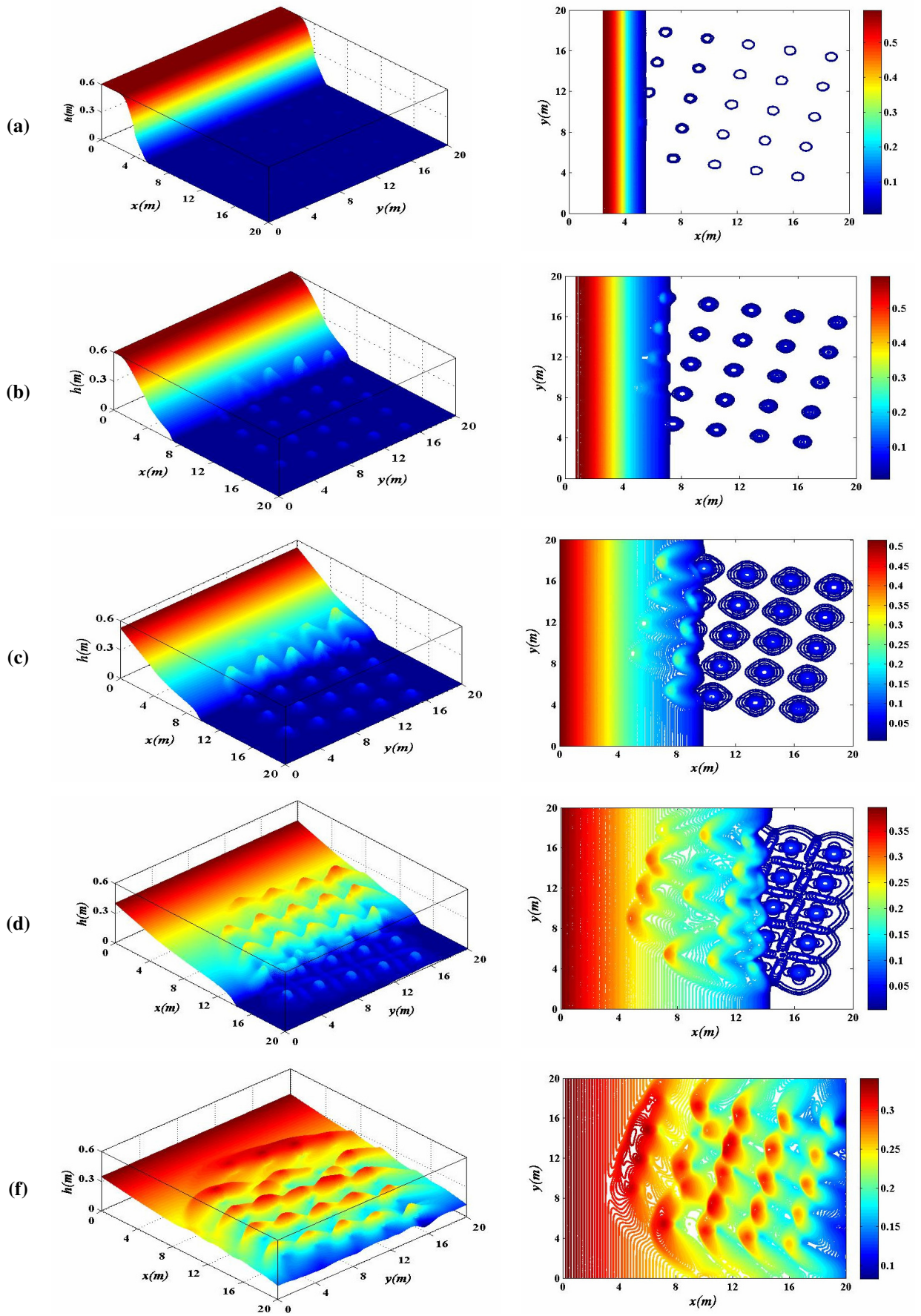
Figure 7.5. The dam-break propagation over sewage pipe network defined in Figure 7.3 for time *t*=0.4, 1, 2, 4 and 8s (a-f). Colours blue to red correspond to the water depth 0-0.6m.

Figure 7.7 exhibits 3-D plots and top plan views for the dam propagation over an idealised city shown in Figure 7.6. Tables 7.5-7.9 also provide underground analysis for the current sewage pipe network. By time t=0.4s the wet/dry fronts reach to first sewage manholes and causes the efflux outflows over the city crossroads from downstream nodes. As can be seen in Table 7.5 the discharge for the lateral pipes (3, 4, 5 and 6) become nearly zero and only flood water is flowing into the vertical pipes. At time t=1s the flood waves collide with the first two blocks and start to rise behind them and the resulting bores propagate downstream. Meanwhile, the sewage outflows spread into both longitudinal and vertical directions between the blocks. Additionally, the dam-break flow completely passes the first solid blocks and move into the first intersection. The same behaviour for the discharge is also observed in Table 7.6 and still no discharge is flowing in the lateral pipes.

By time t=2s complex interactions between the flows from either the underground efflux waves and wet/dry fronts occurred in the first crossroads. Moreover, the efflux discharges are fully involved into the flooding. At time t=4s the city intersections are partially filled by water and the final sewage efflux outflows also mixed into the inundation and the flood waves move toward the right boundary. Furthermore, the flood is flowing in both lateral and vertical sewage pipes (5, 6, 10, 11, 12) as was demonstrated in Table 7.8. At time t=8s the city is completely inundated and the reflected water waves hit earlier with the right boundary, move toward the upstream. Again the continuity conditions for the junctions at different times can be queried from the tables. Note that the meaning for the negative discharge in these tables is the water flow in the opposite direction of the initial assumption (red arrows in Figure 7.6b). The number of computational grid cells and the CFL number were chosen equal to 1024×1024 and 0.12 respectively. For the underground analysis the orifice coefficient for the sewage manholes was selected to 0.55.

7.3 Conclusions

In this Chapter we have provided the numerical results for the flood propagation over a complex sewage pipe network. A new and novel underground pipe network solver was also presented and coupled with two-dimensional shallow water solver to exactly compute the amount of efflux discharge from underground pipe network during the inundation. In fact the shallow water solver combines the explicit flux wave (f-wave) approach with the implicit underground pipe network solver to simulate the flood propagation over cities with sewage systems. It is also inferred that the two-dimensional shallow water scheme with a

(a)
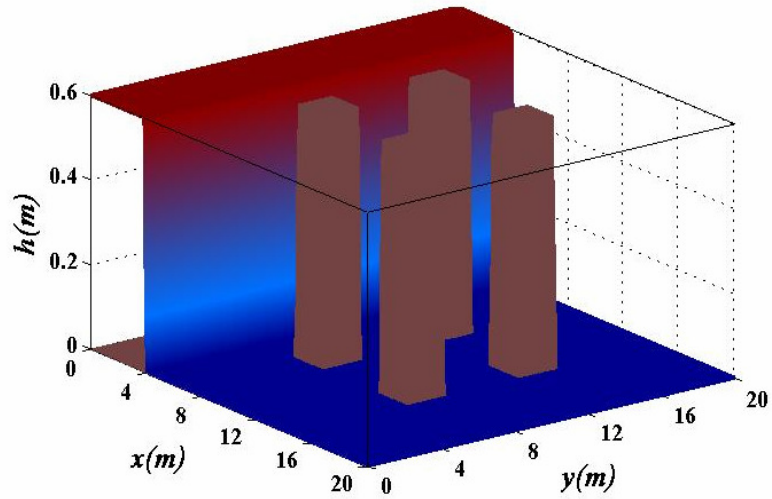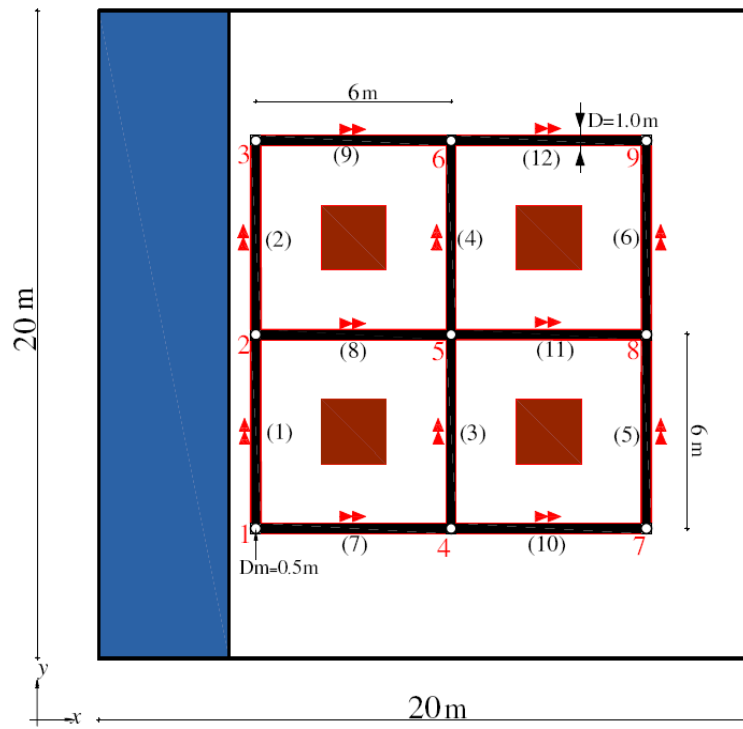
(b)

Figure 7.6. The initial problem for the dam-break propagation over an idealised city with the sewage efflux discharges. (a): Underground view, (b): Over ground view.
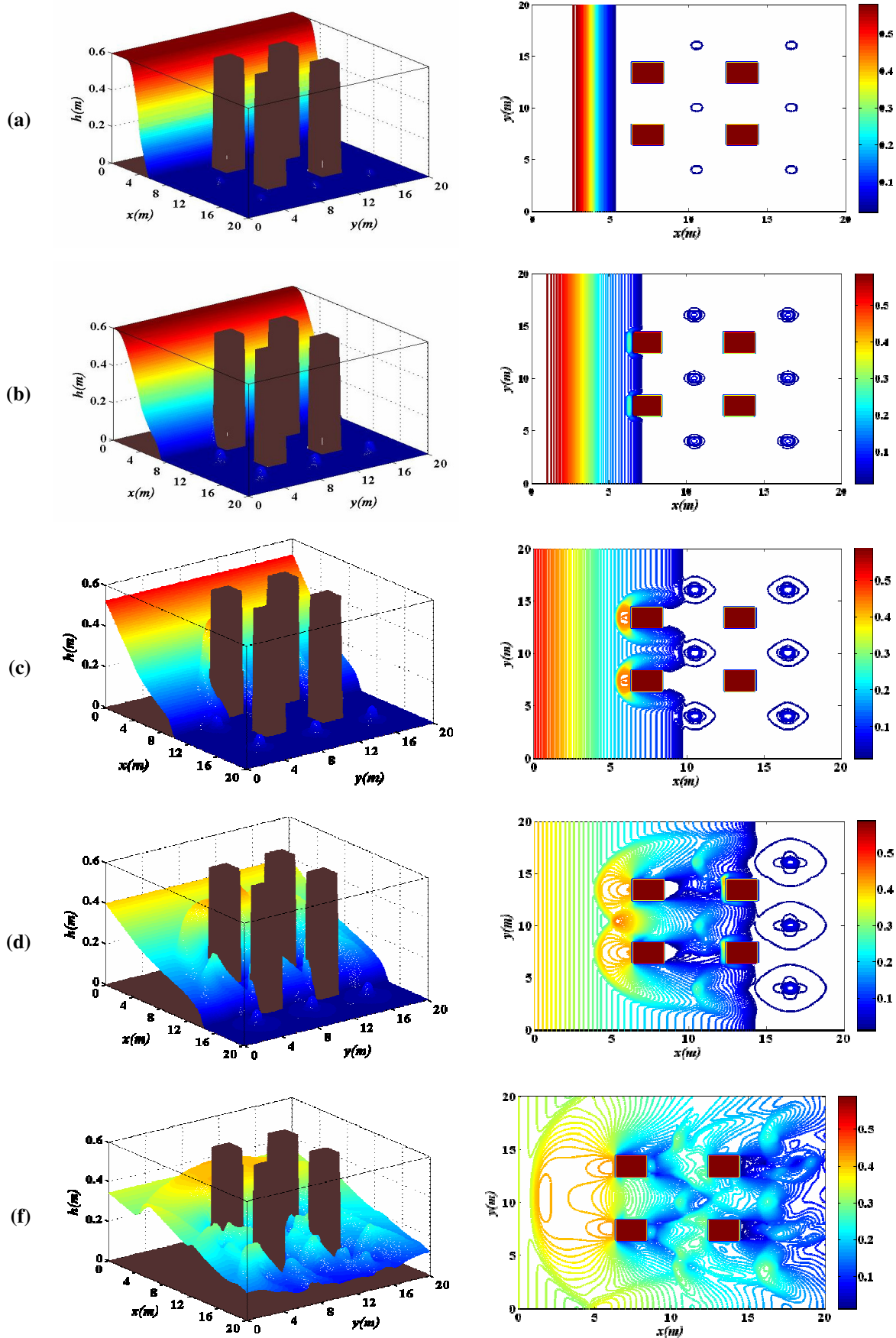
Figure 7.7. The dam-break propagation over sewage pipe network with block interactions for time *t*=0.4, 1, 2, 4 and 8s (a-f). Left column: 3-D plots. Right column: Top view plans.

155

Table 7.5. Pipe discharges, nodal heads and the efflux discharge for dam-break propagation over sewage pipe with block interactions at *t*=0.4s.

Pipe Number	$Q(m^3/s)$	Node Number	Efflux Discharge	HGL(m)	Ht(m)
1	-----	1	----	----	0.1114
2	-----	2	-----	-----	0.1114
3	3.79×10^{-8}	3	-----	-----	0.1114
4	3.57×10^{-8}	4	0.1004	0.1076	-----
5	4.25×10^{-8}	5	0.1004	0.1076	-----
6	4×10^{-8}	6	0.1004	0.1076	-----
7	0.2007	7	0.1003	0.1075	-----
8	0.2007	8	0.1003	0.1075	-----
9	0.2007	9	0.1003	0.1075	-----
10	0.1003	-----	-----	-----	-----
11	0.1003	-----	-----	-----	-----
12	0.1003	-----	-----	-----	-----

Table 7.6. Pipe discharges, nodal heads and the efflux discharge for dam-break propagation over sewage pipe with block interactions at time *t*=1s.

Pipe Number	$Q(m^3/s)$	Node Number	Efflux Discharge	HGL(m)	Ht(m)
1	----	1	----	----	0.1845
2	----	2	----	----	0.1845
3	4.6000	3	----	----	0.1845
4	4.6000	4	0.1292	0.1781	-----
5	-1.2×10^{-8}	5	0.1292	0.1781	-----
6	1.1×10^{-8}	6	0.1292	0.1781	-----
7	1.3×10^{-8}	7	0.1291	0.1779	-----
8	1.1×10^{-8}	8	0.1291	0.1779	-----
9	0.2583	9	0.1291	0.1779	-----
10	0.2583	-----	-----	-----	-----
11	0.2583	-----	-----	-----	-----
12	0.1291	-----	-----	-----	-----

Table 7.7. Pipe discharges, nodal heads and the efflux discharge for dam-break propagation over sewage pipe with block interactions at time at time *t*=2s.

Pipe Number	$Q(m^3/s)$	Node Number	Efflux Discharge	HGL(m)	Ht(m)
1	----	1	----	----	0.2257
2	----	2	----	----	0.2257
3	-4.9×10^{-9}	3	-----	-----	0.2257
4	-4.5×10^{-9}	4	0.1429	0.2179	-----
5	5.4×10^{-9}	5	0.1429	0.2179	-----
6	5.4×10^{-8}	6	0.1429	0.2179	-----
7	0.2857	7	0.1428	0.2177	-----
8	0.2857	8	0.1428	0.2177	-----
9	0.2857	9	0.1428	0.2177	-----
10	0.1428	-----	-----	-----	-----
11	0.1428	-----	-----	-----	-----
12	0.1428	-----	-----	-----	-----

Table 7.8. Pipe discharges, nodal heads and the efflux discharge for the sewage network defined in Figure 7.2 at time *t*=4s.

Pipe Number	$Q(m^3/s)$	Node Number	Efflux Discharge	HGL(m)	Ht(m)
1	----	1	----	----	0.2537
2	----	2	----	----	0.2607
3	-----	3	-----	-----	0.2599
4	----	4	----	-----	0.2161
5	0.4331	5	----	-----	0.2231
6	-0.2611	6	-----	-----	0.2154
7	----	7	0.1633	0.2848	-----
8	----	8	0.1627	0.2826	-----
9	-----	9	0.1625	0.2818	-----
10	0.5964	-----	-----	-----	-----
11	-0.5314	-----	-----	-----	-----
12	0.4235	-----	-----	-----	-----

new choice of wave speed can model multiple interaction with either the structures or efflux propagations over the dry-state.

Chapter 8 : CONCLUSIONS AND RECOMMENDATIONS

This Chapter provides a summary of this thesis and possible directions for future work.

8.1 General Conclusion

In this thesis a modified depth-averaged SWEs based on the wave propagation algorithm has been employed for the inundation problems over the dry urban areas with efflux discharge propagation. A novel and simple Riemann solver based on the new choice of wave speed has been also defined. The proposed Riemann solver utilises the advantages of both approximate and exact Riemann speeds to overcome the drawbacks for the flux-wave (f-wave) approach defined by Bale *et al.* in [6]. In fact, this modified Riemann solver is equivalent to Roe's approximate solver in the case of wet-state and for the nearly dry or dry states problems it uses the combination of exact Riemann speed and Einfeldt speeds defined in [20] for the HLLE Riemann solver. The solver is well-balanced and accurately balances the flux-gradients and source terms for the stationary or steady-state shallow water problems where the fluid discharge should be constant. Additionally, the proposed scheme is depth-positive and it accurately preserves depth positivity for the propagation of wet/dry fronts and can model complex bore interactions over nearly dry or dry-state areas. For the inhomogeneous SWEs the solver employs the inherent property of the f-wave approach and treats the source terms within the flux differencing of the neighbouring cells for the finite volume methods.

The conventional SWEs have been also modified by adding a new type of source term into the continuity equation to consider the effect of efflux/influx terms. This type of source term is completely new and has not been considered by other researchers for the depth-averaged SWEs based on the author's knowledge. These source terms provide some new properties for the SWEs and enable the scheme to consider the effect of sources or sinks during the inundation for some specific efflux number (En) as has been defined in Chapter 3. This efflux number determines the effect of non-hydrostatic pressure distribution for efflux/influx propagation within the solution. To investigate the effect of the efflux term for the SWEs, we have validated our shallow water results with the STAR-CD solver which is a commercial Navier-Stokes solver and predicts free-surface motions. The

comparisons between the SWEs and the STAR-CD verify that the proposed shallow water model gives reasonable predictions for all times provided $En \leq 0.5$ and for long duration for $En \geq 0.5$.

The one-dimensional shallow water model defined in Chapter 3 has been extended and developed for two-dimensional problems in Chapter 5. For the two-dimensional SWEs we have utilised the direction-splitting approach based on the wave propagation algorithm defined in [45, 47] which solves each Riemann problem in each direction. The effect of missing cross-derivative terms has been added into the shallow water solver by solving another Riemann problem in the orthogonal direction. Again for two-dimensional problems the efflux discharge results have been compared with the STAR-CD solver and the same behaviour for the efflux number was observed for two-dimensional problems.

The shallow water scheme has been generalised to more realistic flood situations by modelling the flood propagation over underground pipe network with multiple efflux and structure interactions. In contrast to the one-dimensional problems the calculation of the efflux discharge for the underground sewage systems is a sophisticated task. To cope with this problem a novel underground solver which computes the efflux discharge has been developed. As the free-surface flow passes through the underground sewage ports, the solver takes the water elevation over the sewage manhole and creates different sets of equations for the head loss difference within the pipes and hydraulic grades lines for the nodes. These sets of equations are then solved by the non-linear Newton method which gives the amount of efflux discharge for the downstream nodes. In summary therefore, for the inundation problems over sewage pipe systems our solver utilises a new version of explicit Godunov-type method which predicts the water elevation during the inundation and an implicit underground solver which determines the efflux velocities for the sewage manholes.

8.2 Detailed Conclusions

8.2.1 Shallow Water Solver

The wave propagation algorithm defined by LeVeque [44, 45] for hyperbolic systems has been developed in this thesis. The method is a Godunov-type scheme and can be used for the conservative and non-conservative hyperbolic systems. The scheme also employs the

159

second-order accurate terms for the smooth solution and meets the necessary conditions to achieve discontinuous weak solutions. As mentioned in the previous Section a new choice of wave speed has been defined to treat the difficulties for the propagation over dry states. For obtaining high-resolution solutions and second-order accuracy we have used Monotonised centre (MC) and van Leer limiters for all of one-dimensional and two-dimensional results provided in this thesis. Moreover, a modified Harten entropy fix conditions defined in [33] has been implemented to avoid non-physical solutions. Proper choice of boundary conditions has been performed within the numerical results presented in this thesis. To model the open boundary conditions the zero-order extrapolation boundary conditions was performed. The wall boundary conditions have been modelled by reflecting interior data across the boundary.

The numerical model proposed for the one-dimensional and two-dimensional SWEs has been validated extensively for the homogenous and inhomogeneous shallow water problems within this thesis. In this Section we only provide a brief summary for the standard shallow water benchmarks. In Chapter 4, the validity of the proposed scheme has been examined in part I by comparing with analytical solutions for several one-dimensional benchmarks. First the suitability of the scheme in dealing with two strong rarefaction appeared in the nearly dry-state and completely dry-state has been validated with the analytical solution. Then, the steady flow conditions over the hump have been examined for the case of subcritical and transcritical with or without a shock. For all of the steady-state cases the proposed scheme provided very close agreement with the theoretical discharge which verifies that our solver can balance the source terms and flux-gradient terms for the stationary flow. The next test case considered in part I, investigates the vacuum state over the step and examines the reliability of the method to deal with strong rarefactions over the discontinuous topography. The results prove that our second-order shallow water solver gives nearly identical results to the Reference solution given in [10].

The two-dimensional standard shallow water results have been validated in Chapter 6. In this Chapter, first the rectangular dam-break problem has been propagated over the wet and dry states. A close agreement has been achieved between our solver and the alternative approaches provided in the literature (see e.g. [47, 85]). The second case presented in this Chapter comprises the dam propagation over wet-state. In this test case the scheme employs the Roe's approximate wave speed to evaluate free-surface propagation through

the wall. The final test case provided in the first part of Chapter 6 concerns the dam-propagation over dry-state with complex bed topography and examines the reliability of a two-dimensional scheme with complex bathymetric variations. Again very close agreement is obtained between our solver and other shallow water schemes presented in the literature (see [17, 52] for more details).

8.2.2 Navier-Stokes Solver and Shallow Water Results with Efflux Terms

As mentioned in Section 8.1 the shallow water results with the efflux/influx source terms have been compared with the STAR-CD solver which solves 3-D Navier-Stokes equations based on the SIMPLE finite volume algorithm. To capture the free-surface level the solver employs the Volume of Fluid (VOF) approach which gives different levels for the free-surface flow. The one-dimensional comparisons between the shallow water scheme with the efflux/influx source terms and the STAR-CD solver have been presented in Chapter 4. For the dam-break propagation over dry-state very close agreement have been obtained between the SWEs with friction terms and the VOF scheme. For the efflux test case over the dry-state nearly identical results have been achieved with the VOF scheme for the $En \leq 0.5$. For the higher efflux number it was shown that the front bores were well predicted with both the shallow water solver and the VOF scheme. For the efflux propagation over the wet-state approximately the same behaviour is observed between two methods but the VOF scheme gives smoother results for the front propagation and shocks. For the dam-break over dry- state with efflux propagation again a very good agreement is observed.

Results for the two-dimensional SWEs with the efflux terms have been investigated in Chapter 6 part II. First the two-dimensional shallow water scheme has been used to model the two-dimensional efflux problem over the dry-state and again the numerical results have been compared with 3-D Navier-Stokes solver (STAR-CD) for different efflux velocities. As shown in Chapter 6 nearly similar results have been obtained for both shallow water and VOF schemes. The final efflux test case presented in this Chapter investigated the interaction between dam propagation with two-dimensional efflux discharge. Again the agreement between SWEs and VOF scheme is good (for the lower efflux number). Note that for all Navier-Stokes test cases compared with the two-dimensional SWEs in this thesis the $(k - \varepsilon)$ turbulence modelling has been used; however, no oblivious

discrepancies between laminar and turbulent flow is observed and the laminar assumptions should provide the same results for the free-surface flow. The final efflux test cases in this thesis were presented in Chapter 7 for more realistic flooding problems in two dimensions. The first two cases model dam propagation over the underground pipe networks which includes complex interactions between different efflux discharge and dam flow. As mentioned in Section 8.1 the efflux discharge for the sewage manholes has been computed based on the underground pipe network solver which fully explained in Chapter 7 and briefly described in Section 8.1. The final test case simulates the flooding over sewage pipe networks with some blockage scenarios and demonstrates that the proposed two-dimensional shallow water solver can model the multiple efflux interaction with structures over the dry-state.

8.3 Recommendation for Future Work

8.3.1 Development in Riemann Solver Based on the F-Wave Approach

In this work we have presented a modified version for the flux-wave (f-wave) approach for the SWEs which can simulate different flow regime with bathymetry deviations and efflux/influx terms for the continuity equations. The presented Riemann solver is suitable for any shallow water flow in particular for the steady-state problems. However, a further improvement would be to avoid completely using epsilon, ε, (the depth below which the exact Riemann solver should be used) for the nearly dry-state problems.

8.3.2 Adaptive Mesh Refinement for the Wave Propagation Algorithm

In the numerical results presented in this work we have only employed the structured hierarchies for the finite volume methods. However, the integral conservation laws and the finite volume methods can be applied for any grid cell. For the modified f-wave approach described in this thesis the adaptive refinement methods can be performed to localise the fined grids for different part of computational domain. The *Berger-Collela-Oliger* approach defined in [8, 7] and can be implemented in the modified wave propagation algorithm defined in this thesis. These methods were originally proposed for the Euler-equations and shock tube problems with very sharp gradient. In these methods several levels of Cartesian subgrids can be created in space and time. It is hoped that the local refinement can provide very neat results for the wave propagation algorithm with efflux discharge in particular around the sewage manholes.

8.3.3 Improvement for the Underground Pipe Network Solver

(i). For the underground pipe network solver presented in Chapter 7 the random initial guess at each time step has been chosen for the system of HGL equations and the discharge within the pipe for the non-linear Newton solver. It is thought that the initial guess for the non-linear solution can be hydraulically rectified by using main stream approaches defined [71, 83] for the underground pipe network analysis. These approaches can significantly reduce the number of iterations for the Newton method and enable the solver to deal with thousands of underground pipes.

(ii). The pipe network is considered to be always full but it can be generalised for the partially full pipes. For the partially full pipe network the influx discharge first needs to be computed through the ports until the pipe network become full. Then, the underground pipe network solver explained in Chapter 7 can be applied to calculate the efflux discharges through the ports.

(iii). As mentioned in Chapter 7 for the underground pipe network solver only the effect of friction terms have been considered into the solutions. However, the effect of junction losses, debris and pressure vales can be included as an additional velocity heads into the Bernoulli's equation.

8.3.4 Comparisons with Experimental Data

This thesis has focused on the theoretical improvement of the Riemann solver based on f-wave approach with the new choice of efflux source terms. We have also defined a robust underground pipe solver for the flood propagation over the sewage network. As mentioned in Chapter 1 no experimental comparisons has been performed within this PhD work and it is hoped that some numerical results presented in this thesis (in particular dam propagation over the underground pipe network) are validated with proper experimental data in future.

Bibliography

1. Aguirre-Pe J, Quisca S, Plachco FP**.** Tests and Numerical One-Dimensional Modeling of a High-Viscosity Fluid Dam-Break Wave. *Journal of Hydraulic Research* 1995; **33**(1): 17-26.

2. Akan AO. *Open Channel Hydraulics.* Elsevier: Oxford, 2006.

3. Alcrudo F, García-Navarro P**.** A High-Resolution Godunov-Type Scheme in Finite Volumes for the 2d Shallow-Water Equations. *International Journal for Numerical Methods in Fluids* 1993; **16**(6): 489-505.

4. Alcrudo F, Benkhaldoun F**.** Exact Solutions to the Riemann Problem of the Shallow Water Equations with a Bottom Step. *Computers & Fluids* 2001; **30**(6): 643-671.

5. Audusse E, Bouchut F, Bristeau MO, Klein R, Perthame B**.** A Fast and Stable Well-Balanced Scheme with Hydrostatic Reconstruction for Shallow Water Flows. *SIAM Journal on Scientific Computing* 2004; **25**(6): 2050-2065.

6. Bale DS, LeVeque RJ, Mitran S, Rossmanith JA**.** A Wave Propagation Method for Conservation Laws and Balance Laws with Spatially Varying Flux Functions. *SIAM Journal on Scientific Computing* 2002; **24**(3): 955-978.

7. Berger MJ, Oliger J**.** Adaptive Mesh Refinement for Hyperbolic Partial-Differential Equations. *Journal of Computational Physics* 1984; **53**(3): 484-512.

8. Berger MJ, Colella P**.** Local Adaptive Mesh Refinement for Shock Hydrodynamics. *Journal of Computational Physics* 1989; **82**(1): 64-84.

9. Bernetti R, Titarev VA, Toro EF**.** Exact Solution of the Riemann Problem for the Shallow Water Equations with Discontinuous Bottom Geometry. *Journal of Computational Physics* 2008; **227**(6): 3212-3243.

10. Bouchut F, *Nonlinear Stability of Finite Volume Methods for Hyperbolic Conservation Laws and Well-Balanced Schemes for Sources*. 2004, Birkhäuse Verlag.

11. Brufau P, Vázquez-Cendón ME, García-Navarro P**.** A Numerical Model for the Flooding and Drying of Irregular Domains. *International Journal for Numerical Methods in Fluids* 2002; **39**(3): 247-275.

12. Casulli V**.** Semi-Implicit Finite-Difference Methods for the 2-Dimensional Shallow-Water Equations. *Journal of Computational Physics* 1990; **86**(1): 56-74.

13. Casulli V, Cheng RT**.** Semi-Implicit Finite-Difference Methods for 3-Dimensional Shallow-Water Flow. *International Journal for Numerical Methods in Fluids* 1992; **15**(6): 629-648.

14. Clough RW. *The Finite Element Method in Plane Stress Analysis;* Second ASCE Conference. 1960. Pittsburg.

15. Courant R, Friedrichs KO, H.Lewy**.** Uber Die Partiellen Differenzeengleichungen Der Mathematischen Physik. *Mass.Ann.* 1928; **100**: 32-74.

16. Delis AI**.** Improved Application of the Hlle Riemann Solver for the Shallow Water Equations with Source Terms. *Communications in Numerical Methods in Engineering* 2003; **19**(1): 59-83.

17. Delis AI, Kazolea M, Kampanis NA**.** A Robust High-Resolution Finite Volume Scheme for the Simulation of Long Waves over Complex Domains. *International Journal for Numerical Methods in Fluids* 2008; **56**(4): 419-452.

18. Djordjevic′ S, Prodanovic′ D, Maksimovic′ C, Ivetic′ M, Savic′ D**.** Sipson - Simulation of Interaction between Pipe Flow and Surface Overland Flow in Networks. *Water Science and Technology* 2005; **52**(5): 275-283.

19. Dubois F, Mehlman G**.** A Non-Parameterized Entropy Correction for Roe's Approximate Riemann Solver. *Numerische Mathematik* 1996; **73**(2): 169-208.

20. Einfeldt B**.** On Godunov-Type Methods for Gas-Dynamics. *SIAM Journal on Numerical Analysis* 1988; **25**(2): 294-318.

21. Einfeldt B, Munz CD, Roe PL, Sjogreen B**.** On Godunov-Type Methods for near Low Densities. *Journal of Computational Physics* 1991; **92**: 273-295.

22. Fennema RJ, Chaudhry MH**.** Simulation of One-Dimensional Dam-Break Flows. *Journal of Hydraulic Research* 1987; **25**(1): 41-51.

23. Gallegos HA, Schubert JE, Sanders BF**.** Two-Dimensional, High-Resolution Modeling of Urban Dam-Break Flooding: A Case Study of Baldwin Hills, California. *Advances in Water Resources* 2009; **32**(8): 1323-1335.

24. Gallouët T, Hérard JM, Seguin N**.** Some Approximate Godunov Schemes to Compute Shallow-Water Equations with Topography. *Computers & Fluids* 2003; **32**(4): 479-513.

25. García-Navarro P, Vázquez-Cendón ME**.** On Numerical Treatment of the Source Terms in the Shallow Water Equations. *Computers & Fluids* 2000; **29**(8): 951-979.

26. George DL, Finite Volume Methods and Adaptive Refinement for Tsunami Propagation and Inundation. *PhD thesis*, University of Washington, 2006.

27. George DL**.** Augmented Riemann Solvers for the Shallow Water Equations over Variable Topography with Steady States and Inundation. *Journal of Computational Physics* 2008; **227**(6): 3089-3113.

28. Godunov SK**.** A Difference Method for Numerical Calculation of Discontinuous Solutions of the Equations of Hydrodynamics. *Matematicheskii Sbornik* 1959; **47**: 271-306.

29. Goutal N, Maurel F**.** *In Proceedings of the 2nd Workshop on Dam-Break Wave Simulation.*Départment Laboratoire National d'Hydraulic, Groupe Hydraulic Fluviale Electricité de Fracne, France. 1997.

30. Harten A. High-Resolution Schemes for Hyperbolic Conservation-Laws. *Journal of Computational Physics* 1983; **49**(3): 357-393.

31. Harten A. ENO Schemes with Subcell Resolution. *Journal of Computational Physics* 1989; **83**(1): 148-184.

32. Harten A, Hyman JM. Self-Adjusting Grid Methods for One-Dimensional Hyperbolic Conservation-Laws. *Journal of Computational Physics* 1983; **50**(2): 235-269.

33. Harten A, Lax PD, Leer Bv. On Upstream Differencing and Godunov-Type Schemes for Hyperbolic Conservation-Laws. *SIAM Review* 1983; **25**(1): 35-61.

34. Harten A, Engquist B, Osher S, Chakravarthy SR. Uniformly High-Order Accurate Essentially Nonoscillatory Schemes. III. *Journal of Computational Physics* 1987; **71**(2): 231-303.

35. Henderson F. *Open Channel Hydraulics.* McGraw Hill: New York, 1966.

36. Hubbard ME, García-Navarro P. Flux Difference Splitting and the Balancing of Source Terms and Flux Gradients. *Journal of Computational Physics* 2000; **165**(1): 89-125.

37. Kawahara M, Umetsu T. Finite-Element Method for Moving Boundary-Problems in River Flow. *International Journal for Numerical Methods in Fluids* 1986; **6**(6): 365-386.

38. Kawahara M, Takeuchi N, Yoshida T. Two Step Explicit Finite Element Method for Tsunami Wave Propagation Analysis. *International Journal for Numerical Methods in Engineering* 1978; **12**(2): 331-351.

39. Kawahara M, Hirano H, Tsubota K, Inagaki K. Selective Lumping Finite-Element Method for Shallow-Water Flow. *International Journal for Numerical Methods in Fluids* 1982; **2**(1): 89-112.

40. Larock BE, Jeppson RW, Watters GZ. *Hydraulics of Pipeline Systems.* CRC Press: New York, 1999.

41. Lax P, Wendroff B. Systems of Conservation Laws. *Communications on Pure and Applied Mathematics* 1960; **13**(2): 217-237.

42. Leer Bv. Towards the Ultimate Conservative Difference Scheme I. The Quest of Monotonicity. *Springer Lecture Notes in Physics* 1973; **18**: 163-168.

43. LeVeque RJ. High-Resolution Finite Volume Methods on Arbitrary Grids Via Wave-Propagation. *Journal of Computational Physics* 1988; **78**(1): 36-63.

44. LeVeque RJ. *Numerical Methods for Conservation Laws.* Birkhauser: 1990.

45. LeVeque RJ. Wave Propagation Algorithms for Multidimensional Hyperbolic Systems. *Journal of Computational Physics* 1997; **131**(2): 327-353.

46. LeVeque RJ. Balancing Source Terms and Flux Gradients in High-Resolution Godunov Methods: The Quasi-Steady Wave-Propagation Algorithm. *Journal of Computational Physics* 1998; **146**(1): 346-365.

47. LeVeque RJ. *Finite Volume Methods for Hyperbolic Problems.* Cambridge University Press: 2002.

48. LeVeque RJ, Pelanti M. A Class of Approximate Riemann Solvers and Their Relation to Relaxation Schemes. *Journal of Computational Physics* 2001; **172**(2): 572-591.

49. LeVeque RJ, George DL. *High-Resolution Finite Volume Methods for the Shallow Water Equations with Bathymetry and Dry States* third international workshop on long-wave runup models. 2004. Catalina.

50. LeVeque RJ, George DL. High-Resolution Finite Volume Methods for the Shallow Water Equations with Bathymetry and Dry States. *Advanced Numerical Models for Simulating Tsunami Waves and Runup* 2008; **10**: 43-73.

51. Liang QH, Borthwick AGL. Adaptive Quadtree Simulation of Shallow Flows with Wet-Dry Fronts over Complex Topography. *Computers & Fluids* 2008; **38**(2): 221-234.

52. Liang QH, Marche F. Numerical Resolution of Well-Balanced Shallow Water Equations with Complex Source Terms. *Advances in Water Resources* 2009; **32**(6): 873-884.

53. Liu PLF, Cho YS, Briggs M, Kanoglu U, Synolakis C. Runup of Solitary Waves on a Circular Island. *Journal of Fluid Mechanics* 1995; **302**: 259–285.

54. Liu PLF, Cho YS. Integral-Equation Model for Wave-Propagation with Bottom Frictions. *Journal of Waterway Port Coastal and Ocean Engineering-ASCE* 1994; **120**(6): 594-608.

55. Liu PLF, Cho YS, Briggs MJ, Kanoglu U, Synolakis CE. Runup of Solitary Waves on a Circular Island. *Journal of Fluid Mechanics* 1995; **302**: 259-285.

56. Ma DJ, Sun DJ, Yin XY. Solution of the 2-D Shallow Water Equations with Source Terms in Surface Elevation Splitting Form. *International Journal for Numerical Methods in Fluids* 2007; **55**: 431-454.

57. MacCormack RW. The Effect of Viscosity in Hypervelocity Impact Cratering (Reprinted from Alaa Paper 69-354, 1969). *Journal of Spacecraft and Rockets* 2003; **40**(5): 757-763.

58. MacDonald PW. The Computation of Transonic Flow through Two-Dimensional Gas Turbine Cascades. *ASME* 1971: Paper-GT-89

59. Mahdizadeh H, Stansby PK, Rogers BD. Modeling of Flood Waves over Underground Pipe Networks Based on a Two-Dimensional Wave Propagation

Algorithm Coupled to a Pipe Network Solver. *Submitted to Journal of Hydraulic Engineering-ASCE* 2010;

60.   Mahdizadeh H, Stansby PK, Rogers BD**.** On the Approximation of Local Efflux/Influx Bed Discharge in the Shallow Water Equations Based on a Wave Propagation Algorithm. *International Journal for Numerical Methods in Fluids* 2010; **DOI: 10.1002/fld.2314**

61.   Mahdizadeh H, Rogers BD, Stansby PK. *Flood Modelling with Underground Pipe Networks Using Local Efflux/Influx Bed Discharge in the 2-D Shallow Water Equations.*The First European IAHR Congress. 2010. Edinburgh .

62.   Marshall G, Méndéz R**.** Computational Aspects of the Random Choice Method for Shallow-Water Equations. *Journal of Computational Physics* 1981; **39**(1): 1-21.

63.   Morandi-Cecchi M, Venturin M**.** Characteristic-Based Split (CBS) Algorithm Finite Element Modelling for Shallow Waters in the Venice Lagoon. *International Journal for Numerical Methods in Engineering* 2006; **66**(10): 1641-1657.

64.   Nania LS, Goméz M, Dolz J**.** Experimental Study of the Dividing Flow in Steep Street Crossings. *Journal of Hydraulic Research* 2004; **42**(4): 406-412.

65.   Osher S**.** Convergence of Generalized MUSCL Schemes. *SIAM Journal on Numerical Analysis* 1985; **22**(5): 947-961.

66.   Press WH, Teukolsky SA, Vetterling WT, Flannery BP. *Numerical Recipes in Fortran 77 Second Edition.* Cambridge University Press: 1992.

67.   Roe PL**.** Approximate Riemann Solvers, Parameter Vectors, and Difference-Schemes. *Journal of Computational Physics* 1981; **43**(2): 357-372.

68.   Roe PL**.** Approximate Riemann Solvers, Parameter Vectors, and Difference Schemes (Reprinted from the Journal of Computational Physics, Vol 43, Pg 357-372, 1981). *Journal of Computational Physics* 1997; **135**(2): 250-258.

69.   Rogers BD, Fujihara M, Borthwick AGL**.** Adaptive Q-Tree Godunov-Type Scheme for Shallow Water Equations. *International Journal for Numerical Methods in Fluids* 2001; **35**(3): 247-280.

70.   Rogers BD, Borthwick AGL, Taylor PH**.** Mathematical Balancing of Flux Gradient and Source Terms Prior to Using Roe's Approximate Riemann Solver. *Journal of Computational Physics* 2003; **192**(2): 422-451.

71.   Salgado R, Todini E, O'Connell PE**.** Comparison of the Gradient Method with Some Traditional Methods for the Analysisof Water Supply Distribution Networks. *Computer applications in water supply* 1988; **1**: 38-62.

72.   Schubert JE, Sanders BF, Smith MJ, Wright NG**.** Unstructured Mesh Generation and Landcover-Based Resistance for Hydrodynamic Modeling of Urban Flooding. *Advances in Water Resources* 2008; **31**(12): 1603-1621.

73. Shabayek S, Steffler P, Hicks F. Dynamic Model for Subcritical Combining Flows in Channel Junctions. *Journal of Hydraulic Engineering-ASCE* 2002; **128**(9): 821-828.

74. Soares-Frazão S, Zech Y. Dam Break in Channels with 90 Degrees Bend. *Journal of Hydraulic Engineering-ASCE* 2002; **128**(11): 956-968.

75. Soares-Frazão S, Zech Y. Experimental Study of Dam-Break Flow against an Isolated Obstacle. *Journal of Hydraulic Research* 2007; **45**: 27-36.

76. Soares-Frazão S, Zech Y. Dam-Break Flow through an Idealised City. *Journal of Hydraulic Research* 2008; **46 (5)**: 648-658.

77. Stansby PK. Limitations of Depth-Averaged Modeling for Shallow Wakes. *Journal of Hydraulic Engineering-ASCE* 2006; **132**(7): 737-740.

78. Stansby PK, Chegini A, Barnes TCD. The Initial Stages of Dam-Break Flow. *Journal of Fluid Mechanics* 1998; **374**: 407-424.

79. Swamee PK, Jain AK. Explicit Equations for Pipe-Flow Problems. *Journal of the Hydraulics Division-ASCE* 1976; **102**(5): 657-664.

80. Sweby PK. High-Resolution Schemes Using Flux Limiters for Hyperbolic Conservation-Laws. *SIAM Journal on Numerical Analysis* 1984; **21**(5): 995-1011.

81. Titov VV, Synolakis CE. Modeling of Breaking and Nonbreaking Long-Wave Evolution and Runup Using Vtcs-2. *Journal of Waterway Port Coastal and Ocean Engineering-ASCE* 1995; **121**(6): 308-316.

82. Titov VV, Synolakis CE. Numerical Modeling of Tidal Wave Runup. *Journal of Waterway Port Coastal and Ocean Engineering-ASCE* 1998; **124**(4): 157-171.

83. Todini E, Pilati S. A Gradient Algorithm for the Analysis of Pipe Networks. *Computer Applications in Water Supply* 1988; **1**: 1-20.

84. Toro EF. *Riemann Solvers and Numerical Methods for Fluid Dynamics.* Springer: Tokyo, 1997.

85. Toro EF. *Shock Capturing Methods for Free Surface Shallow Flows.* John Wiley & Sons: United Kingdom, 2001.

86. Vázquez-Cendón ME. Improved Treatment of Source Terms in Upwind Schemes for the Shallow Water Equations in Channels with Irregular Geometry. *Journal of Computational Physics* 1999; **148**: 497–526.

87. VonNeumann J, Richtmyer RD. A Method for the Numerical Calculation of Hydrodynamic Shocks. *Journal of Applied Physics* 1950; **21**(3): 232-243.

88. Wu YY, Cheung KF. Explicit Solution to the Exact Riemann Problem and Application in Nonlinear Shallow-Water Equations. *International Journal for Numerical Methods in Fluids* 2008; **57**(11): 1649-1668.

89. Zhou JG, Causon DM, Mingham CG, Ingram DM**.** The Surface Gradient Method for the Treatment of Source Terms in the Shallow-Water Equations. *Journal of Computational Physics* 2001; **168**(1): 1-25.

90. Zhou JG, Causon DM, Ingram DM, Mingham CG**.** Numerical Solutions of the Shallow Water Equations with Discontinuous Bed Topography. *International Journal for Numerical Methods in Fluids* 2002; **38**(8): 769-788.

91. Zienkiewicz OC, Ortiz P**.** A Split-Characteristic Based Finite-Element Model for the Shallow-Water Equations. *International Journal for Numerical Methods in Fluids* 1995; **20**(8-9): 1061-1080.

92. Zienkiewicz OC, Codina R**.** A General Algorithm for Compressible and Incompressible Flow Part I. The Split, Characteristic-Based Scheme. *International Journal for Numerical Methods in Fluids* 1995; **20**(8-9): 869-885.

93. Zienkiewicz OC, Morgan K, Sai B, Codina R, Vasquez M**.** A General Algorithm for Compressible and Incompressible Flow. Tests on the Explicit Form. *International Journal for Numerical Methods in Fluids* 1995; **20**(8-9): 887-913.

94. Zienkiewicz OC, Morgan K, Sai B, Codina R, Vasquez M**.** A General Algorithm for Compressible and Incompressible Flow Part II. Tests on the Explicit Form. *International Journal for Numerical Methods in Fluids* 1995; **20**(8-9): 887-913.